

**Investigating small-scale dynamics:
Analysis and Interpretation of Solar Orbiter
observations**

Von der Fakultät für Elektrotechnik, Informationstechnik, Physik
der Technischen Universität Carolo-Wilhelmina zu Braunschweig

zur Erlangung des Grades einer Doktorin

der Naturwissenschaften (Dr. rer. nat.)

genehmigte Dissertation

von Ziwen Huang

aus Jiangsu

1. Referent: Prof. Dr. Sami K. Solanki
2. Referent: Prof. Dr. Ferdinand Plaschke

eingereicht am: 11.03.2025

Disputation am: 08.07.2025

Druckjahr: 2025

**Dissertation an der Technischen Universität Braunschweig,
Fakultät für Elektrotechnik, Informationstechnik, Physik**

Abstract

The solar atmosphere is a highly dynamic and magnetically complex environment, where two of the key open questions are how the corona is heated to over a million kelvin and how the solar wind is generated. Small-scale activities, such as bright points, small jets, and spicules, are believed to play a fundamental role in supplying energy and material to the corona. Although these energy releases are subtle compared to large-scale events, they may be pervasive enough to contribute significantly. Due to their transient and small-scale nature, observations in high resolution, both spatially and temporally, are essential for understanding the mechanisms underlying these small-scale energy releases and assessing their role in sustaining the coronal temperature and driving the solar wind.

Along with the advancements in observational techniques, our understanding of small-scale structures in the corona has significantly improved over the past few decades. The launch of Solar Orbiter in February 2020 has further expanded these opportunities. It follows a unique highly elliptical orbit, allowing it to observe the Sun from as close as 0.28 au at perihelia and to capture the high-latitude views of the polar regions (starting from 2025). Solar Orbiter carries ten instruments, both in-situ and remote-sensing, including the Extreme Ultraviolet Imager (EUI) for high-resolution imaging, the Spectral Imaging of the Coronal Environment (SPICE) for spectroscopic analysis, and the Polarimetric and Helioseismic Imager (SO/PHI) for magnetic field measurement, offering valuable data for studying the small-scale dynamics in the solar atmosphere.

This thesis presents the results of two main investigations. The first study is focused on the EUI brightenings in the quiet sun, the smallest transient EUV brightenings that have been so far reported, based on the high-resolution observations from EUI. Three EUI brightenings are captured by both the High Resolution EUV telescope (HRI_{EUV} , part of EUI) and SPICE in this study. The detection of the EUI brightenings is almost at the limit of SPICE's capability, which means that the identification of these structures is only possible with the assistance of HRI_{EUV} images. On the other hand, SPICE can provide the multi thermal information of the brightenings. By combining both data sets, two of these EUI brightenings with longer duration are found to be detectable at Ne VIII temperature (0.6 MK). The signatures of all three brightenings are detected in an O VI line (0.3 MK). It is also possible to investigate the thermal evolution of one of these brightenings, where double peaks are observed in the light curves of C III (0.06 MK) and O VI, while the only peak in the light curve of Ne VIII is found between the two peak times of the intensities of the two transition region lines. This suggests that the temperature of this brightening could increase from the formation temperature of the C III line to that of the O VI line and then to the Ne VIII temperature (from upper transition region to low corona), and then it cools down. These findings also lead to the conclusion that some EUI brightenings could barely reach coronal temperatures. As part of this study I also derive a model of the noise of the SPICE detectors. As these detectors are

conceptually very similar to those that will be used on future missions such as the Extreme Ultraviolet Spectroscopic Telescope (EUVST) under construction for the forthcoming Solar-C mission, these results will be applicable with only minor adaptation.

The second part of this work is about the small-scale transients in the coronal hole plumes. Plumes are the largely ray-like structures that could channel magnetohydrodynamic waves and solar wind and are observed to host high-speed propagating disturbances (PDs) and small-scale transients at their bases. Three plumes are detected within an equatorial coronal hole by HRI_{EUV}. At these plume bases, from tens to hundreds of base brightenings are observed in the 30-min observation. Their properties (intensity, size, lifetime, shape and apparent speed) are studied statistically. The results show that most of the base brightenings are small-scale, short-lived and appear slightly elongated. These brightenings exhibit complex motion, with most moving at speeds below 10 km s^{-1} in the plane of sky. Potential field extrapolation, based on magnetic field data obtained by SO/PHI, is applied to de-project the apparent speed to the real velocity along the magnetic field, which is still found to be significantly lower than, and hard to reconcile with, the higher speeds observed in PDs at greater heights within the plumes. Since a direct connection between base brightenings and PDs remains uncertain, two possible explanations are proposed for the base brightenings: they could be associated with wave-driven Type I spicules or result from interchange reconnection events.

In summary, this study utilizes a diverse set of high-resolution observations from Solar Orbiter to investigate small-scale structures in both the quiet Sun and coronal hole regions. These data provide valuable insights into the characteristics of these structures and the physical mechanisms behind them. Due to the limitations of the data sets, certain aspects remain inconclusive in this work and require further investigation with observations from multiple instruments. In the last chapter I finally provide some considerations of how observations from forthcoming missions such as EUVST and Multi-slit Solar Explorer (MUSE) will be able to improve our knowledge of the events studied in this thesis.

Key words. Sun: activity – Sun: atmosphere – Sun: magnetic fields – Solar Wind – Sun: UV radiation

Zusammenfassung

Die Sonnenatmosphäre ist eine hochdynamische und magnetisch komplexe Umgebung, in der es zwei zentrale ungelöste Fragen gibt: Wie wird die Korona auf über eine Million Kelvin erhitzt und wo hat der Sonnenwind seinen Ursprung? Kleine Aktivitäten wie Aufhellungen, kleine Jets und Spikulen spielen eine wichtige Rolle beim Energie- und Materialtransport in die Korona. Diese Energieentladungen sind zwar, im Vergleich zu größeren Ereignissen, subtiler, könnten jedoch verbreitet genug sein, um einen signifikanten Beitrag zu leisten. Aufgrund der Kurzlebigkeit und geringen Fläche dieser kleinen Energieentladungen sind hochauflösende Beobachtungen, sowohl räumlich als auch zeitlich, unerlässlich, um die Mechanismen dahinter und somit und ihre Rolle bei der Aufrechterhaltung der koronalen Temperatur und der Erzeugung des Sonnenwinds zu verstehen.

Durch Fortschritte an den Instrumenten zur Sonnenbeobachtung hat sich unser Verständnis der kleinen Strukturen in der Korona in den letzten Jahrzehnten erheblich verbessert. Mit dem Start von Solar Orbiter im Februar 2020 haben sich diese Möglichkeiten nochmals erweitert. Solar Orbiter folgt einer einzigartigen, stark elliptischen Umlaufbahn, die es ihm ermöglicht, die Sonne aus einer Entfernung von 0,28 au im Perihel zu beobachten und die Polarregionen in hohen Breitengraden zu erfassen (seit 2025). Die wissenschaftliche Nutzlast von Solar Orbiter besteht aus zehn Instrumenten für Fern- und in-situ Beobachtungen. Zu den Fernerkundungsinstrumenten gehören das Extreme Ultraviolet Imager (EUI) für hochauflösende Bilder, das Spectral Imaging of the Coronal Environment (SPICE) für spektroskopische Analysen und das Polarimetric and Helioseismic Imager (SO/PHI) zur Magnetfeldmessung, die wertvolle Daten zur Untersuchung kleinen dynamischen Prozessen in der Sonnenatmosphäre liefern.

Diese Dissertation präsentiert die Ergebnisse aus zwei Studien. Die erste Studie konzentriert sich auf die EUI-Aufhellungen in der ruhigen Sonne. Hierbei handelt es sich um die kleinsten EUV-Aufhellungen, die bisher berichtet wurden. Sie wurden mit Hilfe der hochauflösenden Beobachtungen von EUI untersucht. Drei EUI-Aufhellungen werden in dieser Studie sowohl vom High Resolution EUV Telescope (HRI_{EUV} , Teil von EUI) als auch von SPICE erfasst. Die Detektion dieser EUI-Aufhellungen liegt nahe der Auflösungsgrenze von SPICE, was bedeutet, dass die Identifizierung dieser Strukturen nur mit Unterstützung von HRI_{EUV} -Bildern möglich ist. SPICE kann jedoch multitermale Informationen der EUI-Aufhellungen liefern. Durch die Kombination beider Datensätze zeigt sich, dass zwei dieser EUI-Aufhellungen mit längerer Dauer bei Ne VIII-Temperaturen (0,6 MK) nachweisbar sind. Alle drei EUI-Aufhellungen sind in einer O VI-Linie (0,3 MK) nachweisbar. Es ist auch möglich, die thermische Entwicklung eines dieser Ereignisse zu untersuchen, bei dem doppelte Spitzen in den Lichtkurven von C III (0,06 MK) und O VI, beobachtet wurden, während eine einzige Spitze in der Lichtkurve von Ne VIII zwischen den beiden Spitzen der Übergangsregion-Linien liegt. Dies deutet darauf hin, dass die Temperatur dieses Ereignisses von der C III-Linientemperatur über die O VI-Linie bis hin zur

Ne VIII-Temperatur (von der oberen Übergangsregion bis zur unteren Korona) steigen könnte, um dann abzukühlen. Diese Ergebnisse legen ebenfalls nahe, dass einige EUV-Aufhellungen kaum die koronale Temperatur erreichen können. Im Rahmen dieser Studie leite ich auch ein Modell für das Rauschen der SPICE-Detektoren ab. Da diese Detektoren konzeptionell denen, welche bei zukünftigen Missionen wie dem sich im Bau befindlichen Extreme Ultraviolet Spectroscopic Telescope (EUVST) für die bevorstehende Mission Solar C verwendet werden, sehr ähneln, werden diese Ergebnisse mit nur geringen Anpassungen anwendbar sein.

Der zweite Teil dieser Arbeit befasst sich mit kleinen und vorübergehenden Ereignissen in Plumes, welche in koronalen Löchern vorkommen. Plumes sind große strahlenartige Strukturen und können magnetohydrodynamische Wellen und den Sonnenwind kanalisieren. An ihren Fußpunkten lassen sich sehr schnell ausbreitende Störungen (propagating disturbances, PDs) sowie kleine vorübergehende Ereignisse beobachten. Drei Plumes wurden innerhalb eines äquatorialen koronalen Lochs von HRI_{EUV} erfasst. An den tiefliegenden Teilen dieser Plumes wurden in einer 30-minütigen Beobachtung von mehreren Dutzend bis hin zu mehreren hundert tief-liegende Aufhellungen (base brightenings) festgestellt. Es wurde eine statistische Analyse ihrer Eigenschaften (Intensität, Größe, Lebensdauer, Form und Geschwindigkeit) durchgeführt. Die Ergebnisse zeigen, dass die meisten base brightenings klein, kurzlebig und leicht länglich erscheinen. Die base brightenings zeigen komplexe Bewegungen, wobei sich die meisten mit Geschwindigkeiten von unter 10 km s^{-1} in der Bildebene der Sonne bewegen. Mit einer potentielle Magnetfeldextrapolation auf Grundlage von SO/PHI-Daten lässt sich die scheinbare Geschwindigkeit auf die reale Geschwindigkeit entlang des Magnetfelds entprojizieren. Die Geschwindigkeit ist jedoch immer noch signifikant niedriger ist als die höheren Geschwindigkeiten der PDs in höheren Regionen der Plumes. Da eine direkte Verbindung zwischen base brightenings und PDs unsicher bleibt, werden zwei mögliche Erklärungen für die base brightenings vorgeschlagen: Sie könnten mit wellentreibenden Typ-I-Spikulen oder mit Austauschrekonexionseignissen zusammenhängen.

Zusammenfassend nutzt diese Dissertation eine Vielzahl an hochauflösenden Beobachtungen von Solar Orbiter zur Untersuchung von kleinen Strukturen sowohl in der ruhigen Sonne als auch in einem koronalen Loch. Diese Daten liefern wertvolle Einblicke in die Eigenschaften dieser Strukturen und die ihnen zugrundeliegenden physikalischen Mechanismen. Aufgrund von Einschränkungen in den Datensätzen bleiben einige Aspekte in dieser Arbeit ungeklärt und erfordern weitere Untersuchungen, die Beobachtungen mit mehreren Instrumenten umfassen. Im letzten Kapitel gehe ich schließlich darauf ein, wie die Beobachtungen künftiger Missionen wie EUVST und der Multi-slit Solar Explorer (MUSE) unser Wissen über die in dieser Arbeit untersuchten Ereignisse verbessern können.

Contents

1	Introduction	1
1.1	Solar atmosphere	2
1.1.1	Overview of the solar atmosphere	2
1.1.2	From photosphere to corona	5
1.1.3	Magnetic field	12
1.2	The solar wind	16
1.3	Coronal heating problem	19
1.3.1	Discovery of the corona's temperature	19
1.3.2	Energy Requirements	21
1.3.3	Heating mechanisms	23
1.4	Small-scale dynamic events	27
1.4.1	Brightenings	28
1.4.2	Jet-like events	31
1.5	Motivation of this thesis	33
2	Instruments and Methods	37
2.1	Solar Orbiter	37
2.1.1	EUI: The Extreme Ultraviolet Imager	38
2.1.2	SPICE: The Spectral Imaging of the Coronal Environment	41
2.1.3	SO/PHI: The Polarimetric and Helioseismic Imager	43
2.2	Data diagnostics Methods	44
2.2.1	Differential Emission Measure	44
2.2.2	Magnetic field extrapolation	48
2.2.3	Error estimation	50
3	Brightenings in the quiet sun	53
3.1	Introduction	53
3.2	Overview of observations	56
3.3	Data preparation and analysis	60
3.3.1	Data preparation and Gaussian fit	60

CONTENTS

3.3.2	Error estimation of SPICE data	61
3.3.3	Data alignment: searching SPICE data for EUI brightening signatures	65
3.4	Results	70
3.4.1	23 February 2021: Event E-1	70
3.4.2	12 September 2021: Event E-2	73
3.4.3	13 September 2021: Event E-3	77
3.4.4	DEM analysis	82
3.5	Discussion and Conclusion	84
4	Brightenings in the coronal holes	87
4.1	Introduction	87
4.2	Observation overview	90
4.3	Data analysis	92
4.3.1	Visual identification method	92
4.3.2	Automatic method	94
4.3.3	Comparisons of thresholds	96
4.3.4	Properties of brightenings	99
4.4	Results	100
4.4.1	Visual detection results	100
4.4.2	Automatic detection results	102
4.4.3	Brightenings and PDs	104
4.5	Velocity correction	106
4.6	Discussion	111
4.6.1	Link between base brightenings and PDs	111
4.6.2	Decoding base brightenings	115
4.7	Conclusion	117
5	Conclusions and outlook	119
	Bibliography	127
	Acknowledgement	157
	Publications	159
	Curriculum Vitae	161

List of Figures

1.1	Plasma β model	3
1.2	Structure of the solar atmosphere	4
1.3	Granulation and the chromospheric network.	7
1.4	Quiet sun magnetic field structure	13
1.5	Solar wind speed measurements from the Ulysses spacecraft	17
1.6	1-dimensional model of temperature and density in solar atmosphere	20
1.7	Parker's braiding model	26
1.8	Examples of small-scales activities observed in X-ray and EUV channels	29
2.1	Solar Orbiter payloads	39
2.2	SPICE FOV diagram	43
3.1	Images of HRI _{EUUV} FOV	59
3.2	Noise estimation for uncalibrated SW data	64
3.3	Noise estimation for uncalibrated LW data	64
3.4	First step of data alignment: coarse alignment	66
3.5	Second step of data alignment: cross correlation of time-slice images	68
3.6	Maps of correlation coefficients	69
3.7	Time-slice plots of EUV brightening E-1	71
3.8	Image and light curve of EUV brightening E-1	72
3.9	O VI spectra profiles of EUV brightening E-1	73
3.10	Time-slice plots of EUV brightening E-2	75
3.11	Image and light curve of EUV brightening E-2	76
3.12	Ne VIII spectra profiles of EUV brightening E-2	77
3.13	Time-slice plots of EUV brightening E-3	78
3.14	Image and light curve of EUV brightening E-3	79
3.15	Evolution of EUV brightening E-3	81
3.16	O VI spectra profiles of EUV brightening E-3	82

LIST OF FIGURES

3.17	DEMs of EUI brightening E-2	83
3.18	DEMs of EUI brightening E-3	84
4.1	Overview of coronal hole observations	91
4.2	Dynamics at the base of plumes	93
4.3	Base brightenings detected automatically.	95
4.4	Test of the the threshold describing the neighborhood	97
4.5	Test of the boundary threshold	98
4.6	Visual detection results	101
4.7	Automatic detection results	103
4.8	Measurements of the speeds of PDs	105
4.9	Magnetic field imprints of the plumes	107
4.10	Potential extrapolation tests based on HMI data	110
4.11	Brightness structure and width of the propagating disturbance	112
5.1	Picoflare jets in the interplume region.	123

List of Tables

1.1	Chromospheric and coronal energy losses	22
2.1	Characteristics of the telescopes of EU1	40
2.2	Characteristics of main spectral lines observed by SPICE	42
3.1	Overview of the observations.	57
3.2	Event characteristics	60
3.3	Error estimate parameters	63
4.1	Automatically detected brightenings categorized according to directions	104
5.1	Overview of some key spectroscopic instruments	125

LIST OF TABLES

Chapter 1

Introduction

The Sun, our closest star, is a dynamic, evolving celestial object that has undergone significant changes since its early formation. According to stellar evolution models, the Sun emerged from a cloud of gas and dust. It formed as a T Tauri star (Hayashi 1961) and settled into its current G2 classification upon entering the main sequence phase (Chapter 2.2 in Stix 2002). In approximately 5 billion years, the Sun will leave the main sequence and enter a red giant phase, dramatically expanding in size (Sackmann et al. 1993). At the current stage of its evolution, it is formed by a central core (where nuclear reactions powering the star take place), a zone from about 25% to 70% of its radius where energy is transported by radiation, and a zone reaching to the visible surface (the so-called photosphere) where energy is transported by convection. The solar atmosphere starts at the photosphere and extends outward, which is the main topic of this thesis.

1.1 Solar atmosphere

1.1.1 Overview of the solar atmosphere

Charged particles in the solar atmosphere are under the effect of thermal pressure, Lorentz force and gravity. Among them there are two internal pressures, i.e., the thermal pressure, arising from the random motions of the particles, and the magnetic pressure, originating from the Lorentz force the magnetic field applies to the charged particles, influencing how plasma behaves in the presence of magnetic fields. Due to the low resistivity in the solar atmosphere, the plasma and the magnetic field are coupled to move together. Note that, the “movement” of magnetic field is a result of charged particles in motion, which create currents that, in turn, generate the secondary fields that keep the magnetic flux constant. When the thermal pressure dominates, the plasma modifies the magnetic field with its motion. Otherwise, it follows the structure of the magnetic field. The parameter describing their relation is called plasma β , defined as the ratio of the thermal pressure ($P_{th} = nkT$, under the assumption of the solar atmosphere being an ideal gas) to the magnetic pressure ($P_{mag} = B^2/2\mu_0$):

$$\beta = \frac{P_{th}}{P_{mag}} = \frac{nkT}{B^2/2\mu_0} \quad (1.1)$$

where n is the number density of particles, T is the temperature, B is the magnetic strength, k is Boltzmann’s constant and μ_0 is the vacuum permeability.

Figure 1.1 shows a plasma β model from Gary (2001), where the author considered the magnetic field strength between 2500 Gauss and 150 Gauss. It is clear that the solar atmosphere has high- β regions: the photosphere and solar wind acceleration region; low- β regions: the transition region and the corona; and an intermediate- β region: the chromosphere. This indicates that, the plasma and magnetic field interact in different ways at different heights, structuring the solar atmosphere.

An overview of the solar atmosphere can be found in Figure 1.2. Generally, the solar atmosphere is referred to as a "multi-layer" structure (from inside to outside: the photosphere, the chromosphere, the transition region and the corona), with each layer exhibiting distinct properties and observational charac-

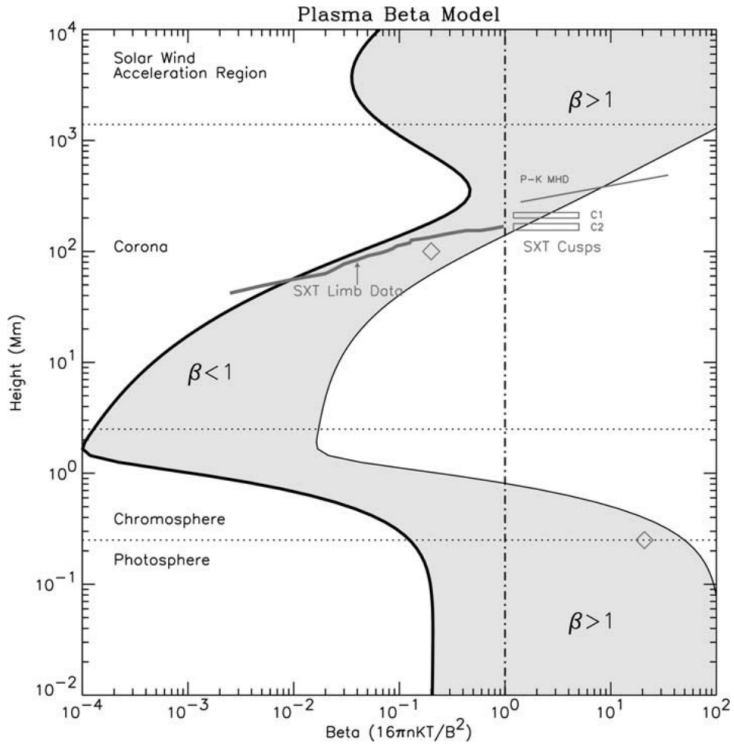


Figure 1.1: Plasma β as a function of height over an active region (introduced later in this Section). The two side boundaries of the gray shaded region come from the magnetic strengths of 2500 Gauss and 150 Gauss. This model is compared with various data, shown in grey symbols and text. Image credit: Gary (2001), reproduced with permission from Springer Nature.

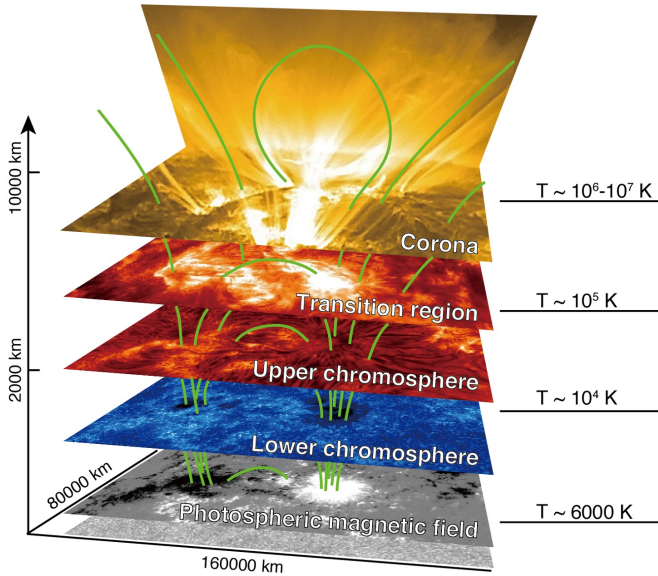


Figure 1.2: Structure of the solar atmosphere. From bottom to top are photosphere, chromosphere, transition region and corona, each characterized by different heights and temperatures. The observational phenomena in different layers are connected by the magnetic field (see green lines). Image credit: SOLAR-C webpage; NAOJ/JAXA, NASA¹.

teristics, bridged by the magnetic field. However, this is just a schematic representation showing observations at different wavelengths/temperatures. The idea of "multi-layer" is a 1-dimensional perspective (i.e., along a field line), while the actual solar atmosphere is more dynamic and highly structured by the magnetic field.

The solar magnetic field is complex and highly variable, with magnetic concentrations occurring at different scales. It varies in strength, scale, and configuration across different regions (see review by Wiegelmann et al. 2014) and across the solar cycle (see review by Hathaway 2015). Generally speaking, there

¹<https://solar-c.nao.ac.jp/en/science.html>

are active regions, coronal holes and the quiet sun in the solar atmosphere. Active regions are large concentrated areas of strong magnetic fields with opposite polarities connected by large-scale loops. Coronal holes are regions with a prevalence of unipolar magnetic fields. Failing to find an opposite polarity nearby to connect, the magnetic field there generally opens outwards, or more strictly, only closes back to the solar surface over very large distances as there are no magnetic monopoles. In the quiet sun, the magnetic field is much weaker, but distributes in a structured way to form a network-like pattern with small-scale concentrations.

The solar magnetic field is not only non-uniform but also dynamic. It is continually generated and restructured and interacts with surrounding plasma, with material flows and energy transportation involved. All these will be introduced again in more details in Section 1.1.3. The solar atmosphere, especially the low- β regime, e.g., the corona, is thus highly inhomogeneous, being structured by the solar magnetic field. As a consequence, each "layer" cannot be well defined based on height or heliocentric distance, but instead, depends more on their temperatures and the emissions they produce. In the coming section, we will talk about each region in detail, going from the photosphere to the chromosphere, the corona and the so-called transition region, the very narrow interface between the chromosphere and the corona.

1.1.2 From photosphere to corona

1.1.2.1 High- β : Photosphere

The photosphere is defined as the region where the optical depth $\tau_{500nm} = 2/3$ in visible light (500 nm) is reached (e.g., Zirin 1992). As the name implies, it is the surface that can be observed by eye, due to its temperature and density. The effective temperature of the photosphere is about 5800 K, which, according to the black body radiation, allows it to efficiently emit in the visible spectrum (Planck 1991). The photosphere has a typical density of $3.4 \times 10^{-7} \text{ g cm}^{-3}$, resulting in a mean free path ($l = 1/k\rho$, where k is the opacity and ρ is the density) of photons, longer than the size of the structure they traveling through, that they can escape. Below the photosphere, the photons can easily be scattered

or absorbed in a short distance. Above the photosphere, visible light emission is extremely faint compared to the photosphere, as more than 99.9% of the visible light comes from the photosphere. Therefore, the chromosphere can only be observed by eye when the emission from the photosphere is blocked, e.g., during a total eclipse or when looking through very narrow filters centered on the core of strong spectral lines (very high opacity) such as the $H\alpha$ line of hydrogen at 656.5 nm. The corona, with its even lower density, is only observable under similar conditions during total eclipses or when using a coronagraph.

The photosphere is commonly observed in visible light and presents many features, such as the sunspots, the faculae and the granulation. Sunspots are cooler (with a temperature of 3000–4500 K), hence darker regions. A review of their structures and physics can be found in Solanki (2003). Their lifetimes are believed to be proportional to their maximum size (Gnevyshev 1938; Waldmeier 1955). A typical lifetime of a sunspot (e.g., about 10 Mm in diameter) is of several days, but large ones (reaching diameters of 60 Mm or more) can exist for weeks and their numbers and locations change over a solar cycle (Hale 1908). They exhibit a central darker region called umbra surrounded by the lighter penumbra. All these characteristics are related to strong magnetic concentrations. In the umbra, the magnetic field is so strong that it suppresses the underneath convective flows, reducing the amount of energy transported from the interior. Unlike the vertical field of the umbra, penumbral magnetic field tends to turn over (Title et al. 1992; Lites et al. 1993) and allow convective flows to partially convey energy out to the surface. Sunspots usually appear in groups and reside in the regions with more dynamic magnetic activities called active regions (Zwaan et al. 1985; Zwaan 1987; Harvey and Zwaan 1993), appearing as bright regions on the sun disk in X-ray and extreme ultraviolet (EUV; 10 nm to 120 nm) passbands. Unlike sunspots, faculae, much easier observed at the limb of the solar disk (e.g., Auffret and Muller 1991; Sánchez Cuberes et al. 2002), are hotter than their surroundings and thus are brighter. They are also a manifestation of relatively strong magnetic flux tubes (but smaller and weaker than those forming sunspots) that by locally reducing the gas density, make it possible to see through into the deeper, hence hotter, layers (Keller et al. 2004).

Granules are the cellular features (see panel (a) in Figure 1.3, also see obser-

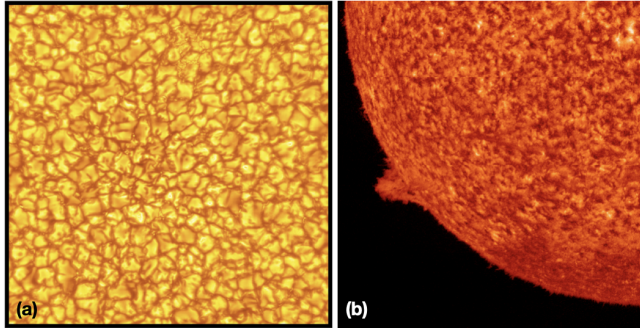


Figure 1.3: (a) Image of the quiet sun at photosphere, taken by the Inouye Solar Telescope at the wavelength of 450.4 nm (covering an area of $30720 \text{ km} \times 30720 \text{ km}$). It shows the bright granules and the dark intergranular lanes. Image credit: NSF/AURA/NSO², licensed under a CC BY 4.0; (b) Image of the south-east quadrant of the Sun at the upper chromosphere, taken by Solar UV Measurement of Emitted Radiation (SUMER) at the wavelength of 58.4 nm (He I). The chromospheric network can be seen in this image. Image credit: SUMER Main Page³, prepared by I. E. Dammasch and K. Wilhelm.

ations in, e.g., Title et al. 1989; Wilken et al. 1997) representing the convective motion at the top of the convection zone (see review by Nordlund et al. 2009). Driven by buoyancy forces, hot material emerges from interior to the surface to form the bright cells. Once the hot plasma reaches the surface, it spreads outwards (horizontal flow) under the pressure gradient until encountering the horizontal flow from another cell. There, the plasma gets cooler and denser due to strong radiative loss and then sinks back, forming dark lanes (Stein and Nordlund 1998). Granules are small (with a typical linear size of about 1000 km (Roudier and Muller 1986)) and can live for only 8–20 min (Bahng and Schwarzschild 1961). They spread over the whole sun surface except for the sunspot regions and are highly dynamic as the old granule cells are continuously pushed aside by the emerging materials.

²<https://nso.edu/gallery/gallery-images-from-the-inouye>

³<http://soi.stanford.edu/results/SolPhys200/Wilhelm/index.html>

Besides, the velocity maps of the photosphere reveal structures known as supergranules, which have a spatial size of about 30–40 Mm and a longer lifetime of a day or two (see review by Rieutord and Rincon 2010). They are related to larger-scale and deeper convection, compared with granules. The horizontal flow inside of the supergranular cells thus can push magnetic fields towards the cell boundaries, forming the magnetic network that can be observed in the chromosphere (see panel (b) in Figure 1.3). More details are discussed in Section 1.1.2.2.

Another observational phenomenon in the photosphere is the 5 min oscillations (first observed by Leighton et al. 1962 and by Evans and Michard 1962), which appear as a periodic motion and are a manifestation of pressure (p-mode) waves (Ulrich 1970; Leibacher and Stein 1971). They are formed by the convection at or close to the solar surface, i.e., when materials rise up and sink down, pressure disturbance is created and propagates in the form of acoustic waves. This oscillation, in general, are evanescent in the photosphere and chromosphere with only waves with periods of less than 3 min (acoustic cutoff frequency, Balmforth and Gough 1990) can propagate into the higher atmosphere.

1.1.2.2 Intermediate- β : Chromosphere

The chromosphere is located just above the photosphere and is approximately 2000 km thick. The lower boundary of the chromosphere is usually defined as the height where the temperature reaches its minimum (~ 4000 K). Above that, the temperature rises to 10000–20000 K, while the density drops roughly by a factor of 10^7 in the chromosphere. Although the chromosphere is usually not visible in white light due to its emission being too faint compared to photosphere, it can be seen with the naked eye during total eclipses and appears to be red because of strong emissions in the Balmer α line of hydrogen ($H\alpha$ line at 656.5 nm).

Accompanying the strong magnetic field concentrations, sunspots are observable in the wavelengths that sample the lower chromosphere, e.g., $H\alpha$ and Ca II K and H lines. Besides, in these channels, one can see bright plages, the chromospheric bright patches, around the sunspots (strong magnetic concentrations) and can remain from days to weeks (Babcock and Babcock 1955). Away from the active chromosphere, a bright web-like pattern (see panel (b) in Fig-

ure 1.3) outlining the supergranular cells can be observed, called chromospheric network (e.g., Leighton et al. 1962; Simon and Leighton 1964). It is bright in $H\alpha$ and EUV lines because the strong magnetic concentrations can channel more energy into the chromosphere. Governed by the photospheric convection motion, the chromospheric network changes over a timescale from a few tens of hours to days (e.g., Simon and Leighton 1964; Janssens 1970; Livingston and Orrall 1974). The chromosphere also show oscillatory motions, which exhibit a prominent period of 3 min (e.g., Lites and Thomas 1985; Abdelatif et al. 1986; Deubner and Fleck 1990). They are strongly observed in sunspot umbrae, but also in other regions of the chromosphere.

As can be already noticed at the edge of the solar disk at eclipses, the chromosphere is dynamic with prominences and spicules. Prominences are dense and cooler materials suspended above the surface by magnetic fields (see review by Parenti 2014). They usually exhibit a loop-or-ribbon-like pattern above the limb while they are called filaments when seen against the disk. Filaments look like dark scars against the bright background. They are usually held by twisted or sheared magnetic structures providing enough upward pressure to balance gravity (Antiochos et al. 1994; DeVore and Antiochos 2000; Amari et al. 2000). Spicules are jet-like structures that can potentially shoot up mass or energy into the higher atmosphere. Their on-disk counterparts are called fibrils or mottles (Roupe van der Voort et al. 2007; Heggland et al. 2007). Typically, spicules can be categorized into two types: type I spicules move more slowly and show a back-and-forth motion (i.e., the material rising in them is seen to fall down again) while type II spicules have a higher speed and disappear rapidly (De Pontieu et al. 2007b). See Section 1.4.2 for more details.

1.1.2.3 Low- β : Corona

The corona is the outermost part of the Sun's atmosphere, characterized by its extremely high temperature, ranging from 1 to 3–4 MK (and up to over 10 MK during flares), and low density (of highly ionized plasma) compared to the lower layers. It is visible during total eclipses (or with an artificial eclipse in the coronagraph), when different features can be seen out of the occulted solar disk, e.g., closed coronal loops, cusp-like helmet streamers and ray-like polar

plumes (Newkirk 1967). Note that, although the average corona is described as a low- β environment, its dynamic nature can create localized high- β conditions. Also, the plasma β in different regions, e.g., in active regions or quiet sun, could also be very different (e.g., Schrijver and van Ballegooijen 2005).

At the corona's temperature, the dominating hydrogen and helium are almost fully ionized, and the heavier elements, such as carbon, nitrogen, oxygen and up to iron, are in their highly ionized states. Thus, the emission lines in the corona mostly come from highly ionized, heavier ions. The discovery of these lines helped to determine the concept of a hot corona, containing plasma at a wide range of high temperatures (e.g., Grotrian 1939; Edlén 1945). This multi-temperature corona is very well observed in images obtained in X-ray and EUV band passes where it is clear that the corona varies spatially. Typically, it has bright active regions, dark coronal holes and the rather calm quiet sun. All of them, as mentioned, are rooted in the deeper atmosphere and closely related to the magnetic field.

Active regions, associated with strong concentrations of magnetic fields, have higher temperature than the surroundings and are thus brighter in X-ray and EUV and far ultraviolet (FUV; 120 nm to 200 nm) channels. These regions are usually characterized by large-scale closed loops filled with high temperature plasma (Bray et al. 1991) and violent energy release, such as solar flares (see reviews by Benz 2008, 2017) and coronal mass ejections (CMEs, see reviews by Chen 2011; Webb and Howard 2012). Differently, coronal holes are regions where the magnetic field generally opens outwards. They typically appear near the polar regions around the minimum of the solar cycle, but can also be found in low-altitude regions throughout the cycle, even across the equator (Sanchez-Ibarra and Barraza-Paredes 1992). Due to the open magnetic fields, plasma can easily escape, leaving the "dark holes" with lower temperature and density. In fact, coronal holes are considered as a source region of solar wind, crucial to the space weather (e.g., Krieger et al. 1973; Zirker 1977, also see review Cranmer et al. 2007). The quiet sun is generally governed by weak and small magnetic elements. Despite its name, the quiet sun is very dynamic. As the magnetic field is constantly influenced by the evolution and interaction of supergranules, it can produce numerous small-scale events.

Speaking of multi-scale energetic processes in the corona, the most astonishing activities are large flares and CMEs. They are considered as the manifestations of the same process releasing magnetic energy (Webb and Howard 2012). With the improvement of instrumental technique, more mini-eruptions and localized intensity enhancement can be detected in the vicinity of active regions, quiet sun and coronal holes, such as coronal jets (e.g., Shibata et al. 1992), coronal bright points (CBPs, see review by Madjarska 2019) and microflares/nanoflares (see Section 1.4). These events, although each one only releases a small amount of energy compared with large-scale activities, could be an indispensable energy source to the million-Kelvin corona if happening frequently enough (e.g., Parker's braiding model, Parker 1972, 1983, 1988).

1.1.2.4 Transition region

Once the million degrees temperature of the corona was discovered in the mid 20th century, it became evident that there should also be regions at temperatures between the chromospheric temperature of about 20000 K and the coronal temperature. Later, the first 1-dimensional MHD models of solar loops did show that such a rise would occur on very short spatial scales (e.g., Gabriel and Mason 1982). Thus, the term "transition region" was introduced to describe the narrow temperature region between the chromosphere and the corona at temperatures around 10^5 K. In reality, when considering a 3-dimensional view of the solar atmosphere, the transition region should be defined based on temperatures, rather than height and not necessarily always connecting chromospheric to coronal plasma. For instance, cold loops with their apex still at transition region temperatures also exist (Dowdy et al. 1986).

The transition region is characterized by strong emission lines in the FUV and EUV ranges. The lower transition region (2×10^4 K to 1×10^5 K) can be observed in the Ly α line of Hydrogen (121.6 nm) and lines from lowly ionized ions such as C II (133.4 nm and 133.6 nm) and Si III (120.7 nm). At the higher temperatures of the mid transition region (1×10^5 K to 3×10^5 K), the emission is dominated by lines such as from C IV (154.8 nm and 155.1 nm), N V (123.9 nm and 124.3 nm) and O VI (103.2 nm and 103.8 nm). Finally, in the upper transition region (3×10^5 K to about $7-8 \times 10^5$ K), lines such as Ne VIII (77 nm and 78 nm)

can be found. A summary of prominent spectral lines observable in the transition region in the EUV (10–120 nm) and FUV (120–200 nm) range together with their formation temperatures can be found in Table 1.1 in Mariska (1992). Covering a wide range of temperature, the transition region is significantly important for investigating the coronal heating problem (see Section 1.3).

A variety of features are revealed in the dynamic transition region. In the lower transition region, the chromospheric network is still visible, but gets more and more diffuse with increasing height/temperature, possibly demonstrating the rapid expansion of the magnetic flux tubes (Patsourakos et al. 1999). The transition region counterparts of chromospheric spicules are also confirmed as plasma flowing at comparable velocities present in both images and Doppler maps (Tian et al. 2014; Narang et al. 2016; De Pontieu et al. 2017). Besides, small-scale transients are detected at transition region temperatures. For instance, explosive events are high velocity (up to about 150 km s^{-1}) jets, often bi-directional, seen in transition region lines (Innes et al. 1997). Dere et al. (1991) suggested that explosive events are closely associated with magnetic flux cancellation and reconnection (also see Innes et al. 1997). Transition region blinkers are longer-lived brightenings that occur both in the supergranule network and above the plage and sunspot regions (Parnell et al. 2002). Instead of a local heating, blinkers are possibly a result of increasing filling factor of emitting plasma (Priest et al. 2002a; Bewsher et al. 2002).

1.1.3 Magnetic field

The Sun has a global magnetic field, with numerous dynamic and complex inhomogeneities. The solar magnetic field is generated by a physical process called the solar dynamo, which is driven by the plasma motion and electric currents in the solar interior, particularly in or just under the convection zone (see review by Charbonneau 2014). The solar dynamo model explains well some cyclical observational phenomena like the 11-year sunspots cycle and the equator-ward sunspots drifting (the butterfly diagram, see early discoveries in, e.g., Carrington 1858; Maunder 1904, also see review by Hathaway 2015). Under the effect of solar rotation and convection flows, the twisted magnetic field eventually emerges

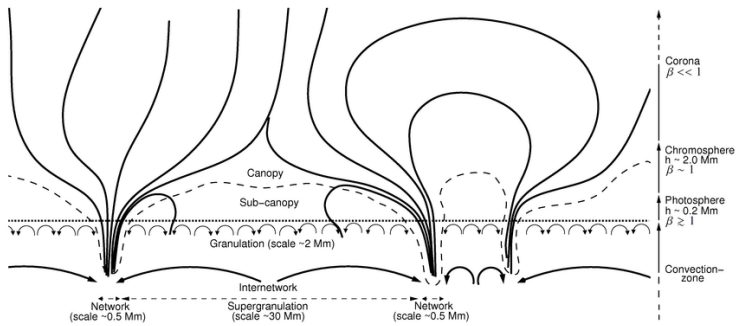


Figure 1.4: Schematic illustrating the quiet sun magnetic field structure over a vertical cross section. The arrows in the convection zone and photosphere show convective flows. The magnetic field grows out from the network concentrations and expands in higher atmosphere (solid lines) as a result of the drop in pressure with height. Therefore, the magnetic canopy is formed (dashed lines). Image credit: Wiegelmann et al. (2014), reproduced with under the terms of the CC BY license.

at the solar surface (e.g., Parker 1955; Babcock 1961; Schou et al. 1998). And this intricate magnetic field, is behind all the structures and dynamics in the solar atmosphere.

Figure 1.4 provides a 2-dimensional schematic of the quiet sun magnetic field through the lower atmosphere, demonstrating the two most common magnetic field structures, the open flux (left) and the closed loops (right). Below the photosphere, large-scale convective flows push the small magnetic bipoles towards the boundaries of supergranules, contributing to the concentrated magnetic flux with a strength of kilogauss. The magnetic field expands with height as a result of the decrease of gas pressure. Depending on the polarity of the nearby magnetic concentrations, it either bends over and connects back to the surface or reaches another expanding flux tube, both forming a "magnetic canopy", where horizontal field is much stronger than vertical field (Solanki and Steiner 1990; Schrijver and Title 2003). Below the canopy is an almost field-free sub-canopy region (e.g., Trujillo Bueno et al. 2004; Orozco Suárez et al. 2007) dominated by

shocks (e.g., Wedemeyer-Böhm and Wöger 2008). On the other hand, it is the canopy domain that represents the middle and upper chromosphere. There are many features and events involving energy transfer in this region, including shock waves, MHD waves and magnetic reconnections (e.g., Hansteen et al. 2006; De Pontieu et al. 2007a). Once reaching the corona, the magnetic field shapes the atmosphere and builds up and releases energy. Note that, the sub-canopy and canopy domains, in reality, are not strictly separated, e.g., there could be a smooth transition by small-scale loops. Also, the 3-dimensional magnetic field is certainly more complex.

As described, the magnetic field in the quiet sun is a mixture of both open and closed field lines rooted in the network concentrations. In the photosphere, the magnetic field strength can locally reach 1000–2000 Gauss inside of the network lanes while usually only a few hundreds Gauss in the center of the network cells (e.g., Beckers and Schröter 1968; Tarbell and Title 1977). Using Sunrise (Barthol et al. 2011) data, Lagg et al. (2010) reported that there are also kilogauss magnetic elements within the network cells. Different from the quiet sun, the active regions are dominated by very strong opposite polarities, connected with longer and higher loops. In the center of a sunspot, the magnetic field can be more than 2000 Gauss, even reach 4000 Gauss (Livingston 2002). The coronal holes are characterized by prevalently open unipolar magnetic flux. The average magnetic field strength in these regions varies from several Gauss to a few tens of Gauss (Harvey et al. 1982).

Magnetic fields are not static. Regardless of altitude or location, they exchange and transfer energy through interactions with one another and with the surrounding plasma. As the solar magnetic field is constantly twisted by the horizontal flows in the photosphere, the magnetic stress thus builds up in the chromosphere and the corona and the stored energy has to be released by restructuring the magnetic topology. This restructuring process, converting magnetic energy into other forms of energy, such as thermal energy and kinetic energy, is called magnetic reconnection. The magnetic reconnection processes are found to be significant not only in the solar atmosphere, but also in other astrophysical objects, like planetary magnetospheres, other stars, accretion disks and in laboratories.

Although magnetic reconnection is often described as a process of "breaking" and "reconnecting" of magnetic field lines, this statement can be misleading given that the divergence of the magnetic field is zero, so the magnetic field should always be closed. Several models have been proposed to explain the details of the reconnecting region, e.g., Sweet-Parker reconnection (Parker 1957; Sweet 1958) and Petschek reconnection (Petschek 1964). Here, a 2-dimensional model is introduced as a simplified example. Magnetic field lines with opposite direction components get closer to each other under external forces. As a result of the discontinuity in the magnetic field direction, a current sheet is generated around the neutral line. In this region with strong current, the local magnetic field is basically zero and the frozen-in condition of the charged particles breaks down due to resistivity or other non-ideal effects, allowing particles to move across magnetic field lines (this region is known as the diffusion region). The magnetic field tends to form a new topology with lower energy. The newly formed magnetic field lines, being highly curved, have a strong outward magnetic tension and can accelerate outflows under the slingshot effect. That is, the magnetic energy is converted into kinetic energy. Magnetic reconnection processes can occur in a quasi-steady way with a small inclination angle between field lines, which are usually considered to be important for coronal heating (e.g., Parker's braiding model, Parker 1972, 1983). It can also occur as sudden, intense events, manifesting as solar flares and CMEs (e.g., CSHKP models, Carmichael 1964; Sturrock 1966; Hirayama 1974; Kopp and Pneuman 1976).

In the photosphere, the measurement of magnetic field can be achieved by using the Zeeman effect (Hale 1908). It is the effect for which certain spectral lines are split into several components (splitting of the energy levels) when the emitting atom is exposed to a magnetic field. This is due to the interaction between the magnetic field and the magnetic moment of the atom, which causes the splitting of energy levels corresponding to different magnetic quantum numbers (J_Z) and affects the energy of the electrons in one of these sub-levels. The degree of splitting is proportional to the strength of the magnetic field. Photons emitted from transitions with $\Delta J_Z=1$ and $\Delta J_Z=-1$ exhibit opposite polarizations. Without an external magnetic field, these transitions are degenerate and have the same energy, leading to the emission of unpolarized light. However,

when a magnetic field is present, the energy levels are split, causing these transitions to occur at different energies, resulting in polarized spectral lines. A spectropolarimeter can detect the polarized light from the photosphere and the strength and direction of the magnetic field can be retrieved. However, it is much more challenging to measure the magnetic field in chromosphere and corona due to the weak magnetic field strength and the wider thermal broadening due to the high temperature. One substitute method is extrapolation (see Section 2.2.2 for more details), which makes use of observed magnetic field at photosphere as the bottom boundary condition to calculate the 3-dimensional magnetic field by solving the magnetohydrodynamic (MHD) equations (e.g., Sakurai 1989; Amari et al. 1997; Wiegelmann and Sakurai 2021). The structure and evolution of the magnetic field are essential to understand the physical processes of the observation phenomena.

1.2 The solar wind

The solar corona expands outward into space in the form of the solar wind, which is a continuous flow of charged particles, primarily electrons and protons. Solar wind travels outward through the solar system, carrying with it the Sun's magnetic field, and plays a crucial role in shaping the space environment around Earth and other planets. It eventually stops where the outward pressure of the solar wind balances with the inward pressure of the interstellar medium, forming the outer boundary of the heliosphere.

The idea of the solar wind originated from early observations of comet tails. Biermann and Schlüter (1951) proposed that their directions are due to particles streaming out from the Sun. Theoretically, Parker (1958) revolutionized solar physics by proposing explanation for why the Sun must have a wind, a continuous outflow of charged particles from the Sun's hot corona. Parker's main idea was that the corona is so hot and energetic that its particles are not bound by the Sun's gravity, causing them to escape and form a supersonic, outward-flowing wind. He also predicted that the Sun's rotation would cause this wind to carry the solar magnetic field in a spiral pattern. His prediction was, however, initially controversial but later proved by direct observations from early missions, e.g.,

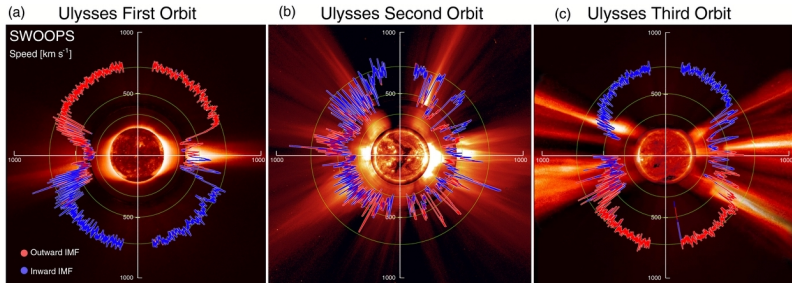


Figure 1.5: Solar wind speed measurements from the Ulysses spacecraft over three orbits around the Sun. Colors indicate the directions of the interplanetary magnetic field (IMF), i.e., red for outward IMF and blue for inward IMF. The first and third Ulysses orbits (panels (a) and (c)) took place at Solar Cycle 22 solar minimum and Solar Cycle 23 solar minimum, respectively and the second orbit (panel (b)) occurred at Solar Cycle 23 solar maximum. Image credit: McComas et al. (2013) ©AAS. Reproduced with permission.

Mariner II launched in 1962 (Neugebauer and Snyder 1967).

The Ulysses mission (1990-2009) provided groundbreaking observations of the solar wind, particularly from high solar latitudes, offering an unprecedented view of the Sun's polar regions. Unlike previous missions, Ulysses followed an orbit that allowed it to study the solar wind from both the equatorial and polar areas. Figure 1.5 shows the solar wind speeds measured by Ulysses at both solar minimum and maximum. It confirmed the existence of two distinct solar wind components: a fast, steady wind originating from the polar coronal holes and a slower, more variable wind from the equatorial regions. The solar wind is also continuously monitored at L1, a stable vantage point near Earth by spacecrafts like Wind (1994; Ogilvie and Desch 1997), Solar and Heliospheric Observatory (SOHO, 1995; Domingo et al. 1995) and Advanced Composition Explorer (ACE, 1997; Stone et al. 1998).

Here are some commonly accepted facts about the solar wind: 1) The solar wind is a continuous stream of charged particles, primarily electrons, protons, and alpha particles, that flow outward from the Sun's corona; 2) The solar wind travels at supersonic speeds, with two main types: the fast solar wind (around

700–750 km s⁻¹) and the slow solar wind (300–400 km s⁻¹); 3) The solar wind carries the Sun's magnetic field into space, forming the heliospheric magnetic field in a spiral shape (the Parker spiral) due to the Sun's rotation; and 4) The properties of the solar wind vary with the 11-year solar cycle, becoming more turbulent and denser during periods of high solar activity. At solar minimum, fast solar wind originates from polar coronal holes, while slow solar wind comes from low-latitude regions (see Figure 1.5 panels (a) and (c)). At solar maximum, the solar wind gets more irregular and variable, with both fast and slow solar winds being emitted at all latitudes (see Figure 1.5 panel (b)).

Meanwhile, not all mysteries about the solar wind are clearly solved. Two of the main open questions regarding the solar wind are those about its source regions and its acceleration mechanism. Fast solar wind is believed to originate from the coronal holes (e.g., Krieger et al. 1973; Zirker 1977), where the magnetic field is generally open, allowing plasma to escape easily. Hassler et al. (1999) reported the outflows within coronal holes to be associated with chromospheric network junctions. Tu et al. (2005) suggested that the solar wind originates from the height of 5–20 Mm above the photosphere in magnetic funnels. On the other hand, the origin of slow wind is more complicated. For example, Nolte et al. (1976) found that the slower wind may come out from smaller coronal holes. Neugebauer et al. (1998) also reported the slow wind linking to the small low-latitude coronal holes. Besides, the slow wind is suggested to originate from coronal hole boundaries (Wang et al. 1998b; Neugebauer et al. 1998; Wang and Sheeley 2006; Wang 2017), closed coronal loops (Wang et al. 1998a) or to be associated with active regions (Kojima et al. 1992; Hick and Jackson 1995; Hick et al. 1995).

Parker (1965) suggested that, purely driven by thermal pressure from the million-kelvin corona, the solar wind can only reach up to the low-to-intermediate speed as in observations. This suggests that the high-speed wind would definitely require an extra energy input to be accelerated. Some models suggested this acceleration is related to the propagating waves triggered by the photospheric convection motions (e.g., Cranmer et al. 2007). This idea is supported by the observations of spicules, jet-like structures dominating solar chromosphere, which may transport energy into the solar wind (De Pontieu et al. 2009, 2011; Martínez-

Sykora et al. 2018). Meanwhile, small-scale jets are frequently observed in the polar coronal holes in both X-ray and EUV/FUV channels (Cirtain et al. 2007; Paraschiv et al. 2015), indicating the role of magnetic reconnection in supplying energy flux (e.g., Axford and McKenzie 1992). In Chitta et al. (2023b), a large number of jets have been observed in coronal holes, generated through magnetic reconnection and characterized by kinetic energy within the picoflare energy range (picoflare jets). These outflows are believed to contribute hot plasma that helps sustain the solar wind.

1.3 Coronal heating problem

As described in the previous chapters, the temperature has been found to increase dramatically from about 5700 K in the photosphere to over 1 MK in the corona. Figure 1.6 shows how temperature and density change along with the height throughout the solar atmosphere as calculated from a 1-dimensional model (which would be a reasonable representation of a large coronal loop) and it is clear that both parameters change dramatically in the transition region. The mechanism behind that, however, is not fully understood yet. This is the so-called "corona heating problem", one of the most intriguing mysteries in solar physics nowadays. This chapter will focus on how the corona's high temperature was discovered at the first place and introduce some of the possible heating mechanisms.

1.3.1 Discovery of the corona's temperature

Although the solar corona can be observed during total solar eclipses, its temperature remained unknown for a long time. The first major clue about the corona's high temperature came from spectroscopic observations. In 1869, during a solar eclipse, Charles Augustus Young and William Harkness independently discovered a bright green emission line in the corona at 530.3 nm. However, the line could not be identified with any known element at that time. Only after decades, German physicist Walter Grotrian and Swedish physicist Bengt Edlén made a breakthrough in determining that this line and another coronal line in the red

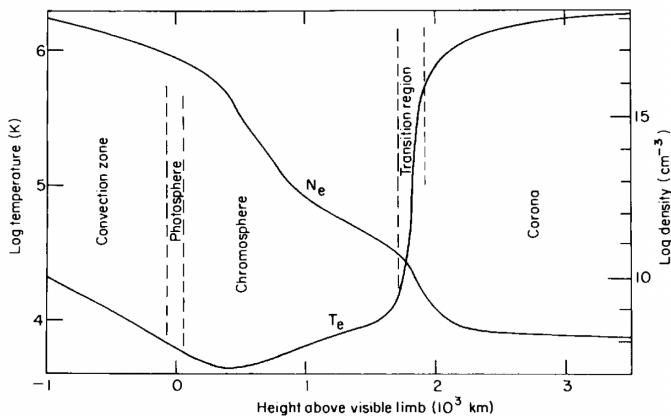


Figure 1.6: Changes in temperature and density across different altitudes in the solar atmosphere. Image credit: Gabriel and Mason (1982), reproduced with permission from Elsevier.

at 637.4 nm are coming from multiple times ionized iron, i.e., Fe XIV (530 nm) and Fe X (637.4 nm), which could only exist at very high temperatures (Grotrian 1939; Edlén 1943, 1945). These two lines are also dubbed as the coronal green line and red line, and are the two strongest emission coronal lines at visible wavelengths.

With the development of space-based instrumentation, the ability to observe the Sun in the EUV and X-ray wavelengths from above the Earth atmosphere greatly expanded our understanding of the corona. For instance, early missions from the 1960s to 1970s like Orbiting Solar Observatory (OSO), and Skylab in the 1970s provided detailed long-term observations of the corona in high-energy wavelengths. These observations confirmed that the corona was filled with hot, million-degree plasma. Skylab, in particular, provided some of the first observations showing active regions and coronal loops filled with hot plasma (Bray et al. 1991). It became clear that different regions of the corona could reach temperatures of 1–3 MK, with some flaring regions getting even temporarily hotter.

1.3.2 Energy Requirements

The energy source required to maintain the corona at a high temperature has to balance the energy loss by radiation and thermal conduction, and by the solar wind in the coronal holes, while all these three energy rates (in units of $\text{erg cm}^{-3} \text{s}^{-1}$) highly depend on the spatial location. The required energy rate can be theoretically predicted using the Rosner, Tucker & Vaiana (RTV) scaling laws (Rosner et al. 1978), which assumes hydrostatic loops with uniform heating and no gravity. Combining these scaling laws with the ideal gas law, the heating rate is found to strongly depend on the density $E_{H0} \propto n_e^{7/4}$. A similar scaling law of $E_{H0} \propto n_e^2$ can be reached by simply considering only radiative loss, for that the radiative loss rate can be written as:

$$E_R \approx n_e^2 \Lambda(T) \quad (1.2)$$

where $\Lambda(T)$ is the radiative loss function, depending on the temperature. In the temperature range of 0.5–3 MK, $\Lambda(T)$ can be approximated as a constant $10^{-22} \text{ erg cm}^{-3} \text{ s}^{-1}$. The heating flux (in units of $\text{erg cm}^{-2} \text{ s}^{-1}$) at the base can be derived as an integration of the volumetric heating rate over height.

Revisiting the 26 August 1992 observation from the Yohkoh soft X-ray telescope (SXT; Tsuneta et al. 1991), which was reported by Aschwanden and Acton (2001), Aschwanden (2001) shows the spatial distribution of the heating requirement by considering the balance between heating rate and radiative loss, providing observational constraints for heating models. The heating requirement is estimated to be 2×10^5 – $2 \times 10^6 \text{ erg cm}^{-2} \text{ s}^{-1}$ for active regions, 1×10^4 – $2 \times 10^5 \text{ erg cm}^{-2} \text{ s}^{-1}$ for quiet sun and 5×10^3 – $1 \times 10^4 \text{ erg cm}^{-2} \text{ s}^{-1}$ for coronal holes. Their results are in agreement with the radiative loss reported by Withbroe and Noyes (1977) (see Table 1.1, where they list all the energy loss rates in the chromosphere and corona and can be used as a benchmark for evaluating heating models). What can be further seen in Table 1.1 is that in both the active region and the quiet sun corona, the radiative loss and conductive loss are comparable. Differently, the radiative loss is significantly lower compared to the conductive loss in coronal hole regions due to the lower density and large solar wind flux.

Table 1.1: Chromospheric and coronal energy losses ($\text{erg cm}^{-2} \text{s}^{-1}$), used with permission of Annual Reviews, Inc., from Withbroe and Noyes (1977); permission conveyed through Copyright Clearance Center, Inc.

Parameter	Quiet sun	Coronal hole	Active region
Transition layer pressure (dyn cm^{-2})	2×10^{-1}	7×10^{-2}	2
Coronal temperature (K, at $\approx 1.1 R_{\odot}$)	$1.1-1.6 \times 10^6$	10^6	2.5×10^6
Coronal energy losses			
- Conduction flux F_c	2×10^5	6×10^4	10^5-10^7
- Radiative flux F_r	10^5	10^4	5×10^6
- Solar wind flux F_w	$\lesssim 5 \times 10^4$	7×10^5	$(< 10^5)$
- Total corona loss $F_c+F_r+F_w$	3×10^5	8×10^5	10^7
Chromospheric radiative losses			
- Low chromosphere	2×10^6	2×10^6	$\gtrsim 10^7$
- Middle chromosphere	2×10^6	2×10^6	10^7
- Upper chromosphere	3×10^5	3×10^5	2×10^6
- Total chromospheric loss	4×10^6	4×10^6	2×10^7
Solar wind mass loss ($\text{g cm}^{-2} \text{s}^{-1}$)	$\lesssim 2 \times 10^{-11}$	2×10^{-10}	$(< 4 \times 10^{-11})$

1.3.3 Heating mechanisms

The time scale of photospheric convection is $\tau_c = l/v_{ph}$, where l is the horizontal scale (e.g., 1 Mm, considering the size of granules) and v_{ph} is the velocity of photospheric convection (of the order of $1\text{--}2\text{ km s}^{-1}$). The Alfvén time is $\tau_A = (2)L/v_A$, where L is the loop length (e.g., typically ranging from a few to several tens of megameters in the quiet sun and extending up to several hundreds of megameters in active regions) and v_A is the Alfvén speed, the speed at which the Alfvén wave propagates. The Alfvén speed $v_A = B/\sqrt{\mu_0\rho}$ is related to the magnetic field strength B and to the plasma density ρ . μ_0 is the magnetic permeability. By comparing τ_c and τ_A , the coronal heating models are usually categorized into DC (Direct Current) models and AC (Alternating Current) models. In DC models, a slow mechanical driver is required, so the coronal loops can adjust to the changes in the photosphere quasi-statically. This can lead to the misalignment of magnetic fields and produce current sheets and reconnection. In comparison, if the photospheric driver changes too fast for coronal loops to adjust to, disturbances are triggered to carry information into the corona, which is usually by means of MHD waves. In both model types, many ways of how the energy is transported and dissipated are proposed, but not all of them can be verified with observations. Here, I mainly talk about two representative mechanisms, i.e., wave heating mechanism and nanoflare or reconnection heating mechanism. More and more studies suggest that both mechanisms can contribute to heating up the corona but not to the same extent in different regions, e.g., active regions, quiet sun and coronal holes.

1.3.3.1 Heating by waves

Biermann (1948) and Schwarzschild (1948) were the first to attempt explaining the high temperature of the corona with acoustic waves, generated by the hypothesized turbulence in the convection zone, before the omnipresent p-mode oscillation was first observed in 1970s. Once the acoustic waves propagate outward, they encounter a density drop and steepen into shock waves. However, the shock waves are found to mostly dissipate to heat up the chromosphere but not to reach the corona. With UV spectroscopic data from OSO-8, Athay and

White (1978, 1979) show that the flux of sound wave is no more than about $10^4 \text{ erg cm}^{-2} \text{ s}^{-1}$, which is 2–3 orders of magnitude smaller than the energy required to heat up the corona. De Moortel et al. (2000) showed that although the acoustic waves can propagate into coronal loops, not enough energy flux is carried for coronal heating.

As the solar atmosphere is highly magnetized, acoustic waves are then naturally extended to MHD waves. Photospheric convection generates enough waves (Narain and Ulmschneider 1996), but the challenge is in how the MHD waves can propagate to the corona and efficiently dissipate there. MHD waves have three modes, slow magnetoacoustic waves, fast magnetoacoustic waves and Alfvén waves. The slow-mode wave easily grows into a shock wave and damps already in the chromosphere. The fast-mode wave, however, is less influenced by non-linear effects and can reach the corona. On the other hand, Hollweg (1978) suggests that fast modes tend to reflect and refract in the lower atmosphere. Some authors (e.g., Banerjee et al. 1998; Doyle et al. 1999) by studying the line broadening from observations provided by the Solar Ultraviolet Measurements of Emitted Radiation (SUMER; Wilhelm et al. 1995) and by the Ultraviolet Coronagraph Spectrometer (UVCS), on board SOHO, reported that the Alfvén wave has no such problem and can propagate into the corona. Moreover, the energy flux carried by Alfvén waves can be estimated to be around $4 \times 10^6 \text{ erg cm}^{-2} \text{ s}^{-1}$, sufficient for heating quiet sun and coronal hole regions and even some active regions. However, Alfvén waves cannot efficiently dissipate in a uniform medium, thus it requires other dissipation mechanisms like phase mixing or resonant absorption. It is worth mentioning that the problem of effective wave propagation is only relevant when considering waves formed in the lower atmosphere, as waves can also be generated directly in the corona.

From the observational point of view, different wave motions have been detected in the corona, such as periodic propagating disturbances, type II spicule oscillations and transverse waves. For instance, observations from SOHO and Transition Region and Coronal Explorer (TRACE; Handy et al. 1999) show low-frequency propagating disturbances in the corona, which are identified as slow-mode waves (e.g., De Moortel et al. 2000; Verwichte et al. 2010). However, these waves carry far too little energy to account for coronal heating. Type II spicules

are jet-like chromospheric structures, which can potentially provide energy and mass supply into the corona (e.g., De Pontieu et al. 2009, 2011), but their role in coronal heating is challenged by Klimchuk (2012). He suggested that only a trivial fraction of hot plasma can be transported into the corona by spicules, and, at the same time, the hot material cools down rapidly. Transverse waves have been detected with observations from Coronal Multi-channel Polarimeter (CoMP, Tomczyk et al. 2008) in coronal loops (Tomczyk et al. 2007; Tomczyk and McIntosh 2009). These CoMP waves show a very small velocity amplitude of 0.5 km s^{-1} , thus do not carry enough energy. However, the amplitude could be underestimated because of the low spatial resolution of CoMP. McIntosh et al. (2011) used high-resolution observations and found a much higher velocity of about 20 km s^{-1} in these transverse waves, which supply enough energy for quiet corona, but not enough for active regions.

1.3.3.2 Heating by magnetic reconnection

As described in Section 1.1.3, magnetic reconnection is a fundamental process where magnetic field lines with opposite or partially-opposite directions restructure, releasing a large amount of energy. The main effects of magnetic reconnection involve 1) heating plasma by Ohmic dissipation; 2) accelerating plasma to gain bulk kinetic energy and 3) accelerating high-speed particles. In addition to its role in large-scale energy release like solar flares and CMEs, magnetic reconnection also offers a compelling explanation for various small-scale flare-like phenomena in the solar atmosphere. These events can be categorized according to their thermal energy content. Large flares ($\varepsilon_{th} = 10^{30} - 10^{33} \text{ erg}$) can be observed in EUV and soft X-ray channels and can produce non-thermal emission (hard X-ray). Microflares ($\varepsilon_{th} = 10^{27} - 10^{30} \text{ erg}$) are observable in EUV and soft X-ray, such as X-ray bright points, X-ray jets and active region bright points. Nanoflares ($\varepsilon_{th} = 10^{24} - 10^{27} \text{ erg}$) are observed in EUV with a temperature of not more than 2 MK. Besides, as mentioned before, transients are also observed in the transition region with a lower temperature, such as explosive events and blinkers.

The importance of the small events lies in that both observations and theoretical models suggest that the occurrence of heating events follows a power-law

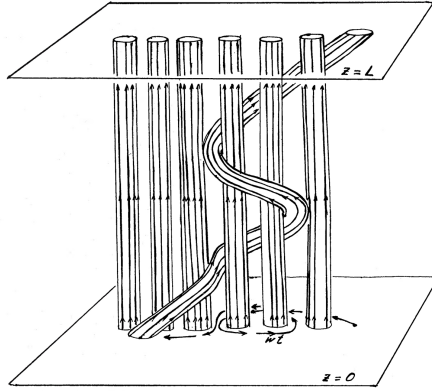


Figure 1.7: Sketch of magnetic field tubes being twisted by the random-walk motion of their footpoint at $Z=0$. Image credit: Parker (1983), ©AAS. Reproduced with permission.

distribution, as $N(E) \propto E^{-\alpha}$, where E is the energy of an individual flare, $-\alpha$ (α is positive) is the power-law index and $N(E)$ is the event frequency. This means that, small, low-energy events happen much more frequently than large, high-energy events and if α is greater than 2, the total energy input in coronal heating is dominated by the events on the low-energy side. In order to achieve frequent enough heating events to heat up the corona, different models have been suggested. Such models must not only ensure that magnetic energy is released efficiently through magnetic reconnection, but also incorporate a general-enough driving mechanism to produce a high frequency of events.

In Parker's braiding heating model (Parker 1972, 1983, 1988), the random walk of photospheric footpoints can tangle the magnetic fields to a non-potential topology to store energy (see Figure 1.7). Naturally, current sheets are formed to dissipate energy and reconnections happen, transferring magnetic energy into both thermal and kinetic energy. Parker (1983) made an estimation of the energy build-up rate by twisting magnetic flux tubes by random walk and found it to be $dW/dT = 10^7 \text{ erg cm}^{-2} \text{ s}^{-1}$. Assuming that the footpoint motion is slow enough to not break the accumulated stress for about 1 day, the dissipated energy is

sufficiently high compared with nanoflare observations. Thus, the braiding model is also called nanoflare model. The term "nanoflare" derives from the fact that the energy they release is approximately nine orders of magnitude smaller than that of the largest flares.

However, the braiding model is not the only one that produce nanoflares. For example, Priest et al. (2002b) suggested a magnetic carpet model. The Sun's surface is covered by small magnetic flux tubes that are constantly emerging, evolving, and disappearing over short timescales (Schrijver et al. 1997) and extend into the chromosphere and corona, known as the magnetic carpet. The magnetic fluxes linking different magnetic concentrations are considered separated by separatrix surfaces, which define the boundary between regions of different magnetic connectivity. Thus, even only a simple displacement of foot-points can produce opposite field on the two sides of the separatrix surfaces, generate current sheets and produce uniform heating.

Another phenomenon that is an example of coronal heating are X-ray bright points (XBPs). They are usually found in the corona above emerging polarities or opposite polarities approaching each other and canceling, which is regarded as a hint of reconnection. The flux cancellation and consequent XBPs can be well explained with the converging flux model (Priest et al. 1994; Parnell and Priest 1995). In a supergranular cell, magnetic flux emerges and shifts toward the boundary, where it interacts with a flux concentration with the opposite polarity. A null-point or separator develops when opposite-directed magnetic fluxes approach each other closely. Therefore, reconnection occurs to form a bright point, trigger outflowing jets (Shibata et al. 1992; Shimojo et al. 2007) and cause the null point to submerge back into the photosphere. Actually, recent studies have suggested that magnetic cancellations happen much more often than previously expected, and thus could power the solar corona more efficiently (Chitta et al. 2017; Priest et al. 2018).

1.4 Small-scale dynamic events

As mentioned above, small-scale dynamic events can provide vital insights into the processes responsible for heating up the corona and heating/accelerating the

solar wind. These events, though are individually small, occur frequently and ubiquitously across the solar atmosphere. Thus, they could be one of the major drivers of the energy transfer and transport. In this chapter, we introduce different small-scale events from the observational point of view in the categories of brightenings (localized temperature change or density enhancements) and jet-like events (outflows). Note that, this categorization does not mean that brightenings and jets are entirely separated physical processes. Actually, as already found in the large-scale events, flaring events and eruptions usually accompany each other.

1.4.1 Brightenings

CBPs are small and compact regions in the corona that emit enhanced radiation. They were initially identified through X-ray observations (XBPs) and later detected also in EUV wavelengths. XBPs were first described as small-scale point-like features (Vaiana et al. 1973a) and are a case of hot low-lying magnetic loops outside of active regions (Vaiana et al. 1973b). With the launch of SOHO, observations of XBPs extended to FUV and EUV channels. Figure 1.8 panel (a) shows an example observation from the Extreme-ultraviolet Imaging Telescope (EIT; Delaboudinière et al. 1995) onboard SOHO, where many bright points are identified in a quiet sun region. Later, the high-resolution observations from TRACE distinguished the EUV bright points as multi-loop structures. Finally, imaging data from the Atmospheric Imaging Assembly (AIA; Lemen et al. 2012) on board the Solar Dynamic Observatory (SDO; Pesnell et al. 2012) and spectral data from the Interface Region Imaging Spectrograph (IRIS; De Pontieu et al. 2014) revealed the evolution of the small-scale loops at different temperatures (e.g., Kayshap and Dwivedi 2017).

Golub et al. (1977) reported that the linear size of XBPs as seen from Earth's orbit, varies from $20''$ to $30''$, with a bright core of $5''$ to $10''$. Using AIA data (195\AA), Mou et al. (2018) followed the whole evolution of CBPs and found them first emerging as small loops with a minimum length of $5''$ and evolving to reach a size of up to about $60''$. The average lifetime of CBPs also varies over a relatively large range, from about 8 hours in X-ray wavelengths (Golub et al.

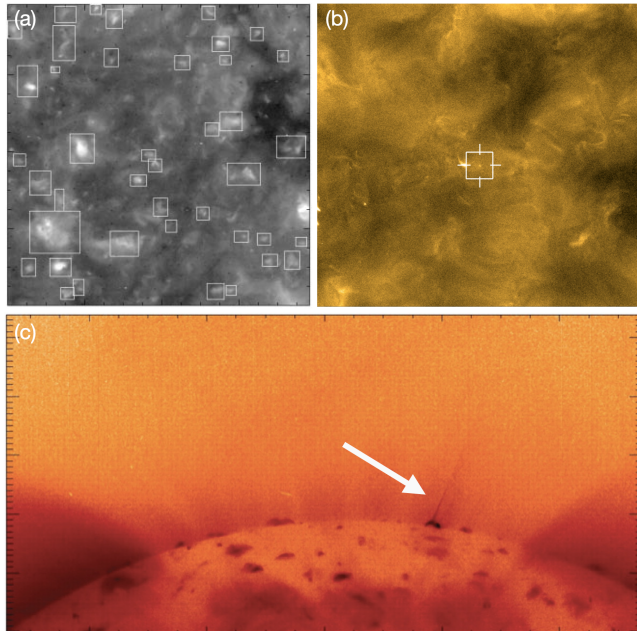


Figure 1.8: (a) SOHO EIT image (195\AA , $\sim 1.5\text{ MK}$) of a quiet sun region with numerous CBPs identified and marked. Image credit: Zhang et al. (2001), reproduced with permission from Springer Nature; (b) Solar Orbiter HRI_{EUV} (174\AA , $\sim 1\text{ MK}$) observed the smallest and weakest brightenings dubbed "campfires". Image credit: Berghmans et al. (2021), reproduced with permission $\text{\textcircled{C}}$ ESO; (c) Hinode XRT image ($2\text{--}200\text{\AA}$, $> \sim 1\text{ MK}$) in negative color of the polar region where a jet can be clearly observed (see the white arrow). Image credit: Certain et al. (2007), reprinted with permission from AAAS.

1974) to 20 hours in EUV wavelengths (Zhang et al. 2001). Habbal and Withbroe (1981) estimated the energy loss rate of one CBP to be $1.4 \times 10^{24} \text{ erg s}^{-1}$. The total energy losses of the CBPs studied in Preš and Phillips (1999) during their lifetimes are from 4.5×10^{28} to 2.6×10^{29} erg, with the radiative loss contributes only about 10%. CBPs are related to the magnetic flux of opposite polarities, either newly-emerged or pre-existing. Both flux emergence and cancellation have been found associated with the occurrence of CBPs. It is believed that two thirds of the bright points appear above canceling magnetic elements, leading to the idea of the converging flux model where the evolving flux consequently triggers reconnection to produce CBPs (Priest et al. 1994).

CBPs are commonly distributed all over the Sun. In the statistics of 518 CBPs in Harvey et al. (1993), 60% were located in quiet sun regions, 34% in coronal holes while the remaining 6% in active regions. Despite their locations, some CBPs are found to be related to flaring and eruptions. Strong et al. (1992) showed the large enhancement of X-ray emission of CBPs and outflows with velocities of $300\text{--}1000 \text{ km s}^{-1}$. Mou et al. (2018) also studied eruptive activities, e.g., microflares, mini-filaments and mini-CMEs and highlighted the role of reconnection between newly-emerged flux and existing magnetic field in triggering the small eruptions.

Nanoflares are the weakest, coolest and least dense events in the flare family. They are defined in Parker's braiding hypothesis of 1988 to explain the coronal heating. However, no observational proof could be found until the late 1990s, not until after the launch of SOHO and TRACE. Due to their small-scale nature, high sensitivity is definitely required for the study of nanoflares. Most of the work was thus conducted with EIT/SOHO, TRACE or AIA/SDO. These observations revealed that nanoflares are usually associated small loops, with a short lifetime of a few minutes and have a typical temperature range of $1\text{--}1.5 \text{ MK}$. Since they can barely reach up to 2 MK , usually no obvious signature can be detected in X-ray wavelengths. Chae et al. (1999) also found accompanying outflows together with the nanoflares. Berghmans et al. (2021) reported the smallest brightening events that have been observed, the so-called "campfires", detected with the EUV High Resolution Imager (HRI_{EUV}), part of the Extreme Ultraviolet Imager (EUI; Rochus et al. 2020) on board solar orbiter (Müller et al. 2020). Examples

can be found in Figure 1.8 panel (b).

To study the contribution of nanoflares to the energy requirement of coronal heating, many statistical studies have been conducted, resulting in different power-law indexes of the distribution of heating events. For example, Krucker and Benz (1998) found a power-law index ($-\alpha$) smaller than -2 and Berghmans et al. (1998) also concluded on a power-law index close to -2 (-1.9 ± 0.1). Both suggest that the majority heating energy is supported by small events. However, Aschwanden and Parnell (2002) reported a power-law index of about -1.54. In Joulin et al. (2016), a power-law index of -1.65 and -1.73 have been found for active region and quiet sun, respectively. The disagreement, could be attributed to the insufficient spatial resolution, narrow temperature range of the instruments and different algorithms used for detecting events. It is pointed out by Pauluhn and Solanki (2007) that the weak events can easily be missed in observations, merging together as a background, which leads to a power law index too biased towards positive values. Their simulation is consistent with the time series data measured by SUMER with power-law index less than -2 (i.e., the largest heating contribution is from the smallest events).

1.4.2 Jet-like events

If brightenings are considered as local plasma heating and can thus support the hot corona, the potentially related mini-eruptions, usually in the form of jet-like structures, are a candidate for supplying mass and energy to power both corona and solar wind. Jets with both cool and hot plasma have been studied, e.g., $H\alpha$ surges (Roy 1973), EUV jets or surges (Schmahl 1981) and X-ray jets (Shibata et al. 1992). $H\alpha$ surges are mass ejection from the bright footpoint of flaring events in the chromosphere. They move with velocities of $20\text{--}200 \text{ km s}^{-1}$ and can last for 10–20 min. EUV jets were first considered as the EUV signature of $H\alpha$ surges because of their spatial correlation (Schmieder et al. 1988) but this idea was later challenged because their exact temporal and spatial correspondence is not clear (e.g., Canfield et al. 1996). Results by Chae et al. (1999) also support that EUV jets and $H\alpha$ surges are not the hot and cool components of the same plasma ejection, but EUV jets may have a similar formation process as X-ray

jets, involving magnetic reconnection (Yokoyama and Shibata 1995, 1996).

From 1991 to 2001, the Yohkoh SXT had been providing continuous observations of the full disk of the Sun. It first unveiled the existence of the X-ray jets, the eruptions accompanying XBPs. These jets can be found in active regions (Berghmans et al. 2001), showing velocities varying from 10 to 1000 km s^{-1} . More often, they are seen emanating from coronal holes as the magnetic field there is more vertical and open and thus can more easily release energy and mass into space, contributing to the solar wind. Figure 1.8 panel (c) shows an example of an X-ray jet from a polar coronal hole. These jets, dubbed polar jets as they commonly appear in the large polar coronal holes, are found to be related to the formation of plumes (Raouafi et al. 2008), which are the long, thin, streamer-like features that extend from the coronal holes into the solar corona. High-resolution observations show that plumes are embedded with fine structures like bright points and small jets (so-called jetlets).

Spicules, as introduced in Section 1.1.2.2 and 1.3.3.1, are dynamic, jet-like structures that are typically found in the chromosphere and propagate higher up towards the corona. For this reason, spicules are considered to be an important candidate in establishing a connection between the chromosphere and the corona. Spicules are of two types (De Pontieu et al. 2007b). Type I spicules are relatively slow with a velocity of $20\text{--}50 \text{ km s}^{-1}$ and can exist for 3–7 min. They can be well observed at the solar limb, needling into the hot corona and then falling down back to the surface. Dynamic fibrils are similar structures but observed on-disk (Hansteen et al. 2006). The type I spicules are usually believed to be caused by the magnetoacoustic shocks generated by the magnetic flux concentrations and global photospheric oscillation (De Pontieu et al. 2004; Hansteen et al. 2006; De Pontieu et al. 2007a). As Type I spicules return back to the surface and they have temperatures typically ranging from 5000 to 15000 K, their contribution to coronal heating and solar wind should be minor.

Differently, type II spicules usually show a larger speed of $40\text{--}100 \text{ km s}^{-1}$ and have a shorter lifetime of 1–2 min. After that, they dissolve rapidly instead of dropping back. They can also be detected as rapid blueshifted excursions (RBEs) on disk (Langangen et al. 2008; Rouppe van der Voort et al. 2009). Previous studies (e.g., Pereira et al. 2014; Henriques et al. 2016) found the signature of

RBEs or type II spicules being heated to at least transition region temperatures and Henriques et al. (2016) also found EUV signatures of RBEs in AIA 304Å and 171Å, indicating their relation with coronal heating events. The formation of the type II spicules is usually considered to relate to magnetic reconnection processes (De Pontieu et al. 2007b; Langangen et al. 2008). The oscillations of type II spicules, as a potential evidence of propagating waves, are discussed in Section 1.3.3.1.

1.5 Motivation of this thesis

Exploring the Sun does not only allow gaining knowledge of the Sun itself, but also provides insight into what drives many of the dynamic processes within the solar system and governs space weather which has significant effects on Earth. It is also essential for fundamental science like stellar physics and plasma physics, as it serves as a model for other stars and a natural laboratory for studying plasma behavior.

Despite the many breakthroughs in solar physics over the past decades, there are still unsolved mysteries. Two of the main open questions are the mechanisms behind coronal heating and the formation of the solar wind. Small-scale events, such as micro- and nano-flares, small jets and spicules are found to be crucial because they can release substantial energy and mass into the corona. Despite their localized nature, the collective contributions of these ubiquitous events may provide the missing link to explain the million-kelvin corona and the high-speed solar wind.

Considering that these events are extremely small in size, short in duration and super dynamic, higher temporal and spatial resolutions are definitely required to capture their formation and evolution. Many advancements in observational techniques have been achieved in only a few decades. Skylab (1973–1974) provided the first detailed X-ray images, unveiling that the solar corona is packed with plasma loops. The Japanese mission Yohkoh (1991) provided Soft X-ray images with a spatial resolution of 5'' over the full sun and 2.5'' over a selected field of view. The full-disk images in EUV wavelengths were recorded by EIT/SOHO (1995) with a spatial resolution of 2.5''. Launched in 1998, TRACE provided

EUV imaging observations of parts of the solar disk with an unprecedented resolution of about $1''$. Stepping into the 21st century, more advanced missions, both spacecraft such as Hinode (2006; Kosugi et al. 2007), SDO (2010), IRIS (2013) and Parker Solar Probe (PSP, 2018; Raouafi et al. 2023) and ground-based observatories such as the 1-meter Swedish solar telescope (SST, 2002; Scharmer et al. 2003), the 1.5 meter solar telescope GREGOR (2012; Schmidt et al. 2012) and the Daniel K. Inouye Solar Telescope (DKIST, 2020; Rimmele et al. 2020), have been utilized for providing more accurate observations (remote-sensing and in-situ) in multiple wavelengths, which undoubtedly enhance our understanding of the small-scale events.

More opportunities have been opened by the Solar Orbiter, which is a European Space Agency (ESA) and National Aeronautics and Space Administration (NASA) mission, launched in February 2020. It is designed to study the solar magnetized atmosphere from up close to the Sun and at different angles with Earth-bound facilities and, later in the mission, from viewpoints high over the ecliptic plane which will offer unprecedented views of the solar poles. Aboard Solar Orbiter, the Polarimetric and Helioseismic Imager (SO/PHI; Solanki et al. 2020), the EUV Imager and the EUV Imaging Spectrograph (SPICE; SPICE Consortium et al. 2020) are capable of respectively measuring the variation of the magnetic field (SO/PHI), the emission response arising from the solar chromosphere and corona (EUI) and the evolution of the thermodynamic state of the plasma (SPICE) thus providing the possibility of tracking the response of the plasma to the field evolution and of establishing the relevance of the observed dynamic events to the energetics of the solar corona.

HRI, in particular, has revealed the existence of ubiquitous brightening and dynamics down to the temporal and spatial resolution of the instrument (e.g., Berghmans et al. 2021; Mandal et al. 2023). This confirms that the higher-resolution observations can bring our understanding of solar dynamic events to smaller scales and inspires more studies to be conducted. The main question is to understand their physical characteristics, generation and evolution mechanisms and possible contributions to powering the corona and solar wind.

This thesis work combines different types of data provided by Solar Orbiter, specifically, EUV imaging data from EUI, spectral data from SPICE and magnetic

field data from SO/PHI, to study small-scale dynamics in both quiet sun regions and coronal holes. The scales of these events are likely to be close to the limits of the observational capabilities of the instruments (EUI and SPICE), meaning that they were largely unknown in detail until the data from Solar Orbiter were examined. The goal is to collocate the studied events in the framework of the various UV dynamic events present in the literature, to shed light on the mechanism behind them (e.g., magnetic reconnection and waves), and to assess their overall relevance to the energetic budget of the corona and its extension. This enables a more comprehensive understanding of solar phenomena. It also helps in the design of future observations with currently operating instruments, e.g., AIA and the Helioseismic and Magnetic Imager (HMI; Scherrer et al. 2012) (on board SDO), IRIS, DKIST and PSP.

The very small sizes and fast evolution of these events would also require a significant evolution in EUV spectroscopic capabilities with respect to what can be currently provided by instruments like IRIS, SPICE and EIS/Hinode. A new generation of instruments is currently being built to answer this need. The Extreme Ultraviolet Spectroscopic Telescope (EUVST) aboard the Solar-C mission (Shimizu et al. 2020) will be able to scan over these events in seconds and with a spatial resolution of $0.4''$ while being capable of simultaneously record spectral lines formed over all relevant temperatures, from the 20000 K of the chromosphere to the >10 MK of flaring plasma. At the same time, the Multi-slit Solar Explorer (MUSE; Cheung et al. 2019; De Pontieu et al. 2020) will be able to scan the regions of interest at even higher cadence, but on a limited number of spectral lines. The work presented in this thesis also allows defining the kind of observations EUVST and MUSE will provide to solve the science problems treated here.

Chapter 2

Instruments and Methods

2.1 Solar Orbiter

Solar Orbiter is a pioneering space mission launched by ESA in collaboration with NASA on 10 February 2020 04:03 UTC, with an Atlas V 411 rocket provided by NASA. Its unique orbit takes it as close to the Sun as 0.28 au and will make it possible to look at the Sun's poles from out-of-ecliptic vantage points (achieving an inclination angle of 18° already in the nominal mission phase and 33° in the extended phase), allowing for unprecedented observations of solar phenomena. Solar Orbiter is planned for a nominal mission duration of 7 years, followed by a three-year extended mission.

Its primary objective is to address the key scientific questions in solar physics "How does the Sun create and control the Heliosphere – and why does solar activity change with time?" A more detailed science overview can be found in Müller et al. (2013) and Müller et al. (2020), where they also expand the main scientific objective into four concrete questions:

- 1) What drives the solar wind and where does the coronal magnetic field

originate?

2) How do solar transients drive heliospheric variability?

3) How do solar eruptions produce energetic particle radiation that fills the heliosphere?

4) How does the solar dynamo work and drive connections between the Sun and the heliosphere?

Solar Orbiter presents a distinctive advantage in addressing these challenges. For example, the close proximity to the sun at perihelia and the high-resolution instruments can provide evidences for small-scale features that potentially relate to the coronal heating and solar wind. The combination of both in-situ data and remote sensing data makes it possible to trace the solar wind back to the Sun's surface. Solar Orbiter will also provide observations of the Sun's polar regions and solar magnetograms recorded from a new perspective than from the direction of the Earth for the first time.

For these purposes, Solar Orbiter carries as payload a suite of ten advanced instruments that allow it to capture high-resolution images of the Sun and collect data on its outer atmosphere and solar wind. Figure 2.1 illustrates the design of the spacecraft and highlights the locations of the instruments onboard. There are four in-situ instruments, the Energetic Particle Detector (EPD; Rodríguez-Pacheco et al. 2020), the Magnetometer (MAG; Horbury et al. 2020), the Radio and Plasma Wave analyser (RPW; Maksimovic et al. 2020) and Solar Wind Analyser (SWA; Owen et al. 2020) and six remote-sensing instruments, the Visible light and UV Coronagraph (Metis; Antonucci et al. 2020), the X-ray Spectrometer/Telescope (STIX; Krucker et al. 2020), the Extreme Ultraviolet Imager (EUI; Rochus et al. 2020), the Polarimetric and Helioseismic Imager (SO/PHI; Solanki et al. 2020) and the EUV Imaging spectrograph (SPICE; SPICE Consortium et al. 2020). In this section, I will introduce the three of them (EUI, SPICE and SO/PHI) that provide most of the data that are used in this work.

2.1.1 EUI: The Extreme Ultraviolet Imager

The EUI instrument is designed to capture high-resolution images of the solar atmosphere in EUV wavelengths. It consists of three telescopes, the Full

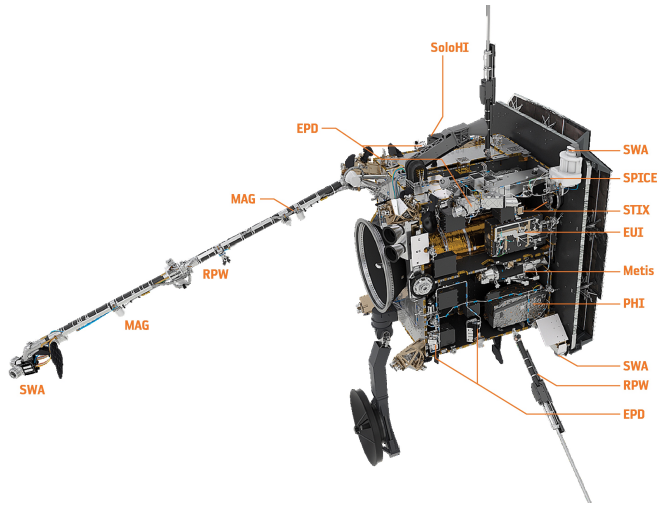


Figure 2.1: The Solar Orbiter payloads. Image credit: Müller et al. (2020), reproduced with permission © ESO.

Sun Imager (FSI) and two High Resolution Imagers, one covering the Lyman- α ($\text{HRI}_{\text{Ly}\alpha}$) line and the other observing at Fe x line at 174\AA at EUV (HRI_{EUV}) wavelengths. They observe at different spatial and temporal resolutions and cover different temperatures from chromosphere to corona, enabling the thorough investigation of multi-scale dynamics. All telescopes are designed to fulfill the scientific requirements within limited space and weight constraints. EUI applies the novel complementary metal-oxide-semiconductor Active Pixel Sensors (CMOS-APS) considering the power limitation and the radiation-heavy environments.

The characteristics of the telescopes are given below (A summary can be found in Table 2.1):

FSI: The FSI applies a single off-axis mirror (Herschelian telescope). It is designed with a large field of view (FOV) of $3.8^\circ \times 3.8^\circ$ with an angular resolution of about $9''$ (two pixels). It provides a good tolerance for the pointing of the spacecraft. It operates in two primary EUV wavelengths, 30.4 nm and 17.4 nm , which are respectively dominated by the emission lines from He II and Fe IX-X,

Table 2.1: Characteristics of the telescopes of EUI

Parameters	FSI	HRI _{EUV}	HRI _{LYa}
Field of view	3.8° × 3.8°	1000'' × 1000''	1000'' × 1000''
Plate scale	4.44''	0.492''	0.514''
Maximum cadence	10 s	<1 s	<1 s
Wavelength	30.4, 17.4 nm	17.4 nm	H I Ly- α (121.6 nm)
Detector	3072 × 3072	2048 × 2048	2048 × 2048

observing both the transition region and the corona. The mirror has a Al-based multi-layer coating with a dual band response with peaks centered at 30.4 nm and 17.4 nm. The wavelength selection is then done by operating a filter wheel with two types of filters. The Al/Zr/Al filter is used to select the 17.4 nm peak and the Al/Mg/Al filter for the 30.4 nm one. The filter wheel can be placed in an intermediate blocking position to protect the detector. Depending on the observing modes required by the programs, the time cadence can go up to 10 s.

HRI_{EUV} (Halain et al. 2015): The HRI_{EUV} is an off-axis Cassegrain telescope, which has a two-mirror optical design. It has a FOV of 1000'' × 1000'' focusing on localized, smaller-scale events and a periodic Al/Mo/SiC multi-layer coating centered at 17.4 nm (Fe IX-X) to look into coronal phenomena. A filter wheel is also used. Instead of switching wavelengths as for FSI, it provides redundancy to the focal filter and does also protect the detector with a blocking position. The "high-resolution" aspect of HRI_{EUV} is one of its major strengths. It has a pixel size of 0.492'', which corresponds to a resolution over two pixels of about 200 km when Solar Orbiter is at closest perihelia. HRI_{EUV} can operate at high imaging cadence of less than one second.

HRI_{LYa} (Schühle et al. 2011): The HRI_{LYa} channel is an off-axis Gregory telescope. Similar to the optical design of the HRI_{EUV}, it has two mirrors, which apply Al/MgF₂ coatings to efficiently reflect the 121.6 nm light. One entrance filter and one focal filter are used for avoiding the contamination of visible, infrared, EUV and X-ray light. It has the same FOV of 1000'' × 1000'' and similar plate scale and temporal resolution as HRI_{EUV}.

2.1.2 SPICE: The Spectral Imaging of the Coronal Environment

The SPICE instrument is a high-resolution imaging spectrometer covering a variety of EUV spectral lines, ranging from 70.4 nm to 79.0 nm and from 97.3 nm to 104.9 nm. As each line has a certain formation temperature, these lines are found to be emitted between the top of the chromosphere and the low corona, with a temperature from 10000 K to 2 MK. Two iron lines among them are selected for flaring plasma with a higher temperature of about 10 MK. A summary of the SPICE spectral lines can be found in Table 2.2, which shows, for each line, the emitting ion, the wavelength and the formation temperature, together with an indication of the intensity of the signal they produce (intensity as photon numbers per pixel per second detected by SPICE) for both active regions and quiet sun (Curdt et al. 2001, 2004). The entire detector can be read out or just selected spectral bands can be read out. In addition, it can be decided whether to retrieve the full spectral profile or to only return the intensity integrated along the wavelength onboard. These spectral profiles provide more detailed information on the plasma state than broad band imagers. In fact, from retrieving the intensity, the position and the width of these profiles, it is possible to obtain information about temperature, density, line of sight (LOS) velocity, unresolved thermal and non-thermal velocity and elemental composition.

The optical design of SPICE can be found in Fludra et al. (2013). It consists of a single-mirror telescope, a spectrometer entrance slit and a diffraction grating. The image passing through the slit is diffracted and finally captured on two separate detectors, one for the short wavelength band (SW: 70.4–79.0 nm) and another for the long wavelength band (LW: 97.3–104.9 nm). A schematic showing the SPICE FOV with the size of the detectors and slits can be found as Figure 2.2. Each APS detector has 1024×1024 pixels, spatially (along Y axis) longer than the slit size (~ 800 pixels including the square alignment apertures, the so-called dumbbells at both ends). Since the slit length is about $14'$ including the dumbbells (the part without is about $11'$ long), the pixel size along the slit is about $1'' \text{ pix}^{-1}$. Along the wavelength, each window is about 9 nm wide in total, giving a spectral dispersion of about $0.009 \text{ nm pix}^{-1}$. SPICE has two types

Table 2.2: Characteristics of main spectral lines observed by SPICE, taken from SPICE Consortium et al. (2020); reproduced with permission ©ESO.

Ion	$\lambda[\text{\AA}]$	$\log T[\text{K}]$	Intensity* [$\text{ph pix}^{-1} \text{s}^{-1}$]	
			AR	QS
H I	1025.72	4.0	883.5	372.2
C II	1036.34	4.3	17.6	21.1
C III	977.03	4.5	563.7	312.1
S V	786.47	5.2	31.6	3.4
O IV	787.72	5.2	56.1	6.0
O V	760.43	5.4	59.5	1.9
O VI	1031.93	5.5	8268.2	139.0
O VI	1037.64	5.5	2951.3	66.19
Ne VI	1005.79	5.6	15.4	0.3
Si VII	1049.25	5.6	7.5	–
Ne VIII	770.42	5.8	63.9	7.8
Mg VIII	772.31	5.9	9.2	–
Mg IX	706.02	6.0	3.0	0.9
Fe X	1028.04	6.0	10.1	4.7
Mg XI	997.44	6.2	1.7	0.6
Si XII	520.67	6.3	31.2	2.5
Fe XVIII	974.84	6.9	6.9	–
Fe XX	721.55	7.0	1428.2	–

*Intensity refers to the number of photons detected by SPICE for both active regions and quiet sun. The solar flux applied for simulating detected intensity is from Curdt et al. (2001) and Curdt et al. (2004). Fe XX intensity was measured in a M7.6 flare.

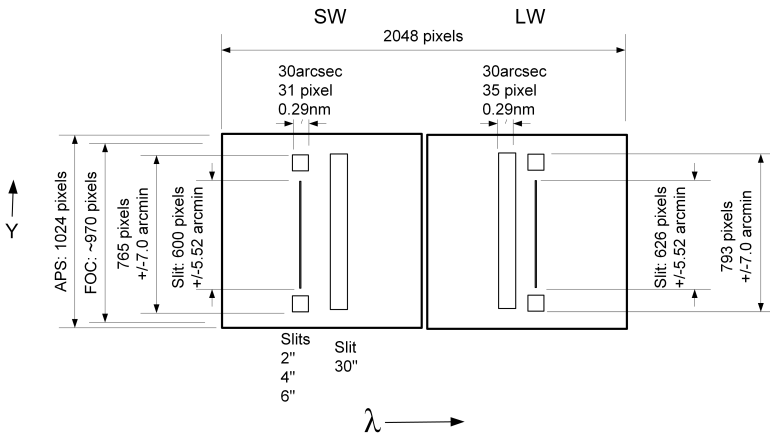


Figure 2.2: SPICE FOV diagram. Image credit: SPICE Consortium et al. (2020), reproduced with permission © ESO.

of slits, i.e., the narrow slits with width of 2'', 4'' and 6'' and the wide slit, or slot, being 30'' wide. The slot is 14' long as it does not have dumbbells at each end.

SPICE data are arranged into a four dimensions array, as (X, Y, wavelength, time). One or more of these dimensions could be singular depending on the observation mode. For example, a whole region scanning can cover a large region on the solar surface, but has to sacrifice the temporal resolution. A sit-and-stare observation have a high time cadence, which can go up to a few seconds. But since the slit position on the Sun is fixed, it can only capture a region as narrow as the slit width. The exposure time and number of scanning steps can be adjusted to meet the specific requirements of a research project, optimizing the balance between temporal resolution, data coverage, and signal level.

2.1.3 SO/PHI: The Polarimetric and Helioseismic Imager

The SO/PHI instrument is designed to measure the magnetic field of the Sun's photosphere. It plays a crucial role in understanding the Sun's magnetic field

evolution, its influence on solar activity, and its impact on space weather. As the first polarimeter that measures the field of the Sun from outside of the Earth-Sun direction, SO/PHI also provides an unique opportunity to combine with other telescopes in Earth's orbit (e.g., HMI) or on the ground (e.g., DKIST) for stereoscopic observations.

SO/PHI functions as an imager, mapping the continuum intensity, which is regarded as emitted from the photosphere. In each pixel, SO/PHI samples the Fe I line (6173Å) for the Doppler velocity and the polarization state (four Stokes parameters). The Stokes parameters are afterwards used for retrieving the vector magnetic field, in the form of (B, γ, ϕ) , where B is the magnetic field strength, γ and ϕ are the inclination and azimuth of the magnetic field, representing the field direction. The Fe I line profile is sampled at 6 wavelengths and because of the unique trajectory of Solar Orbiter, its speed towards or away from the Sun can shift the line. Thus, a LiNbO_3 tunable Fabry-Perot etalon is applied to compensate with the speed. All images are recorded on a $2k \times 2k$ CMOS detector.

SO/PHI is composed of two telescopes with different FOV: the Full Disc Telescope (FDT) with a large FOV covering the whole Sun disk and the High Resolution Telescope (HRT) with an angular resolution (2 pixels) of about $1'' \text{ pix}^{-1}$. The FDT has a FOV of 2° with an angular plate scale of $3.75''$. The HRT has a FOV of $0.28^\circ \times 0.28^\circ$ and an angular plate scale of $0.5''$. It is pointed into the same direction as HRI to observe the photosphere while HRI observes the overlying chromospheric and coronal structures at the same time to build connections between them.

2.2 Data diagnostics Methods

2.2.1 Differential Emission Measure

The Differential Emission Measure (DEM) method is a diagnostic tool for understanding the thermal structure of optically thin plasma. Based on observed emissions, it can provide information about how the plasma is distributed across temperatures. The emission measure (EM) is, by definition, a total measure

of emission integrated over a volume of plasma and based on this, the DEM is a temperature dependent function that describe the EM in a certain (small) temperature range (Phillips et al. 2008), which can be expressed as:

$$DEM(T) = \frac{d(EM)}{dT} \quad (2.1)$$

In the low corona and transition region, EUV/FUV emission lines are generally the result of electron collisional excitation followed by spontaneous de-excitation while at greater heights (lower densities) radiative excitation becomes also important. In both cases, due to its low density, the coronal plasma is generally considered to be optically thin and all emitted photons can travel outwards to reach the observer (there are exceptions for the case of very strong lines like H I Lyman- α 121.6 nm and C III 97.7 nm at low heights). Thus, the intensity of the emission from a k-times ionized element X from a transition from level j to level i can be written as:

$$I_{ji} = \int_{los} \frac{h\nu_{ji}}{4\pi} A_{ji} n_{X,j}^{+k} dl \quad (2.2)$$

where $n_{X,j}^{+k}$ is the number density of k-times ionised atoms of the element X which are excited to the upper level j , h is Planck's constant, $\nu_{ji} = hc/\lambda_{ji}$ is the frequency of the emission and A_{ji} is the Einstein coefficient, describing the probability per unit time that the ion in the excited state j will spontaneously decay to state i . The intensity is a result of the emission from each volume element along the LOS being integrated together.

$n_{X,j}^{+k}$ is hard to measure directly, but can be written as:

$$n_{X,j}^{+k} = \frac{n_{X,j}^{+k}}{n_X^{+k}} \frac{n_X^{+k}}{n_X} \frac{n_X}{n_H} \frac{n_H}{n_e} n_e \quad (2.3)$$

where, n_H and n_e are the number densities of hydrogen and electrons, respectively. $n_{X,j}^{+k}/n_X^{+k}$ is the excited fraction of the ion X^{+k} to the level j , n_X^{+k}/n_X is the k-times ionization fraction of the element X and n_X/n_H is the relative element abundance of X ($A_X = n_X/n_H$) with respect to hydrogen. Under the assumption of ionization equilibrium, meaning that ionization and recombina-

tion processes have reached a steady state for each ion at a given temperature, all these atomic data are provided by atomic databases such as the CHIANTI database (Dere et al. 1997; Landi et al. 2013). This assumption is usually justifiable for static or quasi-static plasma, but can break when rapid changes happen.

The contribution function G_{ji} , which considers the excitation and de-excitation process that contribute to the formation of a line, is then defined as:

$$G_{ji} = A_{ji} \frac{h\nu_{ji}}{4\pi} \frac{n_{X,j}^{+k}}{n_X^{+k}} \frac{n_X^{+k}}{n_X} A_X \frac{1}{n_e} \quad (2.4)$$

Putting together Equations 2.2 to 2.4, the emission intensity can be re-described in the form of:

$$I_{ji} = \int_{los} G_{ji} n_H n_e dl \quad (2.5)$$

In general G_{ji} is a function of the electron temperature T_e and of n_e . In the case of allowed transitions, assuming the balance between collisional excitation from the ground state g and spontaneous decay from an excited state j , and that the major ion population is in the ground state, it can be demonstrated as:

$$\frac{n_{X,j}^{+k}}{n_X^{+k}} = n_e \frac{C_{gj}}{A_{jg}} \quad (2.6)$$

where C_{gj} is the coefficient for collisional excitation from the ground state g to the excited state j and A_{jg} is the Einstein coefficient from j to g . Combining Equations 2.4 and 2.6, and considering that the ionization fraction n_X^{+k}/n_X is predominantly a function of temperature, the contribution function is essentially only dependent on temperature and peaks at a certain temperature, which is the so-called formation temperature of the line having that G_{ji} . Moreover, considering that $n_H \sim 0.85n_e$ in a fully ionized coronal environment, Equation 2.5 becomes:

$$I = 0.85 \int_{los} G(T) n_e^2 dl \quad (2.7)$$

Meanwhile, the EM over a unit area in an optically-thin environment can be written as:

$$EM = \int_{los} n_H n_e dl = \int n_H n_e \frac{dl}{dT} dT \quad (2.8)$$

which, when there is an unique relation between electron density and temperature

(e.g., a constant pressure plasma), can be combined with Equation 2.1 to give:

$$DEM(T) = n_H n_e \frac{dl}{dT} \quad (2.9)$$

The physical meaning of DEM can be understood as the LOS sum of n_e^2 within the temperature bin $[T, T+dT]$. Putting Equation 2.7 and Equation 2.9 together, the emission intensity can again be expressed as:

$$I = \int_T^{T+dT} DEM(T)G(T)dT \quad (2.10)$$

This implies that, in principle, from the intensities I measured from the observation of several allowed lines covering a wide temperature range and the contribution functions $G(T)$ of these lines calculated from an atomic database, the $DEM(T)$ can be obtained as a result of an inversion problem.

In the case of DEM analysis of observations from wide-band instruments (e.g., EUV and AIA), the contribution function is replaced with the channel response function $K(T)$, which also considers the sensitivity of a detector or instrument channel to the line emissions contributing to the signal recorded by the instrument, as a function of wavelength $R(\lambda)$. The response function can be written as:

$$K(T) = \int_0^\infty G(\lambda, T)R(\lambda)d\lambda \quad (2.11)$$

where $G(\lambda, T)$ involves the atomic process of all the plasma emitting at a certain temperature range while $R(\lambda)$ is the instrument-wavelength response (Boerner et al. 2012).

Practically, there are three different methods to retrieve a DEM, i.e., Gaussian DEM (Warren and Brooks 2009), linear or multi-linear DEM (Young 2005a,b, 2018) and Markov-Chain-Monte-Carlo (MCMC; Kashyap and Drake 1998) DEM. The first two assume the shape of the DEM to be in a Gaussian or multi-linear form while MCMC DEM does not require a certain functional form of DEM but repeatedly compare models to data for the best fitting.

2.2.2 Magnetic field extrapolation

As mentioned in Section 1.4, the direct measurement of magnetic fields becomes increasingly difficult when moving up from the photosphere into the chromosphere and corona. Therefore, magnetic field extrapolation is a compensative technique to calculate the coronal fields from the measurements made at the solar surface.

The corona is a plasma $\beta \ll 1$ region due to its low density. This means that the magnetic pressure is much greater than the gas pressure so the magnetic field tends to arrange itself in a stable configuration that minimizes magnetic energy. This gives us the force-free assumption where the Lorentz force vanishes. It generally seems to work well in the corona. The extrapolated magnetic fields have been shown to compare well with coronal structures in observations, either with 2-dimensional imaging observations (e.g., Régnier et al. 2002; Régnier and Amari 2004; Schrijver et al. 2008) or with 3-dimensional loops reconstructed from stereoscopic observations (e.g., Feng et al. 2007). Deriving from Maxwell's equations and considering the case of perfect conductivity, a static force-free magnetic configuration can be expressed as:

$$\mathbf{j} \times \mathbf{B} = 0 \quad (2.12)$$

$$\nabla \times \mathbf{B} = \mu_0 \mathbf{j} \quad (2.13)$$

$$\nabla \cdot \mathbf{B} = 0 \quad (2.14)$$

where \mathbf{B} is the magnetic field, \mathbf{j} is the electric current density and μ_0 is the vacuum permeability. From Equation 2.12 and 2.13 one can have:

$$\mathbf{j} = \frac{1}{\mu_0} \alpha \mathbf{B} \quad (2.15)$$

where α is called the force-free parameter. When $\alpha = 0$, the force-free field is in its minimum energy state without electric currents, also known as a potential field. When α is a constant number everywhere in the volume, it is a linear force-free field and otherwise, a nonlinear force-free field when α is variable.

An extrapolation can be done globally or locally. For example, the potential-field source-surface (PFSS) model is a global potential extrapolation usually

assuming a source surface, which is usually at about $2.5 R_{\odot}$ where the magnetic fields either close back to the solar surface below or extend outwards radially (e.g., Schatten et al. 1969; Wang and Sheeley 1992; Riley et al. 2006). A synoptic map of the (measured) magnetic field data at the solar surface is used as a bottom boundary. Only the radial photospheric magnetic field is required for the potential field extrapolation.

Although a potential field extrapolation is mathematically simple and it is fast to compute the magnetic structure of a relatively quiet region or to provide the large-scale connection between the solar atmosphere and the heliosphere (global magnetic field modeling), it is not satisfactory for modeling active regions precisely because it assumes the free energy in the modeling volume is zero. A comparison between global potential field and observations indicates the difficulty in modeling coronal loops (Schrijver et al. 2005; Sandman et al. 2009).

For a non-potential force-free field, α can be calculated as:

$$\alpha(x, y) = \mu_0 \frac{j_{z0}}{B_{z0}} \quad (2.16)$$

where j_{z0} and B_{z0} are the vertical components of the electric current and magnetic field at the surface ($z = 0$). j_{z0} can be expressed as:

$$j_{z0} = \frac{1}{\mu_0} \left(\frac{\partial B_{y0}}{\partial x} - \frac{\partial B_{z0}}{\partial y} \right) \quad (2.17)$$

In a linear force-free field, α is constant and thus can be estimated as the average of $\alpha(x, y)$ over the whole region. An alternative way is to compute models with different α and compare the magnetic field lines with the corresponding emission observations to figure out the best fit (e.g., Carcedo et al. 2003; Wiegelmann and Sakurai 2021).

A non-linear force-free field contains more details of the magnetic field and is also closer to the real configuration. However, it relies heavily on high-quality vector magnetogram data, which encounters the azimuthal 180° ambiguity problem. The transverse component of the magnetic field vector has a directional angle, called the azimuth. The measurements of magnetic field derived based on the Zeeman effect does not uniquely determine the azimuthal direction, i.e., if the azimuthal angle is measured as θ , both θ and $\theta + 180^\circ$ are possible solutions.

Thus, careful disambiguation, e.g., minimizing the total magnetic energy should be applied before the data is used for extrapolation.

A force-free field can be a good assumption in the corona, but not always in the photosphere ($\beta \gg 1$) and the chromosphere ($\beta \approx 1$). In the lower layers of the Sun, the Lorentz force remains finite and needs to be compensated by plasma forces like the plasma pressure gradient and gravity force.

This is taken into consideration in a magneto-hydro-static (MHS) model, which assumes no plasma flows and the forces are temporally independent. This is a valid assumption when the inertial term ($\rho d\mathbf{v}/dt$) is much smaller than the Lorentz force, i.e., when the plasma flow velocity is much lower than the Alfvén speed. In regions with slow plasma flows, such as in the photosphere (flow velocity is in the order of $1\text{--}2 \text{ km s}^{-1}$), the dynamic effects are negligible. Therefore, Equation 2.12 becomes:

$$\mathbf{j} \times \mathbf{B} = \nabla p + \rho \nabla \Psi \quad (2.18)$$

where p is the plasma pressure, ρ is the mass density, and Ψ is the gravitational potential. Same as the non-potential force-free models, a linear MHS model requires thorough estimation of α , which usually depends on the comparison with the observed emission and a non-linear MHS needs the accurate measurement of the magnetic field vector.

2.2.3 Error estimation

In any measurement or observation, there are potential sources of error that can impact the accuracy and precision of the results. Understanding these sources and making error estimation is crucial for data analysis and for improving the reliability of the results. In this thesis, the uncertainty of the observed intensity is estimated by considering the photon noise, the readout noise and the dark current, with one or more of them maybe bring negligible for specific telescopes. As each of them contribute to the total noise independently, the combination of all error aspects is then calculated by adding them up in quadrature (square root of sum of squares).

2.2.3.1 Photon noise

Photon noise is a fundamental type of noise that occurs in any light detection process, which originates from the discrete nature of the photons. The photon flux emitted by the light source is not constant but with a random fluctuation. This temporal randomness of their arrival at the detector results in a statistical variation of the number of photons that hit the detector in a certain time interval, which is the photon noise.

Photon noise is characterized by Poisson statistics as the arrival of each photon can be regarded as an independent, discrete and random event. Therefore, the uncertainty of N , the number of photons collected (intensity), is approximately \sqrt{N} . The more photons per second are emitted by the light source that reach a detector pixel, the greater the signal registered by that pixel is, and thus the larger uncertainty it has. As a result, the signal-to-noise ratio ($SNR = N/\sqrt{N} = \sqrt{N}$) improves as the square root of the signal.

Photon noise is an inherent property of the detection process and cannot be eliminated by improving detector technology. However, increasing exposure time or measuring stronger (emission) lines to collect more light can reduce its relative effect.

2.2.3.2 Readout noise

Readout noise is a type of noise inherent to electronic detectors, particularly charge-coupled devices (CCDs) and CMOS detectors. It occurs during the process of reading and digitizing the electrical signal generated by photons hitting the detector. For example, both CMOS and CCD detectors use light-sensitive components to convert light intensity (photons) into electrical signals (electrons) and this electron charge will be afterwards transferred into a voltage signal. After that, this voltage signal is amplified and the resulting analog signal is digitized into a digital value representing the light intensity. This acquisition chain is bound to introduce noise.

Different from CCDs, where the signal collected by each pixel is transferred to a common amplifier, each pixel of a CMOS has its own amplifier, which enables faster readout process and lower energy consumption, but could, at the

same time, introduce higher readout noise. Unlike photon noise, readout noise is independent of the signal itself. Thus, it can have a more noticeable impact when the signal level is low while is usually neglected in the case of strong signals.

2.2.3.3 Dark current

Dark current is the background electric current that can always be detected even when the detector is not exposed to light. It originates from thermal excitation of electrons within the sensor pixels. Also, these thermal electrons, as well as the electrons generated by photons, are collected, converted and amplified together by the detector, causing noise in the signal, the so-called dark current. It is regarded as a base level of noise and can significantly reduce the signal-to-noise ratio in a weak signal detection.

The thermal origin of the dark current makes it sensitive to the operating temperature of the sensor. During operation, the build up of thermal energy can result in more hot electrons being excited and collected. That is why cooling detectors and protecting them from the hot environment is important to improve the image quality. Another aspect that matters in estimating dark current noise level is the exposure time, as the dark current is usually given in the form of the number of electrons that build up in each pixel in each time unit. The longer the exposure is, the more thermal electrons are collected.

Chapter 3

Brightenings in the quiet sun

The content presented in this chapter builds on the publication "Imaging and spectroscopic observations of extreme-ultraviolet brightenings using EU1 and SPICE on board Solar Orbiter" on Issue Astronomy and Astrophysics, Volume 673, as Article A82 in May 2023. This work was carried out based on discussions with L. Teriaca, R. Aznar Cuadrado, L. P. Chitta, S. Mandal, H. Peter, U. Schühle, S. K. Solanki, F. Auchère, D. Berghmans, É. Buchlin, M. Carlsson, A. Fludra, T. Fredvik, A. Giunta, T. Grundy, D. Hassler, S. Parenti and F. Plaschke.

3.1 Introduction

As discussed in Section 1.7, Parker's nanoflare model is commonly accepted as an efficient way to heat up the corona to a sufficiently high temperature by small flares triggered from magnetic reconnection. It also implies that, maintaining corona temperature involves processes occurring at smaller spatial scale and shorter temporal scale. Therefore, to support this idea observationally, it is

essential to detect small-scale transients that appear frequently enough across the solar surface to provide most of the energy required to maintain the coronal temperature.

The launch of Solar Orbiter greatly advances the ability to observe small-scale solar structures, enabling detection down to finer spatial scales than previously possible. The smallest transient EUV brightenings, firstly reported by Berghmans et al. (2021), were observed by HRI_{EUV}, part of the EUI instrument (see Section 2.1.1). The data they analyzed were taken on 30 May 2020, during the commissioning phase of Solar Orbiter, which was 0.556 AU from the Sun. At this distance, HRI achieved a spatial resolution of 400 km. In the 4-min observation with 5 s cadence, 1467 brightenings were identified to conduct a throughout statistical analysis. In Berghmans et al. (2021), these brightenings are called "campfires" for public outreach. Although this name nicely expresses their brightness enhancement in the observations, it cannot show the physical nature of these structures in a scientific sense. Thus, I hereafter use the name "EUI brightenings" to refer to these small-scale EUV brightening detected in EUI observations.

The EUI brightenings are characterized by their small scale. They generally exhibit two distinct morphologies, i.e., dot-like and loop-like structures. The largest events have a projected area of a few Mm² and the loop-like brightenings extend no more than 4 Mm in length. These brightenings are also short-lived, with most lasting only a few tens of seconds, while the longest events reach the observation limit of approximately 200 s. The statistical results show that both the projected area and duration exhibit power-law distributions.

As the magnetic reconnection process plays an important role in the nanoflare heating model, studies have been conducted to search for the connection between the EUI brightenings and their magnetic structures and activities. Berghmans et al. (2021) compared the location of the EUI brightenings to imaging observation from HRI_{Ly α} and found that most of the EUI brightenings located at the boundaries of chromospheric network, where strong magnetic flux concentrates. By analyzing the underlying magnetic features with data from SO/PHI, Kahil et al. (2022) demonstrated that most EUI brightenings are associated with magnetic flux cancellation at the footpoints of small loops. However, what they

also found is that around 25% of the EUV brightenings studied lack clear signs of magnetic activity in the photosphere, suggesting that other heating mechanisms may be at work. Panesar et al. (2021) further identified connections between EUV brightenings and opposite-polarity magnetic features using data from HMI (Helioseismic and Magnetic Imager, Scherrer et al. (2012)). Using MHD simulations, Chen et al. (2021) suggested that most brightening events, which resemble the observed EUV brightenings, are primarily driven by magnetic reconnection. The link between EUV brightenings and magnetic field activities implies that these brightenings may share formation and evolution mechanisms with larger-scale events such as flares.

Another key factor in understanding whether small-scale events contribute to coronal heating is the capability of establishing their temperature. Observations from a broad band imager (e.g., AIA (Atmospheric Imaging Assembly, Lemen et al. (2012)) and EUV) carry some temperature information for that each passband usually has a dominating line formed at a certain temperature. However, the temperature information obtained based on this is not completely accurate due to that the imagers work by combining the emission from all lines in their passbands. Thus, the DEM method is usually applied to calculate the emission (in the units of $\text{cm}^{-5} \text{K}^{-1}$) integrated over the LOS in each temperature bin (Hannah and Kontar 2012; Cheung et al. 2015). DEM analysis using data from AIA has shown that the DEM-weighted temperatures for EUV brightenings and similar small EUV brightenings, peaking at $\log T[\text{K}] = 6.12$, are close to typical coronal temperatures (Chitta et al. 2021a; Berghmans et al. 2021).

Although the DEM method with broad band imaging data is effective and commonly used to determine temperature profiles of coronal structures across various scales, it does have uncertainties due to assumptions regarding the spectral response of broadband imagers. For example, Guennou et al. (2012) found that the DEM inversions of AIA data may be biased toward 1 MK in multi-thermal plasma, which may account for the 1 MK temperatures derived for EUV brightenings using this technique.

Spectrometers can provide more accuracy in temperature diagnostics for their spectral resolution. Previous studies have investigated small solar phenomena, such as bright points, small jets, and explosive events, by utilizing

spectral lines formed at different temperatures within the transition region and corona, recorded by various spectrometers. For example, Innes et al. (1997), using data from SUMER, concluded that explosive events are bidirectional jets driven by magnetic reconnection. Teriaca et al. (2004) detected mass flows within transition region small structures through the non-Gaussian profiles of the O VI (103.193 nm) line. Tian et al. (2008) explored cool and hot elements in an EUV bright point using ten spectral lines. These studies have provided valuable insights into the complex transition region and corona. Similarly, spectroscopic data are also helpful in exploring the thermal properties of EUV brightenings. In this chapter, I will discuss about the analysis of EUV brightenings with both imaging and spectral data, with the EUV (HRI_{EUV}) and the SPICE instruments simultaneously observing the same solar region in 2021 during Solar Orbiter's cruise phase.

3.2 Overview of observations

To study the temperature characteristics of EUV brightenings, I search the simultaneous observation of EUV and SPICE for brightenings identified in HRI_{EUV} FOV that are also captured by SPICE. Table 3.1 shows the overview of the data sets used in this study. Data applied here are from two sections of the spacecraft orbit, taken from 23 February 2021 and 12/13 September 2021, respectively. All times in Table 3.1 are the starting time of each observation. The EUV data analyzed are part of the EUV data release 5.0¹, and the SPICE data of the SPICE data release 3.0². The overviews of the HRI_{EUV} FOV in both data sets are displayed in Figure 3.1.

Solar Orbiter was 0.53 au away from the Sun with a separation angle from the Earth-Sun line of about 140° on 23 February 2021 when data set 1 was obtained. HRI_{EUV} observed from 17:13:25 UT to 17:20:59 UT with a time cadence of 2 s at the wavelength of 17.4 nm. The high angular image scale of HRI_{EUV} (0.492'' pixel⁻¹) corresponds to the 2-pixel resolution of about 380 km on the Sun at this heliocentric distance.

¹<https://doi.org/10.24414/2qfw-tr95>

²<https://doi.org/10.48326/idoc.medoc.spice.3.0>

Table 3.1: Overview of the observations.

Date	Instrument	Time	Cadence	Exposure	Type	Version
23-Feb-2021	HR _{EUV}	17:13:25-17:20:59	2 s	1.65 s		
		15:44:00				
	SPICE	17:33:43	N/A	20 s	Context raster	V10
12/13-Sep-2021		16:50:31-17:23:31	20 s	4.7 s	Small rasters	
		22:00:59-22:14:59	2 s			
	HR _{EUV}	23:05:00-23:19:00	1 m	1.65 s		
		00:11:51-00:24:59	2 s			
		22:04:19-23:12:09				V08
	SPICE	23:12:20-00:20:10	10.2 s	10 s	Sit and stare	V12
		00:20:20-01:28:10				V05

Around this time, SPICE observed in both context raster and high-cadence small rasters modes. The two context raster observations started from 15:44:00 UT (opening context raster) and 17:33:43 UT (closing context raster), respectively. Each context raster was a 192-step scanning over a wide range on the Sun in $4''$ steps, with a $4''$ (about 1500 km on the Sun) slit and a 20 s exposure time at each position. Between the two context rasters, small rasters with only 3-step scanning were obtained from 16:50:31 UT and 17:23:31 UT every 20 s with a 4.7 s exposure time. The slit width was also $4''$ and for every step the slit repositioned also by $4''$. Along the SPICE slit, the image scale is $1.098'' \text{ pixel}^{-1}$ (about $420 \text{ km pixel}^{-1}$).

On 12 and 13 September 2021, when Solar Orbiter had a heliocentric distance of 0.59 AU and an angular separation from the Sun-Earth line of about 50° , HRI_{EUV} obtained three sets of image sequences, but only observations from 16:50:31 UT to 17:23:31 UT and from 00:11:51 UT to 00:24:59 UT have a high time cadence of 2 s. The other sequence (23:05:00-23:19:00 UT) has a 1 min time cadence, which is not suitable for detecting short-lived and dynamic brightenings. The exposure time of all observation periods is 1.65 s and the spatial resolution of HRI_{EUV} images is about 420 km. At about this time, SPICE provided sit-and-stare observations in three time spans, during which the position of the $4''$ slit was fixed on the Sun. The pixel size along the SPICE slit is about 470 km on the Sun in this data set and the time cadence is 10.2 s with an exposure time of 2 s.

In this work, all the data used are level 2 with the instrumental effects corrected. For HRI_{EUV}, the level 2 data are returned in digital number per second (DN s^{-1}) while the unit of the SPICE level 2 data is $\text{W m}^{-2} \text{ sr}^{-1} \text{ nm}^{-1}$. As the SPICE slit can only cover a narrow region, only three EUV brightenings are found to be captured by both HRI_{EUV} and SPICE in these data sets. Their positions are marked in Figure 3.1 and for convenience, they are called E-1, E-2 and E-3 hereafter. These EUV brightenings are characterized by their small scale and short duration. All of them are smaller than 5 Mm^2 at the limit of the SPICE observation capabilities. E-1, the shortest-lived EUV brightenings was only observed for about 40 s while the others existed longer than minutes. The characteristics of all events are summarized in Table 3.2.

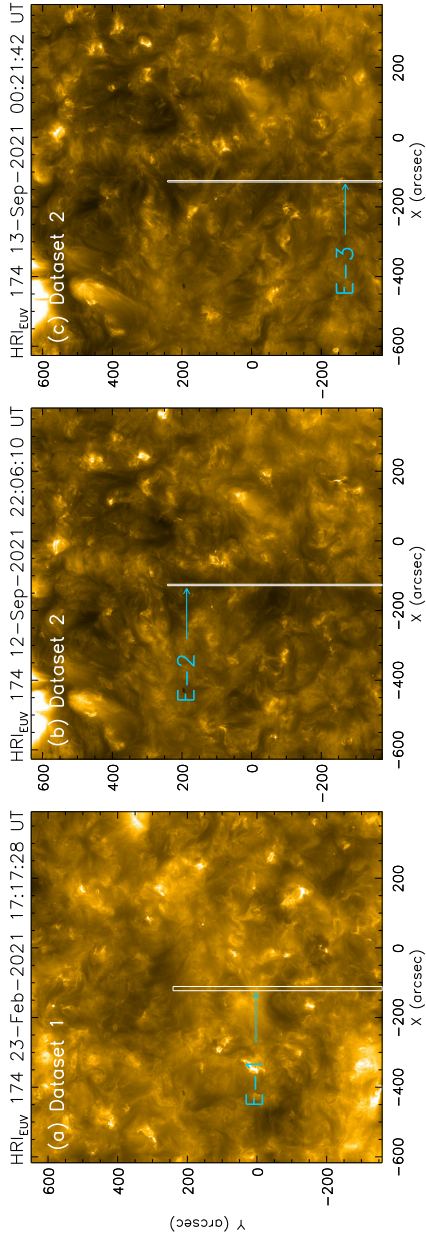


Figure 3.1: Images of the HR_{EUV} FOV from both data sets. (a) shows the observation taken on 23 February 2021 at 17:17:28 UT in data set 1 while (b) and (c) are the images obtained on 12 September 2021 at 22:06:10 UT and 13 September 2021 at 00:21:42 UT, respectively. Both (b) and (c) come from data set 2. The white box in each image indicates the region that is also covered by the SPICE slit, which is wider in data set 1 (3-step raster) and narrower in data set 2 (sit-and-stare). The blue arrows point the EUV brightenings as a guide to the eye.

Table 3.2: Event characteristics

Event	Start time	Peak time	Duration	Area (Mm ²)
E-1	17:17:04	17:17:28	50 s	2.2
E-2	22:04:24	22:06:10	6 m	3.8
E-3	00:20:16	00:21:40	4 m	4.5

Event	SPICE spectral lines
E-1	Mg IX, Ne VIII, C III, Ly β , O VI
E-2	N IV, Ne VIII, S V, O IV (78.7 nm, 79 nm), C III,
E-3	Ly β , O VI

3.3 Data preparation and analysis

3.3.1 Data preparation and Gaussian fit

The available spectral lines recorded by SPICE in each data set are shown in Table 3.2. In data set 1 (E-1), SPICE provides Mg IX 70.602 nm ($\log T[/K] = 6.0$) and Ne VIII 77.042 nm ($\log T[/K] = 5.8$) and cooler transition region lines such as C III 97.703 nm ($\log T[/K] = 4.8$), Ly β 102.572 nm ($\log T[/K] = 4.0$), and O VI 103.193 nm ($\log T[/K] = 5.5$). Mg IX has a too low SNR to be analyzed in this case. For data set 2 (E-2 and E-3), more lines such as N IV 76.515 nm ($\log T[/K] = 5.1$), S V 78.647 nm ($\log T[/K] = 5.2$), O IV 78.772 nm ($\log T[/K] = 5.2$), and O IV 79.019 nm ($\log T[/K] = 5.2$) are provided by the SW detector in addition to Ne VIII. Dominated by the instrumental profile, SPICE spectra can be reasonably fitted to a Gaussian function, which is applied for retrieving the integrated line radiance. Before this fitting, a preparation is conducted to the original data to deal with the effect of spike pixels, which are, to be specific, the pixels with high positive value caused by cosmic rays during the observation and the pixels with high negative value mostly due to cosmic rays hitting the detector when the single dark field used for correction was taken. All lines can be fitted well to a single Gaussian function, apart from the S V line at 78.647 nm and the two O IV (78.772 nm and 79.019 nm) lines,

which are blended together at the spectral resolution of SPICE. Therefore, these lines are fitted together with a triple Gaussian function. The O IV 79.019 nm line is excluded from further study in this work due to its position near the edge of the detector, which reduces its reliability. Hereafter in this chapter, all O IV line mentioned refers to the O IV 78.772 nm line.

A custom software based on the `xcfit_block.pro` routine from Solarsoft is used for the gaussian fit process. This software processes the prepared data and corresponding estimated errors (see Section 3.3.2) to derive the parameters of the Gaussian function(s), including amplitude, line center, line width and the background at each point. The background is assumed to remain constant across the wavelength range of each spectral line window. To enhance the SNR, the data are binned over 4 spatial pixels along the slit direction. Given that the slit width is 4'', roughly four times the imaging spatial scale, this binning produces square pixels in the resulting raster scans. Additionally, the SPICE spatial resolution, estimated at approximately 6–7'', ensures that this binning does not significantly degrade the information on the target EUV brightenings. Hereafter in this chapter, all references to SPICE data correspond to this 4-pixel binning along the slit, resulting in an effective plate scale of 4'' × 4.392'' (hereafter one SPICE-binned pixel), approximately 1540 × 1690 km for event E-1 and 1710 × 1880 km for events E-2 and E-3. From the fitting results, I determine the radiance for each pixel after binning.

3.3.2 Error estimation of SPICE data

The errors in the SPICE data are essential in the Gaussian fitting process, as they directly influence the uncertainties of the fitted parameters. An average signal \bar{I}_{DN} is defined as the DN accumulated per detector pixel and averaged over the exposure time. Then, the uncertainty (in photons) arising from photon noise across a total of n_p pixels with average signal \bar{I}_{DN} can be written as:

$$\sigma_{ph} = \sqrt{F^2 \bar{I}_{DN} n_p / G} \quad (3.1)$$

where G (DN photons⁻¹) represents the camera conversion gain and F , the intensifier noise factor, accounts for the amplification effect of the intensifier.

It is suggested that F commonly has a value between 1.3 and 2 (Denvir and Conroy 2003) and for the data used in this study, F is considered to also cover some of the uncertainties in determining G . Based on this, the uncertainty (in DN) due to the same photon noise of the signal $\bar{I}_{DN}n_p$ can be expressed as:

$$\sigma_{DN} = \sigma_{ph}G = \sqrt{F^2\bar{I}_{DN}n_pG} \quad (3.2)$$

To get the total uncertainty, one should also consider the readout noise σ_{read} , which is square root summed when several pixels are binned together, and the dark noise $n_p I_{dark}$ (in units of DN s^{-1}), which is the square root of the dark current I_{dark} over n_p pixels. By square-summing the uncertainties caused by photon noise, readout noise and dark noise together, the total uncertainties (in DN) can be written as:

$$\Sigma_{DN} = \sqrt{F^2\bar{I}_{DN}n_pG + n_p\sigma_{read}^2 + n_p I_{dark}t} \quad (3.3)$$

Practically, the SPICE data are returned after the on-board binning in DN summed over several binned pixels $I_{DN} = \bar{I}_{DN}n_p$ and its uncertainty is:

$$\Sigma_{DN} = \sqrt{F^2 I_{DN}G + n_p\sigma_{read}^2 + n_p I_{dark}t} \quad (3.4)$$

In Table 3.3, the required parameters for error estimation with Equation 3.4 are listed. Among them, G , σ_{read} and I_{dark} have been estimated through both the on-ground and in-flight calibration activities conducted by the SPICE team. To determine the intensifier noise factor and validate this method, a test is done with the uncalibrated L1 full detector observation obtained on 21 December 2021 at 15:08:34 UT, which used the 30'' wide slot. The correction is performed by subtracting a corresponding dark field taken on 15 December 2021 at 08:32:20 UT and dividing it by the flat-field matrix. These test data can be found in SPICE data release 2.0³. Besides, the cosmic spikes and hot pixels are removed, which affected about 2000 and 1000 pixels in SW and LW images, respectively. This number is very small compared with the total number of pixels in the 1024×1024 image, leaving only a negligible effect.

³<https://doi.org/10.48326/idoc.medoc.spice.2.0>

3.3. DATA PREPARATION AND ANALYSIS

Table 3.3: Error estimate parameters

	F	G (DN/phot)	σ_{read} (DN)	I_{dark} (DN/s)
SW	1	3.58	6.9	0.89
LW	1.6	0.57	6.9	0.54

Considering that the effective spatial resolution of SPICE is about 6 to 7 pixels and the wide slot observation introduces additional blurring in the spectral direction, the noise level corresponding to the average signal within a 3×3 pixel area of such an image can be approximated by calculating the standard deviation across the same 3×3 pixel region. Before getting the standard deviation, a smoothed version of the same image (created by passing through a 7×7 boxcar filter twice) is subtracted from the original image to minimize the impact of the intensity gradient on the results. But the corresponding signal value is still derived from the original image. This process is applied to every pixel in the data arrays.

Figures 3.2 (SW channel) and 3.3 (LW channel) present scatter plots of the standard deviation against the signal. The thick orange line indicates the median within bins of 10 DN, while the black line represents the theoretical predictions from Equation 3.4. Additionally, the blue histogram illustrates the data point density across bins of 10 DN. The median values match well with theoretical predictions for the majority of the intensity range when using reasonable values of F , which is $F = 1$ for SW data and $F = 1.6$ for LW data.

For calibrated L2 data, uncertainties can be computed directly using the header keyword RADCAL. This keyword provides the inverse average calibration factor, α , over the relevant spectral window, in units of $[\text{DN}/(\text{W}/\text{m}^2/\text{sr}/\text{nm})]$. This factor enables the total DN in a pixel (or in the original group of pixels for data binned on board, already adjusted by the onboard binning factor n_p) to be retrieved, as given by the relation $I_{DN} = \alpha I_{cal}$. Therefore, the uncertainty of the calibrated signal I_{cal} can be expressed as:

$$\Sigma_{cal} = I_{cal} \frac{\Sigma_{DN}}{I_{DN}} = \frac{\Sigma_{DN}}{\alpha} = \frac{1}{\alpha} \sqrt{F^2 \alpha I_{cal} G + n_p \sigma_{read}^2 + n_p I_{dark} t} \quad (3.5)$$

where the parameter n_p is specified by the keyword NBIN in the FITS header.

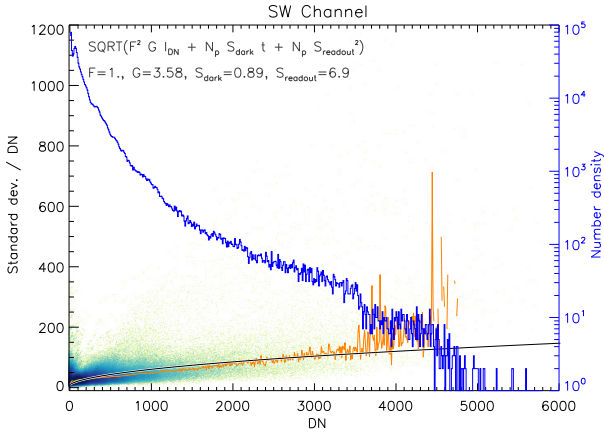


Figure 3.2: Noise estimation for uncalibrated SW data. The 2-dimensional histogram illustrates how the standard deviation varies with the signal across the image. The orange line depicts the median calculated within 10 DN bins, while the black line shows the prediction from Equation 3.4 assuming $F=1$. The blue histogram indicates the density of the data points.

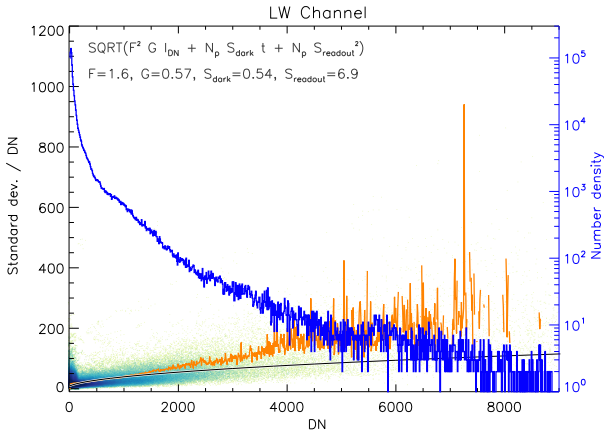


Figure 3.3: As in Figure 3.2, but for the uncalibrated LW data. The theoretical outcome (black) is fit by $F=1.6$.

The equation can be extended to account for cases where additional binning by a factor n_u (a total of n_u pixels binned together by the users) is applied by averaging the L2 calibrated data, regardless of whether onboard binning has already occurred. When user-defined binning is performed, the relationship becomes $I_{DN} = \alpha I_{cal} n_u$. For uncertainty calculations, the goal is to determine the total number of counts, I_{DN} , within the binned area. That gives the full expression of the uncertainty of I_{cal} :

$$\Sigma_{cal}(\lambda) = \frac{1}{\alpha(\lambda)} \sqrt{\frac{F^2 \alpha(\lambda) I_{cal} G}{n_u} + \frac{n_p \sigma_{read}^2}{n_u} + \frac{n_p I_{dark} t}{n_u}} \quad (3.6)$$

which also considers the wavelength-dependent calibration factor $\alpha(\lambda)$. The complete inverse calibration curve as a function of wavelength (referred to as RADCAL) is included in the FITS headers, stored as binary tables for the various windows. The wavelength-dependent calibration factor is particularly relevant for estimating errors in the case of large spectral windows and of full detector spectra, especially for the SW detector.

3.3.3 Data alignment: searching SPICE data for EUJ brightening signatures

Unlike large-scale, long-lived features that are easily identified in HRI_{EUJ} images and SPICE spectral scans, EUJ brightenings are challenging to detect in SPICE scanning data without referencing HRI_{EUJ} observations. To investigate EUJ brightening signatures in SPICE data, precise alignment of the data from both instruments is essential.

The alignment process involves a two-step method utilizing time-series data. The header information in the data files provides only rough alignment details for HRI_{EUJ} and SPICE. This limitation arises primarily because the two instruments are mounted on separate spacecraft panels and are subject to different thermal effects due to the highly elliptical orbit. Additionally, a scanning spectrometer poses its own challenges. Unlike a snapshot from an imager, a spectroscopic image constructed over an extended scanning period that can exceed one hour is significantly impacted by solar rotation. Although solar rotation effects can

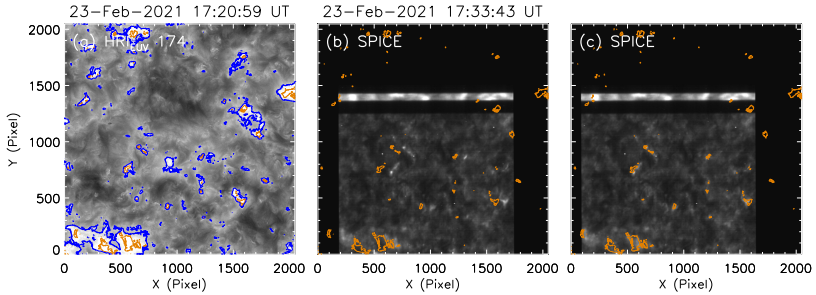


Figure 3.4: First step of data alignment. (a) HRI_{EUV} image from 23 February 2021 at 17:20:59 UT, overlaid with intensity contours at 1500 DN s⁻¹ (blue) and 2000 DN s⁻¹ (orange); (b) Intensity map of Ne VIII line radiance from the SPICE context raster, starting at 17:33:43 UT, reprojected onto the HRI_{EUV} FOV using WCS keywords from the file headers. The same 2000 DN s⁻¹ contours as in panel (a) are overplotted for reference; (c) Same as panel (b), but with the SPICE intensity map manually coarse-aligned to the HRI_{EUV} image.

be calculated and corrected, the issue remains that context rasters (those with sufficiently large FOV for meaningful correlation analysis) are captured at different times from the sit-and-stare or fast three-step rasters used in this study. To address these challenges, I implement a two-step approach to directly align the SPICE sit-and-stare (or high-cadence three-step rasters) data with the HRI_{EUV} images. Here, the 23 February 2021 data set is used as an example to explain this alignment method.

The first step involves visually refining the alignment between the SPICE context raster (reprojected onto the HRI_{EUV} data, as described below) and the HRI_{EUV} image. This refinement ignores solar rotation, aiming only to achieve a sufficiently close alignment for the next step. Figure 3.4 illustrates this process. Panel (a) displays the last HRI_{EUV} image from the 23 February data set (captured at 17:20:59 UT), overlaid with intensity isocontours of 1500 and 2000 DN s⁻¹ to outline the brightenings. Panel (b) shows the SPICE context raster image, beginning at 17:33:43 UT, reprojected onto the HRI_{EUV} data using the world

coordinate system (WCS⁴) information from the L2 FITS header. The same 2000 DN s⁻¹ isocontours as in panel (a) are overlaid on the Ne VIII context raster. Panel (c) presents the same raster as in panel (b), now adjusted for visual refinement (the first coarse alignment step). The residual misalignment caused by solar rotation is evident as a compression in the scanning direction, resulting from the FOV's rotation in the same direction as the slit scanning.

The second alignment step utilizes time-series data. For the 23 February 2021 observations, there are three time series corresponding to the three raster positions. This step involves aligning HRI_{EUUV} and SPICE data by comparing time-slice images. Within the overlapping time period of HRI_{EUUV} and SPICE high-cadence observations, the Ne VIII spectra, which have a temperature sensitivity closest to the HRI_{EUUV} bandpass for the average corona are analyzed. Each spectrum is fitted with a single-Gaussian function, and the returned line amplitudes are used to create a time-slice plot.

To generate a time-slice image of HRI_{EUUV} data that matches the timing and spatial scale of the SPICE data, the HRI_{EUUV} images nearest in time to each SPICE spectra are selected and rescaled to the SPICE spatial scale (4'' × 4.392'' after spatial binning along the slit) by averaging neighboring pixels. Figure 3.5 illustrates this process with the example that contains event E-1. Panel (a) shows an HRI_{EUUV} image reprojected onto the SPICE context raster. Panels (b) and (c) present time-slice images of HRI_{EUUV} data at full resolution and degraded resolution (to match SPICE observations), respectively. The location of the slice is selected based on the preliminary alignment from the first step. Panel (d) displays the time-slice image derived from the Ne VIII amplitude.

The orange box in panel (a) highlights the area where the correlation between HRI_{EUUV} and SPICE time-slice images is examined, that is, it covers all the possible locations of the SPICE slit. For each of the time-slice plots within this region, the correlation coefficient is calculated and the location of maximum correlation is then identified. For the 23 February data set, this procedure is repeated for each of the three raster positions. Figure 3.6 panels (a), (b), and (c) show correlation coefficient maps for all three raster positions, obtained by shifting the alignment position over a grid of 21 × 31 HRI_{EUUV} full-resolution pixels. Panel (d)

⁴https://fits.gsfc.nasa.gov/fits_wcs.html

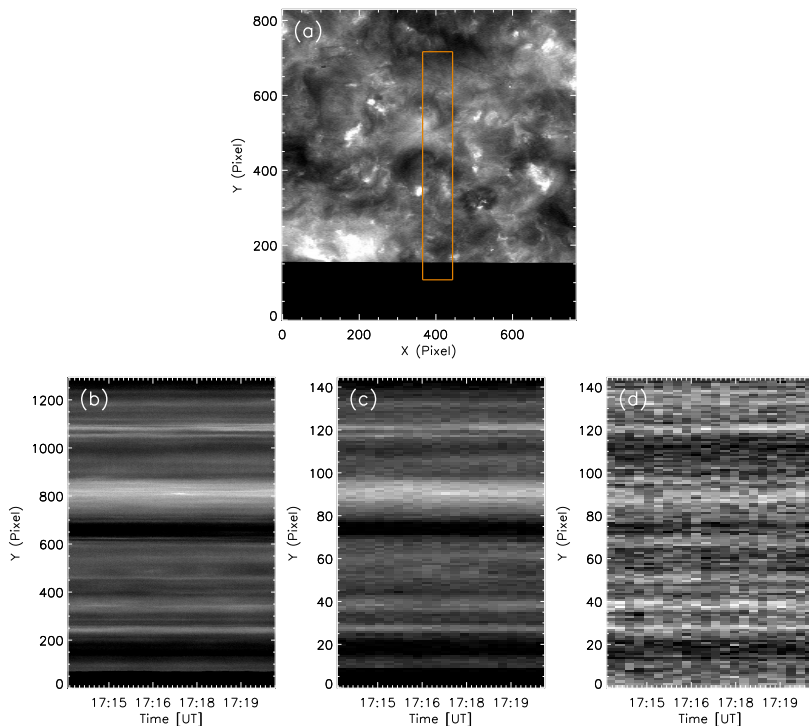


Figure 3.5: Illustration of the second step in data coalignment. Panel (a) shows an HRI_{EUV} image projected onto the SPICE context raster using WCS keywords from the file headers, with the orange box marking the region where the SPICE slit is initially estimated to be, based on the results from the initial coarse alignment. Panel (b) presents one example of the time-slice image of HRI_{EUV} data at full resolution from one of the slit positions indicated in panel (a). Panel (c) shows the same time-slice image as panel (b), but at a resolution reduced to match SPICE imaging resolution. Panel (d) provides the time-slice image of the Ne VIII line amplitude derived from Gaussian fitting results.

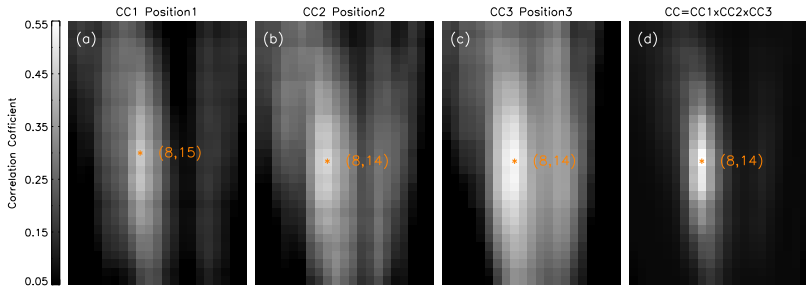


Figure 3.6: Maps of correlation coefficients. Panels (a)–(c) display the correlation coefficient maps calculated between the time-slice plots of the down-sampled HRI_{EUV} time-slice image and the Ne VIII amplitude time-slice image at three raster positions. The color bar on the left indicates the range of correlation coefficient values. Panel (d) shows the combined correlation coefficient map obtained by multiplying the correlation coefficients from the three positions. The orange stars indicate the slit positions corresponding to the maximum correlation coefficient, with their pixel coordinates provided in parentheses.

displays the product of these three correlation coefficient maps, with the peak indicating the final alignment refinement. For the 12/13 September data sets (sit-and-stare observations), the analysis is performed independently on the three individual time series when HRI_{EUV} and SPICE observed simultaneously.

Through precise alignment of the HRI_{EUV} and SPICE data, the locations of EUJ brightenings in the SPICE data are pinned, as identified in the HRI_{EUV} images. A straightforward way to compare the EUJ brightening signatures in both data sets is by reducing the resolution of the HRI_{EUV} data to match that of SPICE. However, to verify whether the SPICE slit covered the EUJ brightening structure during the simultaneous observation period, the full-resolution HRI_{EUV} data are used, as they provide a clear representation of the trace showing the evolution of the EUJ brightening in the time-slice images. In data set 1, which includes rasters with three spatial steps, a time-slice plot is generated for each spatial position. Data set 2 provides a time-slice plot at a single spatial position, but with higher temporal resolution.

3.4 Results

3.4.1 23 February 2021: Event E-1

Data set 1 reveals one EUV brightening E-1. Figure 3.7 shows the time-slice images at the second spatial position, where the EUV brightening is most prominent. A brightening is observed in the upper part of the slit, lasting approximately 40 seconds. Panels (a) and (b) of Figure 3.7 display the time-slice plots of HRI_{EUV} data at both full and reduced (to SPICE) resolution, respectively. In panel (b), the data have been degraded both temporally and spatially (along the slit) by selecting HRI_{EUV} data close in time to each SPICE spectrum and averaging the pixels to match the SPICE-binned spatial scale ($4'' \times 4.392''$). The brightening, marked by orange boxes, appears and fades in both time-slice plots, confirming that the brightening is detectable with the SPICE resolution.

Panel (a) of Figure 3.8 shows a sub-region of HRI_{EUV} observation covering EUV brightening E-1, taken near the peak time of it. It illustrates a clear view of the overall structure of E-1. In panel (b), the solid black line represents the light curve of this event, calculated over the solid box shown in panel (a), over the entire observation period. The HRI_{EUV} intensity (dashed line) is also measured over the SPICE pixel, indicated by the dashed box in panel (a), which shows no significant deviation from the HRI_{EUV} intensity of the whole event. Despite the small size of this EUV brightening (less than 4 Mm at its largest extent), the combination of the heliocentric distance of Solar Orbiter and the high spatial resolution of HRI_{EUV} allows for a detailed observation of this EUV brightening.

The time-slice images from all spectral lines obtained by SPICE are presented in Figure 3.7, along with the light curves showing the temporal variation in the line intensities. As mentioned before, four pixels are binned along the SPICE slit. The error bars, shown in orange, represent uncertainties of these intensities, propagated from the uncertainty of the returned Gaussian fitting parameters. It is noticed from the HRI_{EUV} light curve that the intensity of the EUV brightening increases by approximately 16%. However, among all the spectral lines provided by SPICE in this data set, only the O VI spectra show an increase when the EUV brightening appeared (from about 17:17 UT to 17:18 UT), although this increase is less pronounced than in the HRI_{EUV} light curve. The absence of a

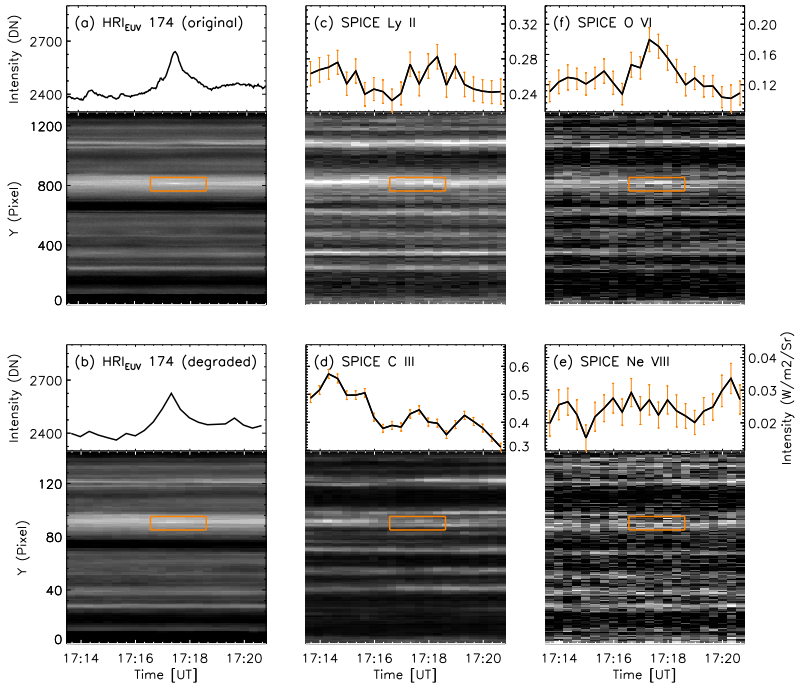


Figure 3.7: Observation of EUI brightening E-1 from 23 February 2021 at different temperatures. Panels (a) and (b) display time-slice plots of HRI_{EUV} images at both full and reduced (to SPICE spatial and temporal) resolution. Panels (c)-(f) show time-slice plots of intensity derived from Gaussian fitting results for Ne VIII, C III, Ly β , and O VI. The locations where the EUI brightening occurs are indicated by orange boxes. The curves at the top of each panel represent the intensities at these positions over time. Error bars, derived from the uncertainties in the fitting parameters, are shown in orange.

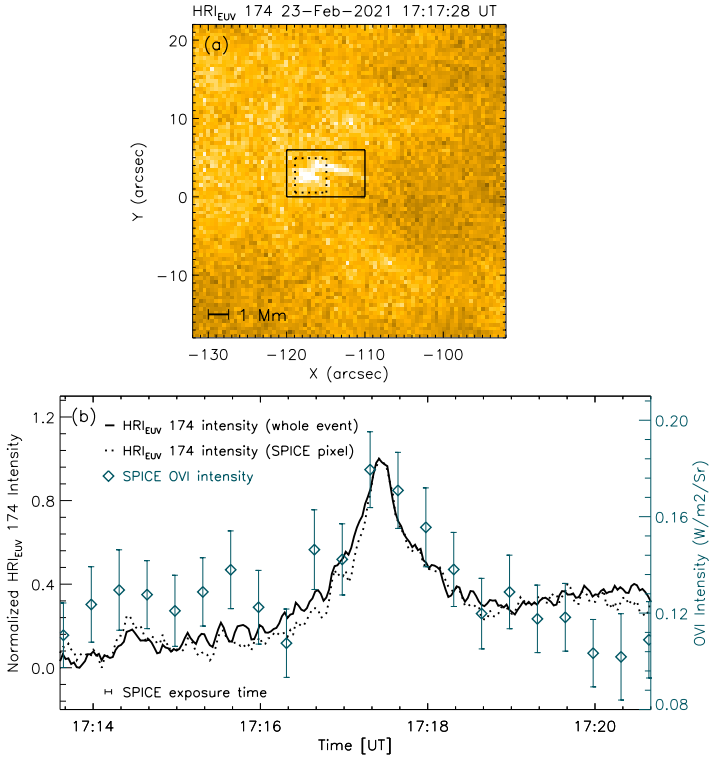


Figure 3.8: EUV brightening (E-1). Panel (a) displays an HRI_{EUV} image taken on 23 February 2021 at 17:17:28 UT, around the time when the intensity of the EUV brightening reaches its peak. The smaller dashed box indicates the area covered by a single SPICE-binned pixel ($4'' \times 4.392''$) during the second spatial step of the short raster. In panel (b), the O VI intensity at this pixel (blue diamonds) is derived from Gaussian fitting results of this line in the SPICE data, with error bars calculated from the uncertainties of the fitting parameters. This same region was used to calculate the HRI_{EUV} intensity (dashed line) in panel (b) for comparison. The larger solid box covers the whole event and is the area used to compute the light curve (solid line) in panel (b). A horizontal bar is drawn in the lower left corner to indicate the SPICE exposure duration (approximately 4.7 s).

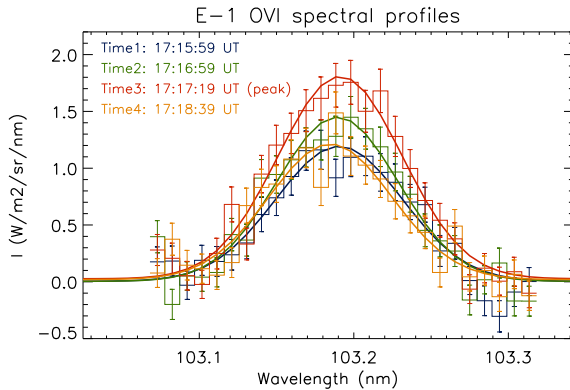


Figure 3.9: EU1 brightening (E-1). The O VI spectral profiles displayed as histograms with error bars of a binned SPICE pixel (indicated by the dashed box in panel (a) of Figure 3.8), are shown along with the Gaussian fitting results (thick lines) at four moments during the lifetime of E-1.

clear signal in Ne VIII may suggest that this EU1 brightening has a significant emission measure detectable by SPICE primarily at temperatures near the typical temperature of O VI (0.3 MK) and very little, if any, emission at coronal temperatures. The O VI light curve in Figure 3.8 indicates that SPICE may have missed the moment when the HRI_{EUV} intensity peaked, likely due to its 20 s cadence, which is nearly half of the duration of this EU1 brightening.

Figure 3.9 shows the O VI line spectra at four different times, illustrating the enhanced emission coinciding with the appearance of this EU1 brightening. The radiance of the O VI line reaches its maximum at time 3 (as labeled in Figure 3.9).

3.4.2 12 September 2021: Event E-2

In data set 2, the observations provided by HRI_{EUV} are separated in three time periods (see Table 3.2) and two EU1 brightenings are covered in the SPICE slit. Event E-2 was observed in the time series between 22:04 UT and 22:10 UT on

12 September, while event E-3 occurred between 00:19 UT and 00:23 UT on 13 September. Compared to E-1, these two EUV brightenings had longer durations (lasting approximately 6 min for E-2 and 4 min for E-3, different from less than one minute for E-1). Additionally, SPICE recorded E-2 and E-3 with a higher time cadence of 10 seconds (instead of 20 s) and a longer exposure time of 10 s (instead of 4.7 s).

Panels (a) and (b) of Figure 3.10 display HRI_{EUV} time-slice plots at both the original resolution ($0.5''$ spatially and 2 s temporally) and reduced resolution ($4''$ spatially and 10 s temporally) to confirm that the EUV brightening remains identifiable at SPICE resolution. The bright trace left by the event, highlighted within the orange boxes, and the corresponding intensity increase in the light curve are still apparent.

Figure 3.11 provides an HRI_{EUV} image of the structure at its brightest moment (panel (a)) along with light curves (panel (b)) for two regions: the solid box, which covers the entire event, and the dashed box, outlining the binned SPICE pixel. The brightening reaches its peak at around 22:06 UT. Additionally, the integrated Ne VIII line radiances at the EUV brightening location (represented by orange squares in panel (b)) are shown, with the light curves showing close temporal synchronization.

In Figure 3.10, the time-slice plots of the integrated radiances for all spectral lines provided by SPICE are displayed, along with their corresponding light curves. It turns out that, the signature of this EUV brightening is only visible in some of the lines. The Ne VIII light curve (panel (i)) aligns closely with the HRI_{EUV} light curve, peaking at the same time (22:06 UT), while the O VI light curve (panel (h)) displays a broader peak centered around 22:06 UT as well. In contrast, the light curves for N IV (panel (e)), S V (panel (g)), and O IV (panel (f)) seem to reach their maximum intensity slightly earlier. Since SPICE observations began only at the start of the plotted interval, it is likely that the rise phase of the brightening was not fully captured.

Figure 3.12 shows how the Ne VIII radiance evolves over time. The variation in peak times among the spectral lines may reflect a changing temperature during the event. Note that, cooler lines such as C III and Ly β exhibit no obvious change throughout the observation period.

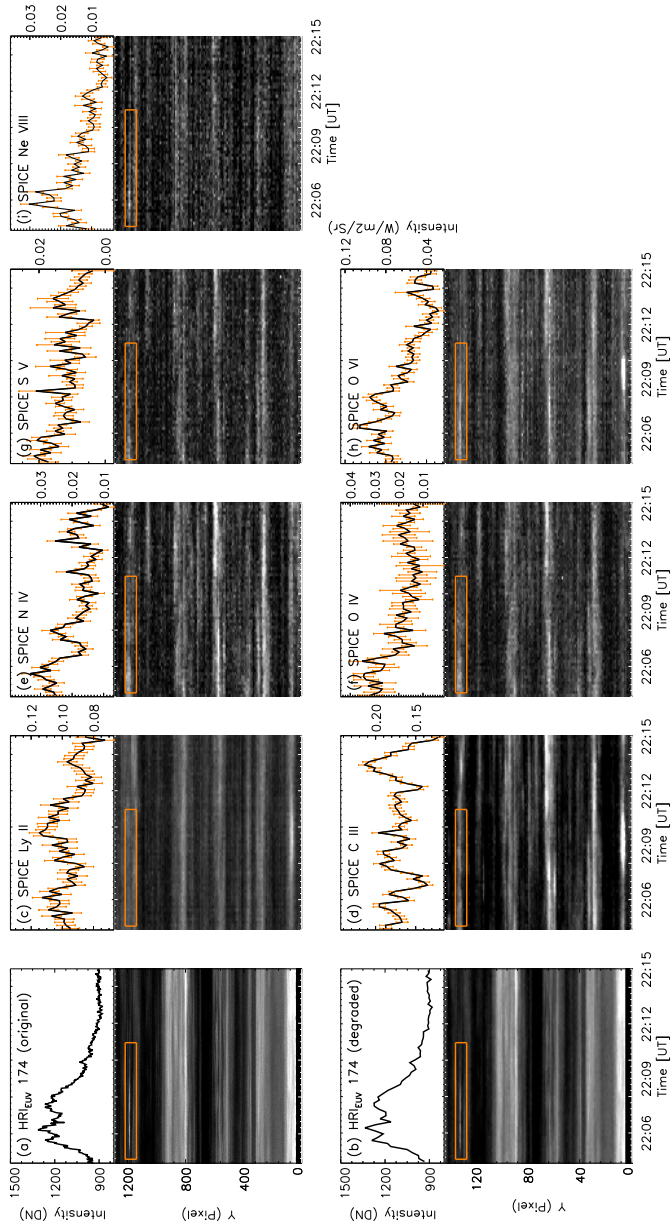


Figure 3.10: EUV brightening (E-2). Same as Figure 3.7, but for E-2 on 12 September 2021. It presents time-slice plots and light curves derived from HRI_{EUV} data at both full resolution and reduced (to SPICE) resolution, together with the intensity computed from the Gaussian fitting results of the spectral lines Ly β , C III, N IV, O IV, S V, O VI, and Ne VIII.

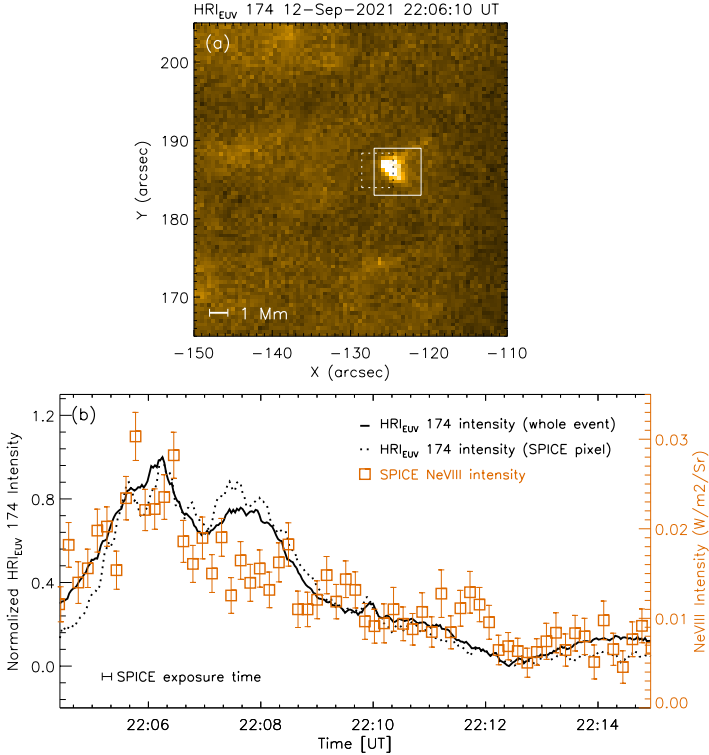


Figure 3.11: EUI brightening (E-2). Same as Figure 3.8, but for E-2 on 12 September 2021. The Ne VIII intensity evolution (orange) is presented in panel (b). The exposure duration of SPICE observation is 10 s in this case.

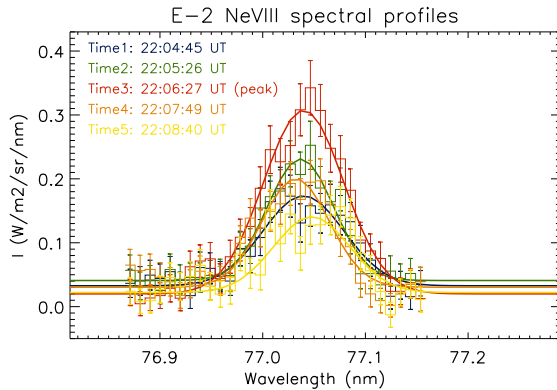


Figure 3.12: EUI brightening (E-2). The Ne VIII spectral profiles (histograms with error bars) are accompanied by Gaussian fitting results (thick lines) at five times during the lifetime of E-2.

3.4.3 13 September 2021: Event E-3

EUI brightening E-3 is also covered in data set 2 with high temporal resolution observations from SPICE. Figure 3.13 presents HRI_{EUV} time-slice images at both its full resolution (panel (a)) and a resolution adjusted to the spatial and temporal scales of SPICE (panel (b)). Even in the degraded image in panel (b), the EUI brightening remains visible, as confirmed by the corresponding light curve, demonstrating that it can be identified at the resolution of SPICE.

This EUI brightening appears as a loop-like structure located south of a larger, brighter brightening. Panel (a) of Figure 3.14 shows an image of the brightening and its surroundings at the moment it reaches peak intensity in the HRI_{EUV} channel. To analyze its intensity evolution, the region covering this EUI brightening, outlined by the white box in panel (a), is used to calculate the HRI_{EUV} light curve shown in panel (b). This curve represents the overall intensity variation of this event.

Additionally, the light curves from the SPICE spectral lines and the HRI_{EUV} data (dashed line) are computed for the area within the dashed box, and these are also included in panel (b). The only noticeable difference between the HRI_{EUV}

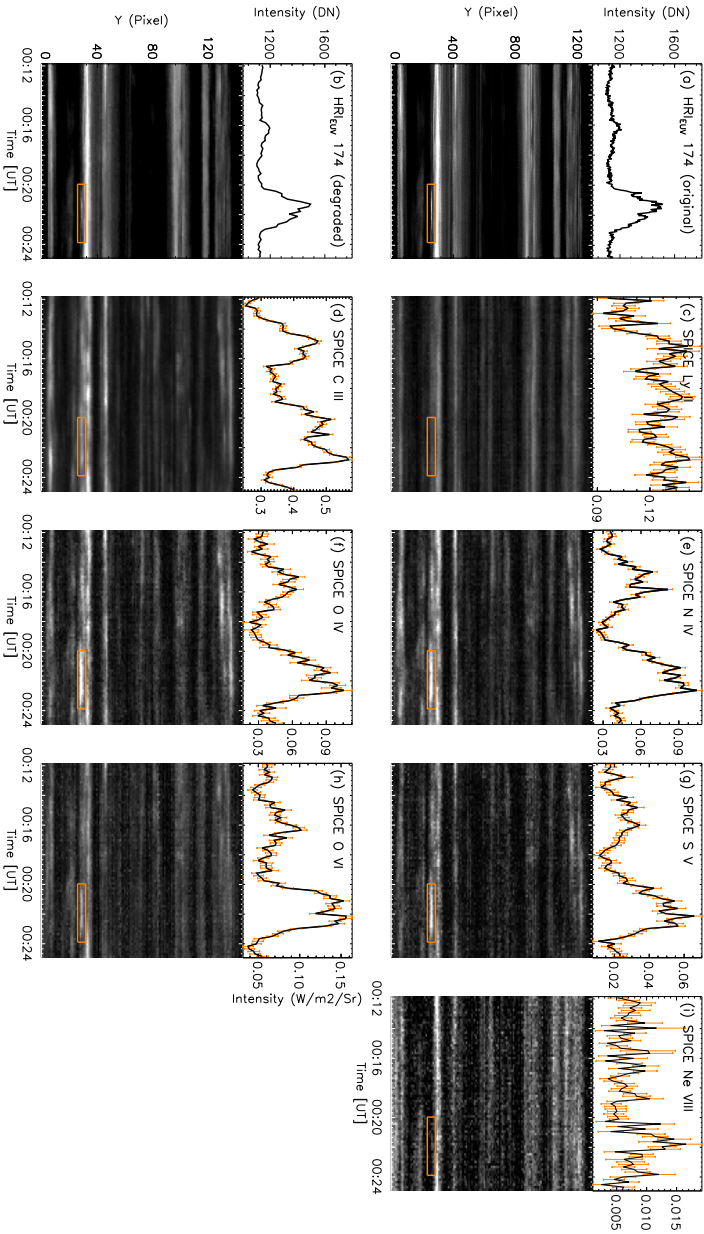


Figure 3.13: EUV brightening (E-3). Same as Figure 3.7, but for E-3 on 13 September 2021. It presents time-slice plots and light curves derived from HRI_{EUV} data at both full resolution and reduced (to SPICE) resolution, together with the intensity computed from the Gaussian fitting results of the spectral lines Ly β , C III, N IV, O IV, S V, O VI, and Ne VIII.

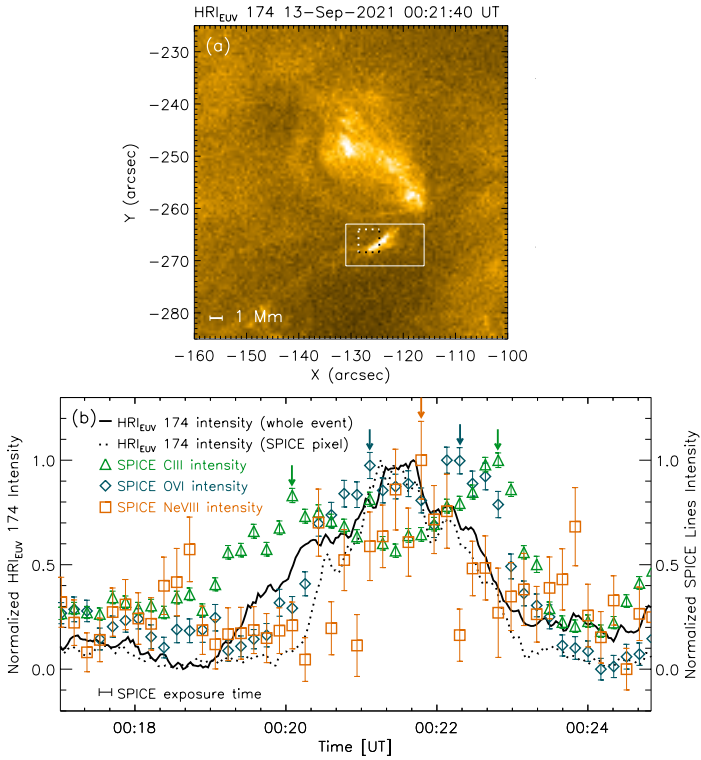


Figure 3.14: EUV brightening (E-3). Same as Figure 3.8, but for E-3 on 13 September 2021. The normalized intensity evolution of C III (green), O VI (blue) and Ne VIII (orange) lines are displayed. The arrows in corresponding colors point to the peaks of these lines. The exposure duration of SPICE observation is 10 s in this case.

light curve of the entire event and that of the SPICE-binned pixel region occurs around 00:20 UT. This discrepancy arises due to a smaller brightening preceding the main event, as illustrated in the top middle panel of Figure 3.15.

Figure 3.15 shows the evolution of EU1 brightening E-3, within the same region used to calculate the light curve in panel (b) of Figure 3.14 at nine different times, including those when the spectral lines reached their peak intensities. These images reveal that this brightening initially emerges as a compact, bright loop and then expands northwestward, forming a stretched structure. Before it appears, another faint loop is visible in the upper panels, west of the SPICE slit, moving from the northwest toward the southeast. It is likely that this faint loop could have transferred energy to one of the footpoints, triggering the EU1 brightening observed within the SPICE slit.

Similar propagations of brightenings have been reported by Mandal et al. (2021). Chitta et al. (2021b) reported a comparable behavior in jet studies, where reconnection occurs between a local bipolar magnetic field and either an open field or one that connects to a far footpoint (Heyvaerts et al. 1977; Shibata et al. 1992). Some small-scale jets are associated with footpoint brightenings, which can reach temperatures of at least 10^5 K (Tian et al. 2014).

Panels (c) to (i) of Figure 3.13 display the Gaussian fitting results for the SPICE spectral lines, illustrating enhanced emission in Ne VIII and several transition region lines during the peak of the EU1 brightening. The light curves tracking the temporal variation of line intensities reveal that some transition region lines exhibit two distinct peaks around 00:22 UT when the HRI_{EUV} and Ne VIII intensities peak (panels (a) and (i) of Figure 3.13). More details can be found in Figure 3.14. The double peaks are especially noticeable in the evolution of the O VI spectral profiles, as displayed in Figure 3.16. The different peak times across spectral lines suggest an evolution of plasma temperature throughout the event.

Both light curves of O VI and C III feature two peaks, but their timing varies: the peaks for C III are further apart, while those for O VI occur closer to the single peak of Ne VIII (see Figure 3.14). This suggests that the plasma temperature could first increase, starting from the typical temperature of C III

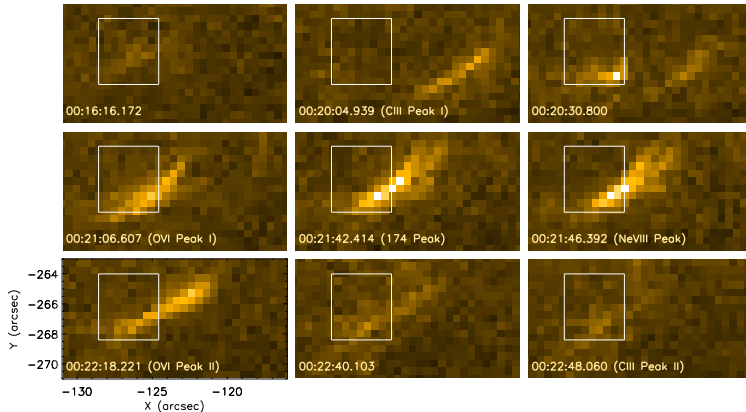


Figure 3.15: HRI_{EUV} snapshots of EUV brightening E-3 at nine different times, including when the intensities of HRI_{EUV} 174, SPICE Ne VIII, C III and O VI reach peaks. The white box in each panel indicate the area of one binned SPICE pixel covering the EUV brightening.

($\log T[/math>/K] = 4.8), rising to O VI temperature ($\log T[/math>/K] = 5.5), and eventually reaching Ne VIII temperature ($\log T[/math>/K] = 5.8), which corresponds to the lower corona. After the peak time of Ne VIII, the plasma begins to cool down, returning to transition region temperatures, which explains the second emission peaks in O VI and C III lines.$$$

Before this brightening occurs, at about 00:16 UT, another noticeable enhancement can be observed in the transition region lines, as shown in Figure 3.13. This could be explained as another smaller, related brightening or as a precursor to the main event. Although the HRI_{EUV} light curves also reflect this feature, its intensity is significantly lower compared to the EUV brightening under investigation here. Similarly, the upper-left panel of Figure 3.15 reveals a faint brightening within the SPICE pixel minutes before the occurrence of the target EUV brightening. This initial brightening likely reaches only lower temperatures and might indicate an energy buildup leading to the EUV brightening.

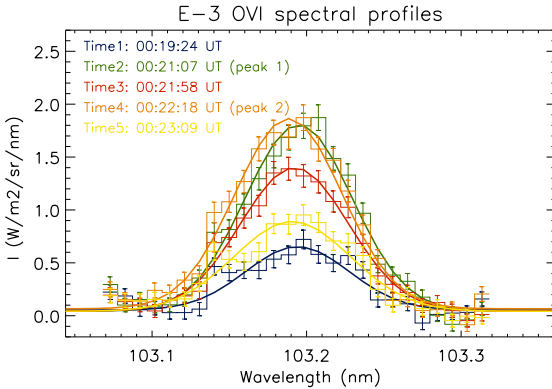


Figure 3.16: EUI brightening (E-3). $O\ VI$ spectral profiles (histograms with error bars) are accompanied by Gaussian fitting results (thick lines) at five times during the lifetime of E-3.

3.4.4 DEM analysis

The observations of multiple lines formed at different temperatures can also be used for the DEM analysis, which could provide the distribution of the emission measure over the temperature. The DEM analysis is done based on IDL routines developed by Young (2018) and by applying CHIANTI data base to look up for the transition information of the interested lines (Dere et al. 1997). Because more lines at different temperatures are required to constrain the model, only the data set 2 (12/13 September 2021) is used. Additionally, DEM method is based on the assumption of an optically-thin environment, so the $Ly\beta$ line, which forms at lower heights like in chromosphere where hydrogen is more abundant, is excluded from the calculation.

The DEMs are calculated by simply assuming a multi-linear form Young (2005a,b, 2018). It is computed over the range of 4.5 to 5.8 in $\log T$, while the minimum is set at $\log T=5.2$ (Raymond and Doyle 1981). A constant pressure of $10^{15} \text{ K cm}^{-3}$ is applied, considering a typical temperature of 10^6 K and electron density of 10^9 cm^{-3} . The line intensities and the corresponding

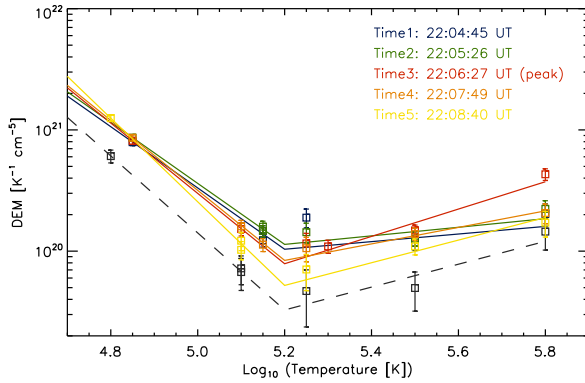


Figure 3.17: DEMs (Log T- DEM space) of the EU1 brightenings E-2 at five times and over the same binned SPICE pixel as done to obtain the profiles in Figure 3.12. The dashed line is a reference done by averaging all binned SPICE pixels along both the slit direction and time. Squares (with bars) indicate the observed line intensities (with errors) at its effective line formation temperature computed in the DEM routine.

errors are calculated by Gaussian fitting and Equation 3.6.

The DEM results are displayed in Figures 3.17 (E-2) and 3.18 (E-3). Lines in different colors are DEMs at different times, corresponding to the times when spectral profiles are shown in Figures 3.12 and 3.16. The same binned SPICE pixels as the dashed boxes in Figure 3.11 and 3.14 are selected. The dashed lines are calculated based on the averaged intensity over all binned SPICE pixels and along the time, to represent a quiet sun background. It is obvious that the emission from the EU1 brightening E-2 is higher than the background while in the case of E-3 the background emission is larger when the brightening just appears and is decaying. This is likely due to the large brightening south to E-3 that is also captured in the SPICE slit. At the peak time of the Ne VIII line of E-2 (time 3), there is an obvious increase in the DEMs at higher temperature. In Figure 3.18, the DEMs at the three middle times are higher than at the first and last times, but very close to each other. Considering the errors and the assumptions

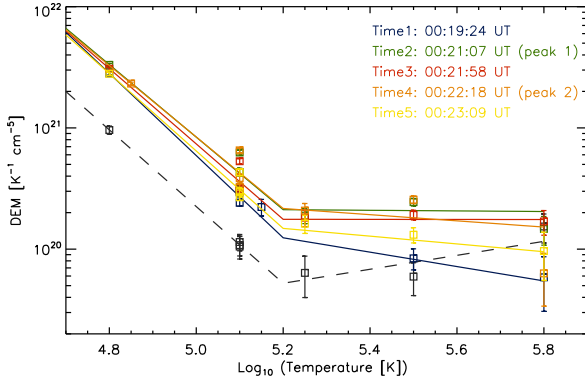


Figure 3.18: As in Figure 3.17, but for EUI brightening E-3. The DEMs are computed at the same time as indicated in Figure 3.16.

made in the model, the thermal structure and evolution of these events remain inconclusive.

The DEM method provides similar thermal information as other plasma diagnostic techniques but fails to clearly reveal the thermal evolution of plasma in these cases. Additionally, the DEM method relies on several assumptions and simplifications, such as defining a fixed minimum temperature or using linear fitting techniques. These assumptions can introduce variability in the results, making them sensitive to the chosen parameters and models. Despite these challenges, DEM remains a powerful diagnostic tool for investigating plasma properties. With more complete data sets that include multi-thermal observations spanning a broader range of temperatures, DEM analyses could yield significantly more reliable and detailed results.

3.5 Discussion and Conclusion

Three EUI brightenings that were simultaneously observed by HRI_{EUV} and SPICE on board Solar Orbiter are investigated in this study. The first event took place on 23 February 2021, during which a series of three-step SPICE rasters with a

20s cadence were obtained. This event lasted for about 40s. The other two events appeared on 12 and 13 September 2021, during which SPICE operated continuously in sit-and-stare mode with a 10s cadence. These two events lasted for minutes. It is important to note that the scales of all three EUJ brightening events are almost at the limit of SPICE observational capability. As a result, their identification relies heavily on the high-resolution imaging provided by HRI_{EUV}.

By combining the high-resolution HRI_{EUV} imaging data with the spectral data from SPICE, I find that the first event is only detectable in the O VI line, while the other two longer-duration EUJ brightenings are visible not just in transition region lines but also in Ne VIII, a line formed at (low) coronal temperatures. For these two events, Ne VIII shows a single emission peak that coincides with the peak observed in HRI_{EUV} data. This suggests that some EUJ brightenings can barely reach the temperatures typically associated with the corona. Supporting this idea, double peaks are observed in the light curves of transition region lines, while Ne VIII shows just one peak between the two peaks from the cooler lines. These results help to understand the heating and cooling process of the EUJ brightening, which seems to heat up to lower-coronal temperatures before cooling down. Unlike Berghmans et al. (2021), who suggested that EUJ brightenings reach coronal temperatures, the findings here imply that these events likely remain at lower temperatures. A similar conclusion was drawn by Dolliou et al. (2023), where a time-lag analysis of the light curves of EUJ brightenings observed in different AIA channels (probing different temperatures) indicates that the plasma in those events is predominantly cool and does not reach coronal temperatures. Apart from the thermal evolution explanation, variations in peak times could also be due to the spatial motion of the EUJ brightenings. Since the SPICE slit is relatively narrow and the EUJ brightenings are active, there is a possibility that some of the brightenings move in and out of the slit, affecting the observed light curves.

To determine if the findings here are generally applicable to more EUJ brightenings, further studies with additional samples are needed. This research clearly demonstrates that SPICE is capable of observing EUJ brightenings, but the small size of these events means that high-resolution imaging from instruments like EUJ is essential for clear detection. Given the rapid evolution of EUJ brighten-

ings, observations with a higher time cadence, such as in sit-and-stare mode, would provide valuable insights. Although the fixed position of the SPICE slit in sit-and-stare mode limits its ability to capture more small brightenings, the high frequency of EUI brightening occurrences increases the likelihood of observing at least some of them along the slit. As Solar Orbiter has reached its nominal science phase, more events are expected to be detected by both HRI_{EUV} and SPICE. These observations will be further enhanced by high spatial resolution observations conducted particularly around the spacecraft's perihelia. Additionally, other instruments, such as IRIS, offer complementary data that can be combined with the HRI_{EUV} observations to enhance our understanding of EUI brightenings. For instance, Nelson et al. (2023) studied EUI data taken on 8 March 2022 together with coordinated IRIS observations to investigate the response of EUI brightenings in transition region lines. Some of the brightenings in that data set show clear simultaneous signatures in the Mg II and Si IV lines, though no typical transition region response is observed for these events. Studying more of these small-scale brightenings will deepen our understanding of their heating mechanisms and their role in coronal heating.

Chapter 4

Brightenings in the coronal holes

This work was carried out based on discussions with L. P. Chitta, L. Teriaca, R. Aznar Cuadrado, H. Peter, S. K. Solanki, T. Wiegelmann and F. Plaschke. The magnetic field extrapolation was performed by T. Wiegelmann.

4.1 Introduction

Coronal hole plumes generally appear as extended ray-like structures within coronal holes. Their observations can be traced back to the early 20th century and a great number of studies have been conducted on plumes (see review by Polletto 2015). Plumes expand super-radially into the outer solar atmosphere to over $30 R_{\odot}$ (Woo and Habbal 1997; DeForest et al. 2001). They are found to be cooler and denser features compared with the ambient interplume regions (Ahmad and Withbroe 1977; Wilhelm et al. 1998; DeForest et al. 2001; Wilhelm 2006). Once a plume is formed, it can last for tens of hours (Lamy et al. 1997) to days (Young et al. 1999) with successors appearing at the same positions in weeks (DeForest et al. 2001).

Plumes are observed in visible light (e.g., Saito 1956), in EUV (e.g., Ahmad and Withbroe 1977; Walker et al. 1993), and in soft X-rays (e.g., Ahmad and Webb 1978). Due to the observing geometry (from or close to the ecliptic plane) and generally large sizes of polar coronal holes (low background), polar plumes are easier to be observed projecting well beyond the limb of the Sun, indicating the inhomogeneity of the outer solar atmosphere and providing information on the general magnetic field of the Sun (Shimooda 1958). On the other hand, tracing plumes in low-latitude coronal holes to greater heights is more difficult because of the much higher background from the nearby quiet sun and, often, active region areas. Nevertheless, these plumes are best observed against the disk, in UV and EUV emissions (e.g., Wang and Sheeley 1995b; Wang and Muglach 2008).

Plumes are found to be closely related to the chromospheric network, which is the pattern outlining the convective supergranular cells. Newkirk and Harvey (1968) proposed that the rosette structures at the intersection of the network lies at the root of plumes. Data from SOHO have revealed strong evidence of the spatial coherence of polar plumes and the network (DeForest et al. 1997). Gabriel et al. (2009) proposed that the observations of "curtain plumes" can be modeled by microplumes appearing at the 5 Mm width boundaries of the supergranular cells. It has been suggested by Wang and Sheeley (1995a) that the magnetic flux concentrations at the edges of network cells reconnect with the small bipoles pushed there by horizontal supergranular convective flows to produce plumes (also see Wang 1998 for the schematic).

Fast solar wind, which is also believed to originate from coronal holes is possibly sustained, at least in part, by coronal hole plumes. To establish the possible contribution of plumes to the solar wind, it is essential to measure the speed of plume outflows at different heights. Numerous studies have been conducted over the years (e.g., Habbal et al. 1995; Corti et al. 1997; Wilhelm and Bodmer 1998), with different measurement methods and have yielded widely-spread conclusions. For instance, off-limb plumes are investigated with the Doppler dimming method (Noci et al. 1987). Gabriel et al. (2003, 2005) proposed a velocity of beyond 60 km s^{-1} embedding in the plumes, from 1.05 to $1.4 R_{\odot}$, exceeding that in the interplume regions. However, Teriaca et al. (2003) found that static plumes in

the outflowing interplume nicely reproduce the observational lines. In the low corona, some studies measuring Doppler shift of lines in SUMER data failed to retrieve any obvious signature of outflows in plumes (Hassler et al. 1999; Hassler 2000; Wilhelm et al. 2000). In Feng et al. (2009), the stereoscopic reconstructions of polar plumes correct the outflow velocity demonstrated in O VI 1032Å and 1038Å lines to values below 10 km s^{-1} . Using observations of plumes in multiple spectral lines by EIS, Fu et al. (2014) concluded that plume outflows are quasi-steady with a velocity increasing with height and can be an important source of solar wind. A summary of the outflow speeds both obtained there and from the previous literature can also be found in this paper.

The launch of SDO opened a new era in the study of plumes. Instead of being a spatially coherent "haze", plumes were seen to be formed of filamentary fine structures, the so-called "plumelets" (Uritsky et al. 2021). In addition, numerous small jets (so-called jetlets) and plume transient bright points (PTBPs) have been reported to occur in plumes (Raouafi and Stenborg 2014; Pant et al. 2015; Panesar et al. 2018; Kumar et al. 2022; Chitta et al. 2023b). Raouafi and Stenborg (2014) also proposed that these small-scale energy releases may sustain the evolution of plumes in the long term.

Propagating disturbances (PDs) are observed in the plumes as the quasi-periodic temporal fluctuations of brightness. They are found to move outwards along the plume filamentary structures in speeds varying from a few 10 km s^{-1} to over 200 km s^{-1} . However, their physical nature is not fully understood yet. On the one hand, PDs are thought to be caused by mass flows (McIntosh et al. 2010; Tian et al. 2011). On the other hand, in many studies they are interpreted to be the signatures of magnetosonic waves (DeForest and Gurman 1998; Ofman et al. 1999; Banerjee and Krishna Prasad 2016; Banerjee et al. 2021). However, using multi-channel observations, Pucci et al. (2014) found that the PDs have higher speeds at lower temperatures, which is inconsistent with the wave scenario. More recently, Kumar et al. (2022) suggested the coexistence of strong flows and waves in plumes.

Various studies have shown that plumes have fine internal structures with high-speed PDs and dynamic base regions with numerous transients. They all might be associated and play a role in the formation and evolution of the entire

plume and contribute to the solar wind. However, the characteristics of the base dynamics and their relation with the plume PDs are not clearly known. High-resolution observations of plumes are essential to understand these. Observations by Solar orbiter mission, acquired near one of the closest perihelia at about 0.3 au, provide detailed information about the fine-scale structuring and small-scale dynamics in plumes. This work focuses on analyzing the characteristics and movements of these dynamic brightening structures using high-resolution data from HRI_{EUUV}. Given that the nature of small-scale activity at plume bases is not yet conclusively known, it is referred to as "brightenings", based on the observations.

4.2 Observation overview

To study the base regions of plumes, an equatorial coronal hole captured by EUI on 13 October 2022 adjacent to active regions, is selected. Three plumes were embedded in the observed coronal hole, south of NOAA 13105 and west of NOAA 13107. The observations were taken when Solar Orbiter was at a distance of 0.29 au from the Sun, and at an Earth Ecliptic longitude of about -107° . With its 17.4 nm filter the HRI_{EUUV} instrument recorded a 30-min long imaging sequence from 17:00:00 UT to 17:30:00 UT, at a cadence of 5 s with an exposure time of 2.8 s. This high temporal resolution is decreased to 20 s after binning 4 images together to reduce the noise level during data preparation. HRI_{EUUV} images have a angular image scale of $0.492'' \text{ pixel}^{-1}$, corresponding to about $100 \text{ km pixel}^{-1}$ (spatial resolution of about 200 km) at 0.29 au.

Figure 4.1 (a) shows an image of the Sun provided by FSI of EUI on Solar Orbiter at 17:10:50 UT. FSI observed the full sun disk at a spatial resolution of about 1800 km and a cadence of 10 min. Available observations cover the whole lifetime of these plumes. Since this study focuses on the small dynamic activity in solar plumes, I mainly use high resolution images from HRI_{EUUV}. The box in panel (a) indicates the region covered by HRI_{EUUV}, shown in panel (b). To enhance the plumes, which are, even though brighter than their coronal hole background, still much fainter than the active regions and quiet sun in the neighborhood, the images in panels (a) and (b) are plotted in log scale. The

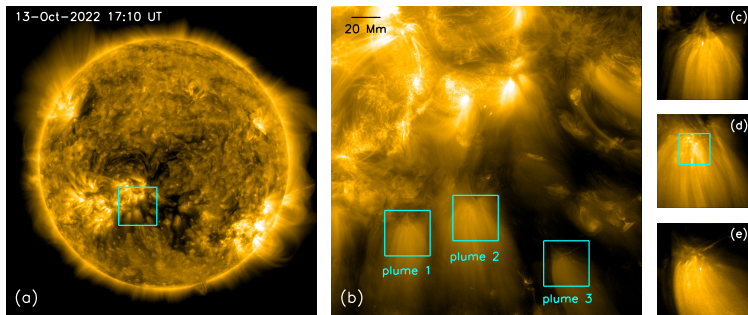


Figure 4.1: Overview of coronal hole observations. (a) Full-disk image of the Sun provided by FSI of EUV. The box indicates the region covered by HRI_{EUV}. (b) Image taken by HRI_{EUV} with three boxes showing the base regions of the three plumes shown in panels (c)-(e). Both (a) and (b) are plotted on a log scale in brightness. (c)-(e) Zoom-in normalized images of the base regions of the three plumes.

zoom-in images of the plume base regions of the three plumes are shown in panels (c)-(e).

As shown in Figure 4.1 (a), these three plumes are rooted in an equatorial coronal hole in the southern hemisphere. The positions of these plumes are close to the disk center with a heliocentric separation angle of about 25 degrees, which allows observations of the base region with relatively low distortion. Meanwhile, at greater heights, the strong magnetic fields of the active region to the north could push the plume magnetic field southward. Thus, the resulting EUV emission from the plume is apparently more parallel to the POS, which is better suited to study the movements of the fine structures in the plumes. The FSI sequences show that all the plumes have been existing for more than 1 day and will disappear in about 20 hours after this HRI_{EUV} observation period while plume 3 appears to be already in its decay phase.

Comparing the three plumes, the features labeled 1 and 2 are found to share similar characteristics that both of them are located near the boundary of the active region with north to south orientation. Plume 3 is rooted in the interior

section of the coronal hole and is oriented in a north-eastern to south-western direction. Plume 1 and 2 are also brighter than plume 3. Considering that plume 3 is already decaying, this agrees with the suggestion in Pucci et al. (2014) that plumes die as their gas density is reduced. Despite these differences, all the plumes have highly-dynamic base regions with brightenings appearing near their footpoints and moving outwards.

4.3 Data analysis

4.3.1 Visual identification method

To better capture the moving bright features in the base regions of the plumes, I first apply a method based on visualization. Before detailed analysis, the data are prepared by averaging over 4 consecutive images and then applying a running average over 3×3 pixels to each resulting image to reduce the noise. To make the data from the three plumes directly comparable, each base region (see Figure 4.1 (c)-(e)) is normalized to the maximum and minimum intensities of the whole sequence in each sub-region. Here, I apply the Difference of Gaussian (DoG) method, which is an image processing technique used to enhance edges or features in an image by highlighting areas of rapid intensity change (Lindeberg 1994; Lowe 2004). It involves subtracting two Gaussian-blurred versions of the same image. In this study, two Gaussian kernels with $\sigma = 3$ pixel and $\sigma = 5$ pixel, respectively, are applied. Different thresholds on DoG maps have been tested and 0.01 (see Section 4.3.3) is selected as a reasonable number to cover brightenings as much as possible while avoiding connections of brightenings close to each other.

Contours representing the target brightenings at different times are overplotted on the same images to show the trajectory of the brightenings. To decrease overlap, the entire observational sequence (30 min) is divided into four distinct time intervals, each covering specific enhancements in the light curve of the base region (see Figure 4.2 (a)). Figure 4.2 (b)-(e) show the brightening contours obtained with the thresholds of 0.01 on DoG maps in four different time spans. Brightenings appearing at different times are marked with different colors (see

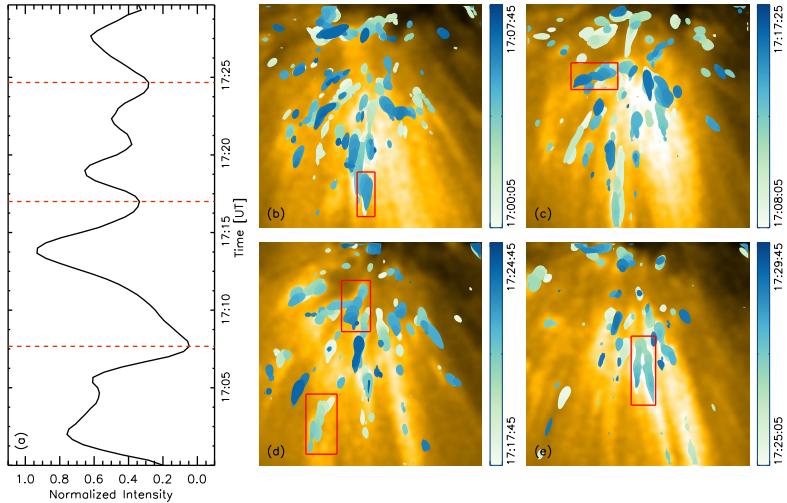


Figure 4.2: Dynamics at the base of plumes. (a) A sample light curve obtained from the base region of plume 2 (see Figure 4.1 (d)). The whole time period (30 min) is divided into 4 sections (partitioned at orange dashed lines). (b)–(e) Images of the base region of plume 2 acquired at the middle instance from each temporal section. Brightenings identified using chosen thresholds are marked by the contours (colors indicate time progression; as defined by the color bars). The red boxes highlight several examples of the "gradient patterns", which are formed by contours from successive frames being adjacent to or overlapping one another, thereby illustrating the movement of the brightenings. Note that, even though the entire observation has already been divided into four sub-periods, the contour of the brightenings that appears later will inevitably overlap the ones that appear earlier. For example, a discrete contour could be either a brightening that only appears in one frame, or a brightening that does not show a significant movement.

color bars in Figure 4.2). In these images, the "gradient patterns" (the overlapping contours with changing colors, see examples in red boxes in Figure 4.2) indicate the moving structures. Based on these "gradient patterns", the images are checked to pick up moving brightenings. A few brightenings existing in two time spans are checked throughout their whole lifetimes and still counted as the same ones. With this method a total of 50 brightenings are selected in the three plumes.

For each brightening, a local background calculated around its position as the minimum value at each pixel obtained along the brightening's lifetime is subtracted. After removing the background, brightenings show up better and the boundaries of them are then re-defined by using a new threshold, which is 0.75 of the maximum value of the brightenings, after several thresholds being tested (see Section 4.3.3).

4.3.2 Automatic method

The visualization method allows to select only those brightenings which are relatively large and bright and experience noticeable shifts in positions. This likely introduces a selection bias. To mitigate this, an automated selection method is also implemented to detect brightenings in the three plumes. Same as for the visual identification method, the DoG method is applied to each averaged image and the detection starts with a threshold of 0.01 in the enhanced images. All pixels with a value higher than this threshold are labeled as "bright pixels". In each frame, connected bright pixels are considered as a single brightenings by doing a 4-neighbor search. Small fragments (less than 2×2 pixels) are ignored.

For every brightening detected, the subsequent image frame is examined. If within a given neighborhood of this brightening a brightening larger than 2×2 pixels is found, then both are regarded as part of the same evolving structure, seen at different times. Here, the neighborhood that is searched for brightenings, is defined as a region centered on the peak of the brightening at the previous timestep with a radius of 6 pixels. The examination then continues with the next frame, based on the newly-evolved brightening until it (the brightening) becomes unrecognizable. Considering the pixel size of 100 km and time cadence of 20 s,

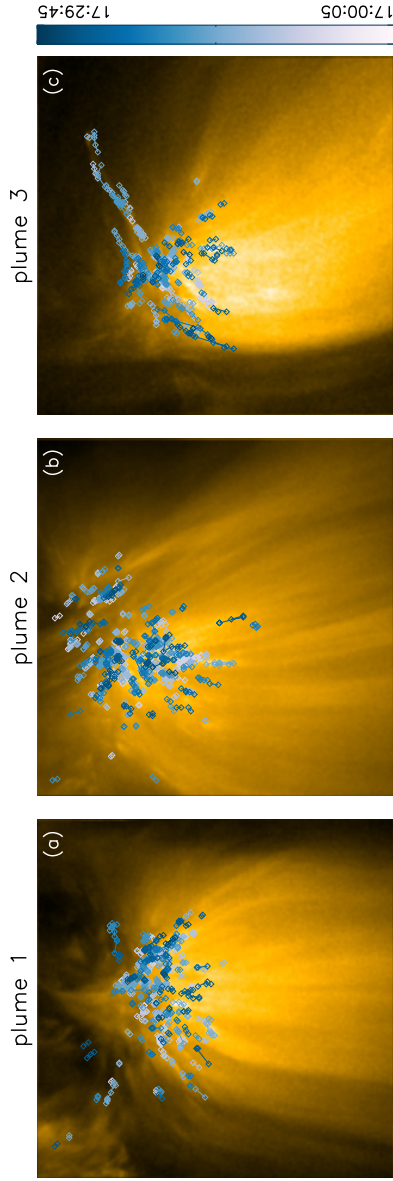


Figure 4.3: Zoom into the plumes bases observed on 13 October 2022 17:10 UT. The intensity-weighted center of each brightening along the evolution is overlotted on the images. The color of each brightening represents the time of its first appearance (see the color bar).

the threshold of 6 pixels corresponds to a velocity of 30 km s^{-1} . More details about the threshold selection can be found in Section 4.3.3. All the brightenings that appear in only one frame are ignored.

A total of 451 brightenings are picked up with this method. Their boundaries are also re-defined as 0.75 of the maximum value of the brightenings after the local background being removed. The positions of all brightenings are shown in Figure 4.3 where diamonds show the positions of the intensity-weighted centers of each brightening over its temporal evolution. The colors represent the start times of brightenings. The detected brightenings are also compared with those picked up by visual identification and most brightenings selected manually are also captured using the automatic method. However, fluctuations in brightness over time and the spatial proximity of different brightenings can result in discrepancies in some events.

4.3.3 Comparisons of thresholds

In these detection methods described above, several thresholds have to be selected carefully. First, both visual identification method and automatic detection use the DoG method, which provides the difference between the original image convoluted with two Gaussian kernels with different widths (σ). This algorithm can provide an approximation of the Laplacian of Gaussian (LoG) but is much easier to calculate. Here two Gaussian kernels with $\sigma = 3$ pixel and $\sigma = 5$ pixel are used given that a ratio around 1.6 is recommended to provide the best approximation of LoG. The intensity at each pixel of a DoG map represents the local intensity change. A DoG map may contain both positive and negative values, where positive values show bright edges or features while negative values indicate dark features or recessed edges and the zero-crossings correspond to locations of maximum gradient, that is, the edge features. In reality, zero-crossings can be very noisy and cause different brightenings to be connected, i.e., to blend with each other. Therefore, a positive threshold works better to capture edges of intensity enhancement and here a reasonable threshold of 0.01 after testing, which is roughly 3-standard-deviations of the DoG image, is used.

In automatic detection, to consider evolving brightenings, a threshold is set

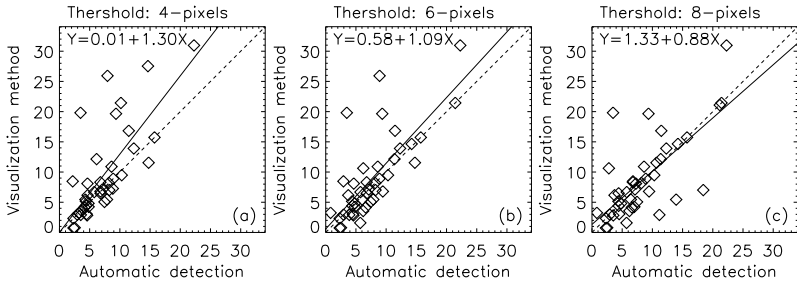


Figure 4.4: Scatter plots showing correlations of the velocities of the same structure obtained from different methods. In (a), (b) and (c), the threshold describing the neighborhood in which the following frame is searched for the moving brightening is set to 4 pixels, 6 pixels and 8 pixels separately. The dashed diagonals show the ideal case of equal velocities from both methods, while the solid lines are the linear fittings. The fitting parameters can be seen in the upper left corner of each panel.

up to define the neighborhood. In other words, in two consecutive frames, a moving structure should appear within a certain distance. The threshold setting this distance is selected based on the knowledge from visual identification method that the majority of brightenings move with a velocity of less than 10 km s^{-1} but the velocity of fast ones can go up to 30 km s^{-1} . With the pixel size of $100 \text{ km pixel}^{-1}$, thresholds of 4, 6 and 8 pixels are tested. As the distance threshold increases, the number of brightenings obtained decreases but the proportion of longer-lived brightenings increases. To test the reliability of different thresholds, I pick out in the automatic method the same brightenings detected based on visual identification and compare their properties.

Not all brightenings correspond to each other in the two methods. In a few cases, differences are caused by two visually detected brightenings being combined by the automatic method due to spatial nearness or one visually detected brightening being separated by the automatic method because of the brightening getting too faint to be marked in a middle frame. Among all the properties, the intensity matches the best and lifetime displays significant discrepancies, likely

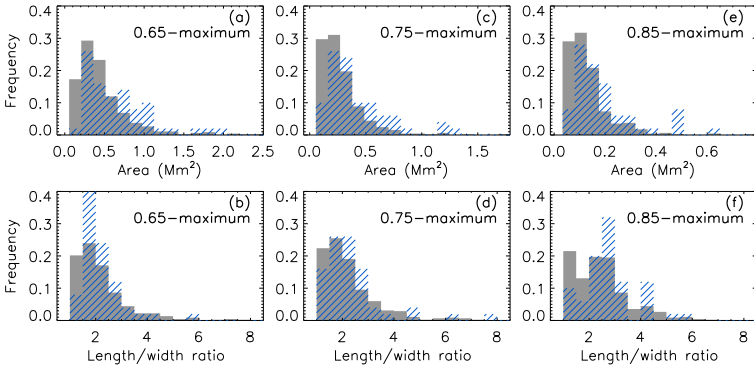


Figure 4.5: Normalized distributions of areas (upper panels) and length/width ratio (lower panels) of the brightenings detected in both methods. The grey bars show results from automatic method and the blue line-filled bars are results from visual identification method for comparison. From left to right panels the boundary threshold are 0.65, 0.75 and 0.85 of maximum.

due to the short duration and the 20 s cadence. The area and length/width ratio highly depend on the selection of the boundary of brightenings.

Here the comparison of velocity are shown in Figure 4.4. Panel (a) shows that the most points deviate from $Y = X$ when the threshold is set to 4 pixels. The majority of deviations are concentrated in the upper half of the scatter plot with the threshold of both 4 pixels and 6 pixels, i.e., the velocities obtained by automatic detection are smaller compared to those from the visual identification method. This is not the case with a threshold of 8 pixels, which shows a more balanced distribution. However, by checking the image one can see that it mixes many brightenings that are spatially close. Therefore, 6 pixels is chosen as a reasonable threshold.

Another concern is about the determination of the outer boundary of each brightening, which influences the property calculations in both methods. In the first step, a threshold of 0.01 is chosen based on DoG maps to define the outline of each brightening. While this method works well to get the location of the brightening, the outer boundary thus defined takes into account both

the enhancement and background. This is the reason why the boundary is then re-defined based on the images with the local background removed. The tested thresholds are 0.65, 0.75 and 0.85 of the maximum intensity within each brightening based on the background-removed images.

Figure 4.5 shows the distributions of area and length/width ratio when different thresholds are selected. The area of brightenings, although changing significantly in value depending on the selection of the threshold, shows consistent distributions that brightenings with a relatively smaller area have a higher occurrence frequency. Differently, the selection of the threshold affects the distribution of the length/width ratio. With increasing threshold, more brightenings detected by the visual identification method tend to show a relatively high length/width ratio of around 3, which does not correspond with the results from the automatic method. The distribution shows a strong peak at about 2 when the threshold equals 0.65 of the maximum. Also note that when the threshold goes down to 0.65 of maximum, the 2-dimensional Gaussian fitting has more difficulty converging, which means the shape of brightenings is more uneven. In this work, considering all the above factors, a threshold of 0.75-maximum is used for the outlines of brightenings.

4.3.4 Properties of brightenings

For all the brightenings selected with both methods, their properties (area, lifetime, intensity, length/width ratio and velocity) are investigated statistically. Based on the boundaries of brightenings defined on images with background subtracted as described above, one can easily get the area and average intensities, which are defined at the maximum along the evolution of each brightening. Here both the mean intensity with and without removing the local background are calculated. The lifetime is the time difference between the first and last appearance of a brightening with an accuracy of 20 s. This lifetime can be considered as an upper limit because it assumes that the brightening appears at the beginning of the first exposure and disappears at the end of last one. On the other hand, the lifetime of the brightenings existing already at the start or remaining at the end of the timeseries is underestimated. Considering that only

5% of the events are influenced and the longest-lived brightenings have a lifetime shorter than 5 min, this effect can hardly have a significant impact on the statistical results.

The shape of the brightenings is quantified as the ratio of length to width when the area reaches its maximum along the evolution. This is calculated by fitting the outline of a brightening with a 2-dimensional Gaussian function, and getting the ratio of the full width at half maximum (FWHM) at both directions, namely, the major and minor axes, as a proxy.

The velocity, representing an apparent POS motion of the brightening, is calculated using its initial and final spatial locations. Considering that the size, shape and brightness are changing during the evolution of the brightening, it is complex to find one representative point for a brightening. The positions of peak points, the centroid and intensity-weighted centroid are compared and statistically they are close enough to have negligible impact. The intensity-weighted centroid is selected to represent the location of the brightening to estimate the velocity, as it factors in both the extent and intensity.

4.4 Results

4.4.1 Visual detection results

Several properties of the 50 brightenings selected using the visual identification method described above are investigated, including intensity, lifetime, area, shape, and velocity. The distributions are shown in Figure 4.6. The panel (a) indicates that the mean intensities of brightenings show different peaks in different plumes. However, as seen in panel (b), they merge closer when the local background is removed. This suggests that although brightenings in bright plumes have higher intensities than those in faint plumes, the difference is mainly caused by the overall brightnesses of the plumes.

Most of the brightenings are transient and small-scale, as shown in Figure 4.6 (c) and (d). They mostly have a lifetime of less than 5 min. The short-lived ones have a lifetime of 60 s. Note that the method applied here only ensures to spot brightenings appearing in several images consecutively. The

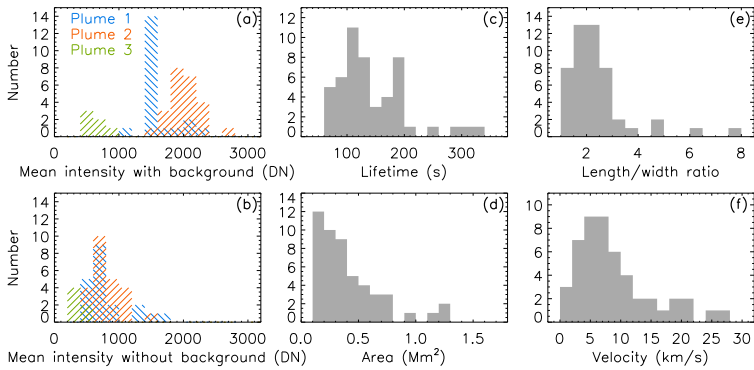


Figure 4.6: Distributions of the properties of the brightenings selected with the visual identification method (50 brightenings). (a) shows the mean intensity of the brightenings without subtracting the local background while (b) shows the mean intensity with the local background removed. (c)–(f) show the lifetime, area, ratio of length to width and velocity. The velocity here is a projection on the POS and is calculated using the first and last positions of the intensity-weighted center of the brightening.

area of the studied brightenings varies from 0.05 to 1.3 Mm². These values are based on the threshold used to demarcate the brightenings' boundaries. The distribution of the length/width (Figure 4.6 (e)) shows a clear peak at around 2 and can go up to 8. This means most brightenings exhibit a slightly elongated elliptical morphology while a minority exhibit significant elongation, forming a plumelet-like structure at low altitudes.

Figure 4.6 (f) shows the distribution of the velocity. About 70% of brightenings have a velocity component in the POS of less than 10 km s⁻¹. The velocity histogram peaks at around 6 km s⁻¹. A close examination of the trajectories of these structures reveals that their movements are more complex than simply unidirectional motion along the plume threads. Typically, the brightenings appear close to the footpoint and move outward, away from the base region. While some of the structures move in alignment with the plume (i.e., from north to south in plumes 1 and 2), some deviate from this direction. Considering a funnel structure of an open magnetic flux tube, in which the magnetic field lines starting from a concentrated region in the photosphere expand nearly horizontally in the chromosphere and transition region, forming a canopy, before they become more vertical again on the way to the corona (Solanki and Steiner 1990; Schrijver and Title 2003). There could also be small-scale loops in the neighborhood in addition to these open field lines. In such a geometry, depending on which field line the brightening is moving along and at which height, it can show different apparent movements in POS. Furthermore, both the intensity of the brightenings and the directions of their motion can change throughout their evolution owing to the variations in photospheric magnetic field on short timescales of less than 5 minutes (e.g., Anusha et al. 2017; Chitta et al. 2023a).

4.4.2 Automatic detection results

Same properties are also studied for the brightenings captured by the automatic method. Figure 4.7 shows the comparison of the distributions of brightening properties obtained by visual identification and by the automatic method. Both methods produce similar results, that is, most of the studied brightenings are small-scale, transient and exhibit slightly elongated morphologies.

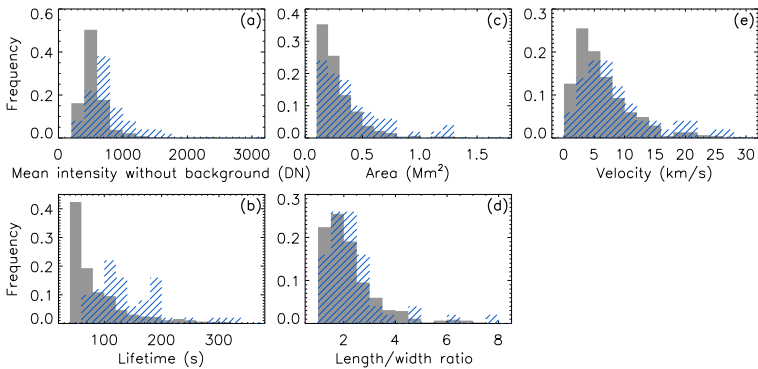


Figure 4.7: Normalized distributions of the properties (mean intensity, lifetime, area, ratio of length to width and velocity) of the brightenings detected with both visual identification method (50 brightenings) and automatic method (451 brightenings). The grey bars show the results from the automatic method and the blue line-filled bars show the results from the visual identification method.

Apart from the similarities, the automatically-detected brightenings show peaks at smaller intensity, area, lifetime and velocity. This means the automatic method is capable of picking up fainter, smaller and shorter-lived brightenings. These brightenings appear more often than the ones selected manually. Since the brightenings that only appear in one frame are neglected, the deduced lifetime cannot be shorter than 40s. More than 40% of the automatically identified brightenings possess this minimum lifetime. The distributions of length/width ratio show less difference as there is no preference in the shape of brightenings when they are selected by eye, but automatically detected ones still show a slightly higher rate of circular morphology.

Most brightenings move with a velocity of less than 10 km s^{-1} , irrespective of the detection method. Compared with the visual identification method, the automatic method detects more brightenings (50%) moving with even lower velocity, of less than 5 km s^{-1} . For these, the distribution peaks at $3\text{--}5 \text{ km s}^{-1}$. Note that, as only the first and last positions of each brightening are used to get an average velocity, the small velocities could be caused not only by the slow

Table 4.1: Automatically detected brightenings categorized according to directions (velocities are in units of km s^{-1})

	Directional	Random-like walk	Undefined*
Number of Brightenings	38	222	191
Mean POS Velocity	9.6	6.2	6.1
Most frequent Pos Velocity	7, 13**	3	3

* Brightenings appearing in only 2 frames have undefined directions

** Distribution of this group shows 2 peaks

motion, but also by brightenings moving in variable directions. All 451 brightenings are categorized according to their directions of motion. Excluding the 191 short-lived brightenings that appear in only two frames, for which a variation in the direction of motion cannot be defined, only 38 of the remaining ones have a relatively fixed direction of motion, i.e., the difference of their directions in two successive time intervals is always not less or equal to ± 30 degrees. These events also exhibit relatively greater speed (see Table 4.1). Two peaks are found in their velocity distribution at 7 km s^{-1} and 13 km s^{-1} . Meanwhile, the remaining 222 brightenings show a more random-like motion.

4.4.3 Brightenings and PDs

The velocities of brightenings are very small compared with the velocities of PDs within plumes. Previous studies suggest that the apparent outward speeds range from several tens to 300 km s^{-1} . A similar velocity can be detected in this work as well. Figure 4.8 shows a long slit starting from the base region and following one of the bright threads in the plume, which is used to make a time-slice plot (see Figure 4.8 (b)). The position of this slit is shown in Figure 4.8 (a). In this time-slice plot, one can clearly see the recurring brightenings at the footpoint and the PDs following up. Some of them that are easy to distinguish from the background are marked with the straight dashed lines.

To calculate the velocities, the light curves with an original time cadence of 5 s (and without spatial running average applied) of each PD at different distances along the slit are fitted by Gaussian functions. Figure 4.8 (c) shows

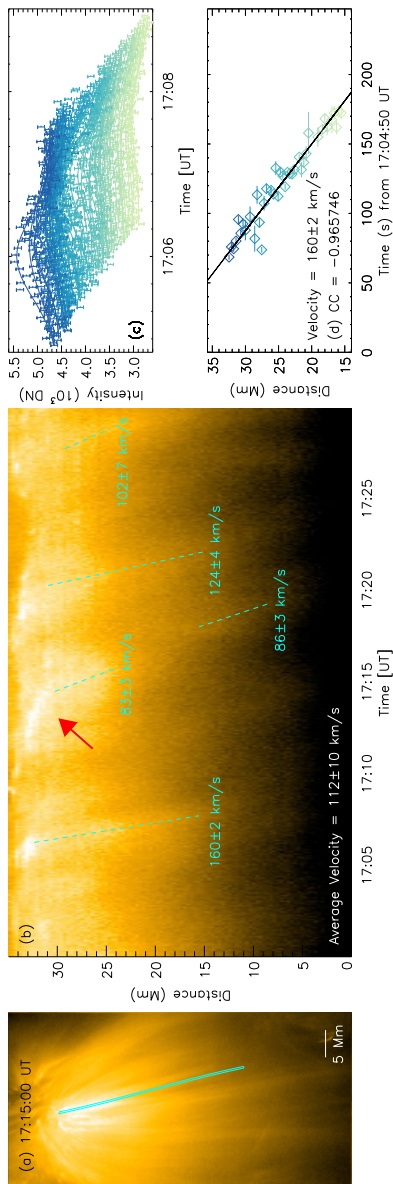


Figure 4.8: (a) HRI_{EUV} image of plume 2 showing the base region and plume streams. The overlotted box shows the position of the slice that is taken to form the timeslice plot shown in (b). (b) Timeslice plot. The PDs are marked with blue dashed lines. The average velocity is $112 \pm 10 \text{ km/s}$. The red arrow points to one of the PDs, which is potentially transformed by a slow-moving brightening. As an example, (c) shows the light curves at different distances (see different colors) of the first PD. The light curves are fitted with a Gaussian function. The central time (where the light curve peaks) derived from the fitting can be found in (d), together with the linear fitting of distances vs central time. The error of intensity in (c) is calculated taking the readout noise and dark current into account. This error is propagated to get the error of central time in (d).

the light curves of the first PD, with different colors indicating different distances. The error bars come from the readout noise and dark current (see equation S1 in Chitta et al. (2023b)). In this dataset, the exposure time is 2.8 s and the photons to DN conversion factor is 7.29 DN photon⁻¹. The temporal positions of the PD where its light curve peaks derived from the fitting are then fitted linearly to the distance (Figure 4.8 (d)). The speeds are distributed over a wide range, from 80 to 160 km s⁻¹. The slow ones have a similar velocity as reported in Gabriel et al. (2003, 2005), while none of the PDs detected here have a velocity as small as the 25 km s⁻¹ reported by Fu et al. (2014). The LOS Doppler velocities at a height of about 20–40 Mm have been found to be 30–60 km s⁻¹ (Hassler et al. 1997; Banerjee et al. 2000; Teriaca et al. 2003; Wilhelm 2006; Banerjee et al. 2009). For comparison, outflow velocity of PDs and small jets as measured in Pucci et al. (2014); Kumar et al. (2022); Chitta et al. (2023b) is in the range of a few 10 km s⁻¹ to a few 100 km s⁻¹.

In one case, a brightening is found at the plume base propagating at a speed of about 10 km s⁻¹, potentially transitioning to a PD moving with a higher speed of about 80 km s⁻¹ (see the arrow in Figure 4.8 (b)). This could be possible evidence that the base brightenings and PDs at greater heights are intrinsically related, but one such overlap may also occur purely by chance. Also, their velocities are very different. However, as the velocities measured here are components on the POS, the comparison of the real velocities of the moving brightenings and PDs should take projection effects into consideration.

4.5 Velocity correction

Based on the analysis on velocities, to assess the connection between the base brightenings and PDs at higher altitudes, it is important to understand the apparent acceleration from a velocity of less than 30 km s⁻¹ of brightenings to more than 100 km s⁻¹ of PDs. Since the coronal hole is adjacent to active regions, it is expected that the strong magnetic field from the active regions would expand and influence the open fields, especially at a relatively high altitude. This could imply that while the open magnetic field remains nearly radial (vertical) at the lower altitudes corresponding to the height of the base region brightenings, it is

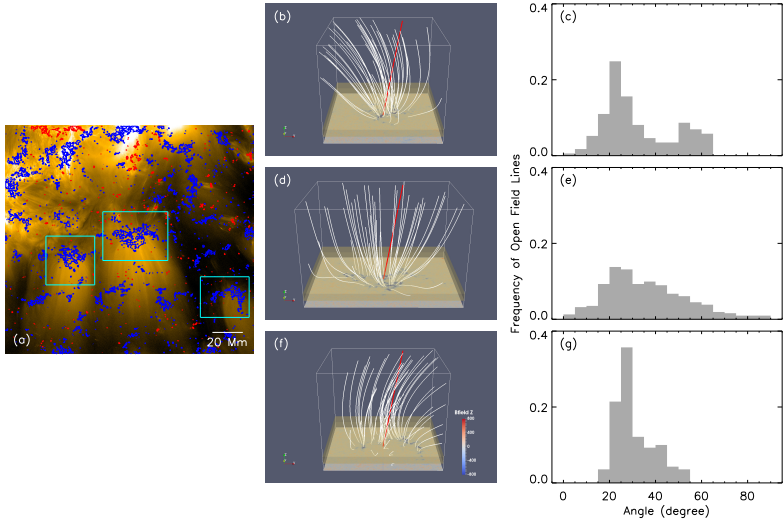


Figure 4.9: Magnetic field imprints of the plumes. (a) FOV covered by both HRI_{EUV} and HRT data. The background image comes from the HRI_{EUV} at 17:00 UT. The red (blue) contours of LOS magnetic field with the level of positive (negative) 50 Gauss are overplotted. (b), (d) and (f) show the extrapolated magnetic field lines at the location of the three plumes, the subregions marked with boxes in (a). (c), (e) and (g) are histograms of frequency of the separation angle between the local magnetic field vector and LOS of three plumes. This separation angle is obtained as average over all pixels at heights between 2000 and 4000 km along each field line; see the yellow boxes in (b), (d) and (f).

more horizontal at the higher altitudes supporting the PDs. The bending of magnetic field lines can cause the illusion of acceleration because only the velocity component in the POS can be captured in images. As mentioned before, not all brightenings move in a fixed direction. Since the brightenings with random-walk-like motions are possibly related to field lines that are closed or nearly horizontal before turning outward, I here focus on the brightenings that appear to move following the same plume threads as PDs. The aim is to de-project the observed speeds of brightenings to determine their true velocities and assess whether these velocities align more closely with the speeds of PDs.

An extrapolation of magnetic field is helpful to understand the 3-dimensional morphology of the magnetic field and to de-project the velocity component to the real velocity, assuming that the brightenings move along the magnetic field lines. Applied here are the vector magnetic data in the solar photosphere provided by HRT, part of SO/PHI. The data were taken at 16:30 UT, 30 mins earlier than the EUV observation with a high spatial resolution of about 200 km. In this dataset, HRT has a smaller FOV than HRI_{EUV} and is offset to the southeast.

After aligning HRI_{EUV} and HRT data, the region covered in both of them is shown in Figure 4.9 (a). The background image comes from the HRI_{EUV} at 17:00 UT and the contours of the LOS magnetic field with the level of 50 Gauss are overplotted. It is clear that the roots of all plumes are closely related to magnetic concentrations spanning about 30 Mm. The ambiguity in the transverse field's component of the SO/PHI-HRT vector magnetogram has been removed using an adapted version of HMI disambiguation pipeline (Hoeksema et al. 2014; Metcalf et al. 2006) that implements the minimal-energy disambiguation method ME0 (Metcalf 1994).

The radial magnetic field is calculated based on the disambiguated vector magnetic data using the transformation in Gary and Hagyard (1990). With the radial magnetic field as the bottom boundary, a potential extrapolation is made to the height of 256 pixels (25 Mm). Figure 4.9 (b), (d) and (f) separately show the field lines where the three plumes locate. The bottom slices are the magnetic field along Z axis, which is the local vertical direction on the Sun. The extrapolation indicates that the open field lines related to the plume grow and expand to form a funnel structure, in agreement with both observations and

previous simulations. The red lines in boxes represent the direction towards Solar Orbiter.

Here, all field lines reaching the top boundary are regarded as open field lines. For each open field line, the angle between the magnetic field vector and LOS direction at different heights can be calculated. Figure 4.9 (c), (e) and (g) show the distribution of the separation angle of each field line averaged over all positions between 2000 and 4000 km. It has been suggested by Berghmans et al. (2021) that small-scale brightenings in the quiet sun observed by HRI_{EUV} occur at heights around 2000–4000 km, although the brightenings at the plume base need not necessarily form at the same height as quiet sun brightenings. Depending on the morphology of each plume, the distributions peak at different angles, from 20 to 30 degrees. This implies that, the velocity can be enlarged by a factor of 3, at most, in the de-projection. This is not enough to explain the difference between velocities of brightenings and PDs. Although the fastest ones (with a velocity of 30 km s^{-1}) could move at a speed almost reaching the high velocity of PDs, most brightenings have a 3-dimensional velocity of less than 30 km s^{-1} . In other words, instead of an illusion caused by perspectives, the difference between these velocities is real.

However, the same angle cannot be used for the correction of velocities detected at greater heights. Due to the limitation of HRT FOV, the adjacent active regions are not covered in this data. As mentioned before, the magnetic field from the active regions could push open field lines either towards them or away from them, depending on the magnetic polarity. This effect is missing in the potential extrapolation with HRT data.

To demonstrate this effect, another extrapolation test is done with data from HMI. This experiment is done for the purpose of proving the effect of the strong magnetic field from the active regions on the directions of nearby open fields. The plumes studied in this work are located in the coronal hole close to active regions NOAA 13105 and NOAA 13107. Unfortunately, due to the separation angle between the Earth and Solar Orbiter of more than 90 degrees, no simultaneous observation of these active regions from HMI is obtained. About one week later, the active regions and coronal hole have rotated to reach the disk center region of the sun in the FOV of HMI. However, a new active region NOAA 13127 has

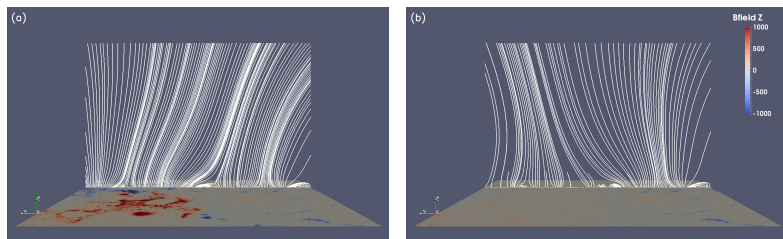


Figure 4.10: Potential extrapolations with the original HMI data and the processed data with the strong magnetic fields from the active regions removed. One cross-section parallel to the x - z plane is selected for demonstrating the directions of magnetic fields. The streamlines show the magnetic field lines projected on this plane.

emerged during this time very closely to where the plumes were located. To avoid the influence of the newly emerged active region, the HMI sharp_cea data at 09:00 UT on 28 September 2022 is selected. This dataset captures NOAA 13105 and NOAA 13107 in the previous rotation when they appear in the western hemisphere in HMI FOV as the Sun rotates. Despite that the active regions are stronger and the plumes in this study have not been produced at this point, this dataset could be simply used to study the effect of active regions qualitatively.

For comparison, two extrapolations are performed. One uses the original data as the bottom boundary and another uses the processed data with the strong magnetic fields (B_r above 100 Gauss) from the active regions removed. No changes are made to the quiet sun and coronal hole regions and some small magnetic concentrations in active regions are left for flux balance. The results can be found in Figure 4.10, where the same cross-section parallel to the X - Z plane is shown in both extrapolations. The streamlines show the projection of the magnetic field lines on this plane. What can be found here is that, compared with panel (b) where there is no active regions, the streamlines on the left side of the plane in panel (a) clearly show a stronger inclination under the effect of active regions.

It proves that the active regions could influence the open field lines in the

vicinity, although it is hard to quantify this effect. In summary, this experiment suggests that the angle between the direction of the PDs and LOS is likely to be greater than that of the brightenings. That is, part of the difference between apparent speed of PDs and brightenings could come from the projection effect.

4.6 Discussion

4.6.1 Link between base brightenings and PDs

4.6.1.1 Are PDs mass flows or waves?

I would like to open the discussion by examining the physical nature of PDs, which are better understood than base brightenings and help to further investigate the potential link between the two, thereby contributing to a deeper understanding of base brightenings. In both coronal loops and plumes, PDs are widely interpreted as mass flows or waves. Previous studies suggested the existence of slow-mode waves in plumes (e.g., DeForest and Gurman 1998; Krishna Prasad et al. 2012). Such slow mode waves have been invoked to be potential contributors to coronal heating (DeForest and Gurman 1998; De Moortel et al. 2000; McEwan and de Moortel 2006). The wave interpretation is first verified using temporal variations of the intensity along plumes in these observations. To this end, I select one of the distinct PDs (see Figure 4.11 (a)) and select equally-spaced points along this PD at different distances from the base region (see diamonds in Figure 4.11 (a)). At each point, a slit is placed perpendicular to the PD, and a Gaussian function is fitted to the intensities along the slit. Figure 4.11 (b) presents the amplitudes of the fitted Gaussian functions as a function of distance. A similar variation in intensity, initially increasing with height and then decaying, can be observed in other PDs as well.

This helps to characterize the nature of the PD. If the plumes are in hydrostatic equilibrium, their EUV emission is expected to fall off exponentially with certain scale-height set by the pressure at their base. For the PDs shown here, the EUV emission first increases up to several megameters above the base and then decreases. Moreover, the peak position of the intensity shifts outward with time (see the variations of intensity with distance at three instances separated

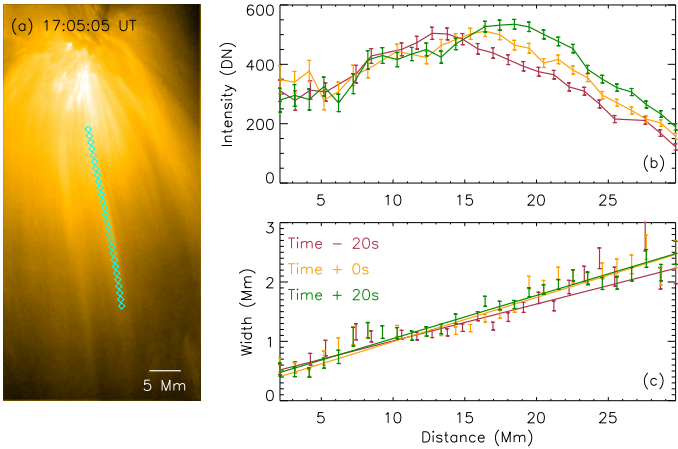


Figure 4.11: Propagating disturbances. (a) HRI_{EUV} image of plume 2. Positions at different distances from the base region are marked with diamonds. The intensities along the slits perpendicular to the stream direction at these positions are fitted by a Gaussian function. (b) and (c) show the peak and FWHM of the fitted Gaussian functions, as a function of the distance along the PD, at three instances (each separated by 20s; as identified with different colors). Same as Figure 4.8 (c) and (d), the error of intensity in (b) comes from the detector readout noise and dark current and the error of width is derived from the Gaussian fitting.

by 20 s). Both these factors are inconsistent with plumes being in a hydrostatic equilibrium. These factors can only be reconciled with additional heating along the plume away from the base region or excess plasma cooling from higher temperatures. But because the PDs are found to propagate outward rather than flow downwards as typically expected in the case of plasma cooling, I suggest that these observations are consistent with a scenario of injection of material at the base of plumes. Note that, this intensity variation could also be explained by a temperature gradient along the direction of the PDs. However, This cannot be confirmed in the present study and has not been reported in previous data (Wilhelm et al. 2011).

Additionally, this analysis reveals PDs exhibiting speeds varying from 80–160 km s⁻¹. Only the largest speed among them can reach the local acoustic speed $c_s \approx 150 \text{ km s}^{-1}$ at the coronal temperature $T = 10^6 \text{ K}$. Note that, because of the projection effects the apparent velocities are only a lower limit of real velocities. In an optically-thin atmosphere, it is possible that multiple PDs with similar velocities close to the local sound speed but different inclinations over the POS could overlap along the LOS, giving the impression that different PDs have different speeds. However, considering that the slowest PDs among these samples travel at 80 km s⁻¹, i.e., half the sound speed, it would require a separation angle from the POS of about 60° to reach the typical velocity of a slow mode. Thus, the slow-mode waves could explain the propagation only when the angles between the propagating directions of different PDs are relatively large. In summary, these results are more in favor of the PDs being high speed mass flows than waves (see also Chitta et al. 2023b).

4.6.1.2 Mass conservation: Evolution of base brightenings into PDs

Assuming that the PDs are mass flows, the possibility is explored that the base brightenings are also mass flows in their initial stage and will eventually evolve into PDs. The trajectories and velocity distributions of these transient structures in the base regions show that there are some brightenings, although only a small fraction (less than 10%), that have a relatively fixed moving direction with a detectable velocity, which conforms to the motion of outflows. Their velocity

distribution peaks at around 7 and 13 km s^{-1} , corresponding with the outflow velocity in coronal holes based on the Doppler shifts of transition region Ne VIII emission line (Hassler et al. 1999). The existence of elongated brightenings also proves that some of them are jet-like structures. However, these "outflows" close to the base region do not share the same order of magnitude of velocity of plume flows detected at higher altitude. Despite previous works stating that "jetlets" (mass flows at the plume base) could move outwards to form plumelets, in this work, it is difficult to reconcile the possibility that the base brightenings are the same evolving structures as plume outflows.

If the base brightenings evolve outwards to become plume outflows, they should have a nearly constant outward mass flow rate given by $\dot{m} = v m_e n_e A$, at different heights, where v is the outflow velocity, m_e and n_e are the electron mass and number density, and A is the cross-section area of the outflow. The following paragraph presents an estimation of the changes of the velocity, the cross-section area and the number density.

This work suggests that one could conservatively consider an increase in velocity (from about 30 km s^{-1} to 100 km s^{-1}) of a factor of 3. To estimate the expansion rate, the change in the width of the same PD selected in Figure 4.11 (a) is analyzed. Figure 4.11 (c) shows the FWHM of the fitted Gaussian functions against the distance. The expansion factor at a very low altitude is hard to be measured directly from the observation, for that the base region is too bright and dynamic to resolve plume streams. In the higher corona, where the filamentary PD substructures can be observed, these streams widen linearly with distance and the stream width can increase by at least a factor of 3 at the distance of 20 Mm relative to the base region, which gives an expansion factor of 9. To compensate the increase of the velocity and the cross-section area, a decrease in density of a factor of 27 seems to be necessary in the PD to satisfy a constant mass rate. This disagrees with the observations here as the EUV emission, which depends on n_e^2 under a constant temperature assumption, does not show such a huge difference in the base region and plumelets. It is important to mention that the expansion rate can only be regarded as a rough estimation. In reality, most streams have diffused edges that can hardly be measured precisely. However, even with a negligible expansion, the base regions cannot be 3 times denser than

plumes at 20–40 Mm, which is consistent with results about plume density in the literature, as discussed below.

Different methods have been applied over the years to measure the plume density. A summary of the results of such investigations can be found in Table 3 and Figure 17 of Wilhelm et al. (2011). The results are variable with large error bars. For instance, Fludra et al. (1999) studied polar plumes and found that the density decreases with height from $2 \times 10^8 \text{ cm}^{-3}$ at the limb to $6 \times 10^7 \text{ cm}^{-3}$ at $1.1 R_{\odot}$. Young et al. (1999) derived densities of $2.5\text{--}5.6 \times 10^9 \text{ cm}^{-3}$ at the bright base region and of $3.8\text{--}9.5 \times 10^8 \text{ cm}^{-3}$ above the limb at coronal temperature. Considering the power law fits, in both plume and interplume regions, n_e is found to be proportional to $(R_{\odot}/R)^8$ below $R=2R_{\odot}$ (Wilhelm et al. 2011). This empirically provides that the density at the plume bases is approximately 1.3 times the density at the height of 20–40 Mm. Though different densities are found in different cases, they do not seem to meet with the possibility of mass flux conservation.

4.6.2 Decoding base brightenings

4.6.2.1 Hypothesis I: Reconnection

One possible explanation of these brightenings is related to magnetic reconnection. Kumar et al. (2022) selected one of the large base jets and applied a potential-field extrapolation from an HMI magnetogram to study the magnetic topology of this region. They revealed that a fan-spine structure is involved in producing the brightening and outflow. Cho et al. (2023) showed evidence of associated brightenings and blueshifted plasma (outflows) in the region with opposite magnetic polarities and found a high temperature structure at the base of the plume. Both works support the picture of interchange reconnection between open field lines and closed loops, leading to localized rapid enhancement and ejection of materials.

However, previous studies have not discussed in detail the movement of these EUV brightenings at the base of the plume. It is possible that this is limited by the resolution of previous EUV imaging observations, so that the movement of these very small brightenings was not easily captured. One possibility that could

account for the observed motions is that the frequent, repetitive and impulsive reconnections take place and result in discrete brightenings flashing successively over a short period of time in a small region, creating the appearance of movement. Alternatively, the movement may arise from the actual evolution of brightenings. For example, the plasma flowing along the newly-formed closed loop hits the footpoints of the loop, causing the evaporation of the chromospheric material to fill in the whole loop. In this work, it is hard to corroborate whether or not magnetic reconnection has occurred. More magnetic field data are required to study the evolution of the photospheric magnetic field below the plumes. This hypothesis about reconnection depends on how mixed the magnetic polarities are, whose observation depends on the instrument's sensitivity and resolution.

4.6.2.2 Hypothesis II: Wave-driven Type I spicules

Jet-like structures, such as spicules, have been found to dominate the dynamic upper chromosphere. Some observational similarities can be found between base brightenings and type I spicules. Both show complex motions and have comparable velocities and both appear to be periodic and related to chromospheric network concentrations. It is worth mentioning here that the base brightenings do not show the back-and-forth motions typical of type I spicules and dynamic fibrils. Also, the base brightenings discussed here are less elongated and have a shorter lifetime than chromospheric Type I spicules.

This can also help to understand the formation of base brightenings. The type I spicules are believed to be potentially triggered by shock waves that are powered by p-modes (e.g., De Pontieu et al. 2004). This omnipresent p-mode oscillation, as also reported in Kumar et al. (2022), can be the cause of base brightenings as well. However, in corona holes, where the magnetic field is more vertical, the leakage of p-modes is more difficult due to a shorter acoustic cut-off period, forming less-elongated and shorter-lived structures, like the base brightenings observed in this study.

Meanwhile, the velocities of the PDs are closer to those of type II spicules. Both of them are outwardly oriented and fade out after a certain distance. It is reported by Cho et al. (2023) that they may have matching periodicities, suggesting a close link between them.

4.7 Conclusion

This study investigates in detail the small-scale dynamic brightenings in the base regions of three coronal hole plumes with the observation from HRI_{EUUV}. Here the main results are: 1) The majority of the observed brightenings at the base of plumes can be characterized by their small-scale nature (covering an area of less than 1.3 Mm^2), transient behavior (with a lifespan of less than 5 minutes), and display of slightly elongated morphologies. 2) The intensities of brightenings from different plumes are identical once the plume background is subtracted. 3) Brightenings show complex movements. Most of the brightenings appear to move with a velocity component in the POS of less than 10 km s^{-1} . After de-projecting the POS velocities to 3-dimensional velocity using an extrapolation with SO/PHI data, the velocities of brightenings are still much smaller than those of the PDs.

The potential explanations for base brightenings are now considered by first investigating their link to PDs, based on the two possible physical natures of PDs, slow waves and mass flows. Assuming the constant temperature along the plume, the results are more in favor of PDs being mass flows than slow waves. In that case, the mass conservation estimation does not support the base brightenings being the initial outflows that can evolve into high-speed PDs. Given the assumptions as well as the estimation errors involved, it is difficult to conclusively rule out the possibility that base brightenings and PDs are directly linked. But in the absence of such a connection, determining the nature of base brightenings based on an understanding of PDs remains challenging. Therefore, two hypotheses are proposed on the nature of base brightenings: (i) they are associated with wave-driven Type I spicules or (ii) they are produced by interchange reconnection. This study can provide very limited constraints on both hypotheses, highlighting the need for further detailed investigation. Considering the small size and short duration of these structures, observations with high spatial and temporal resolution are necessary and longer continuous observations could also be helpful in studying the slow-mode wave scenario in plumes. One could also take advantage of simultaneous observations from multi-instruments, i.e., photospheric magnetic fields data and spectral data, which provide information in different layers in the

solar atmosphere. This work shows that magnetic field data can assist in correcting the observed POS velocities. In addition, Doppler velocities derived from spectral data can also provide the LOS velocity component. These are essential in understanding the mechanism of plumes and measuring the proportion of released energy that is carried by outflows to reach the upper atmosphere and eventually contribute to the solar wind.

Chapter 5

Conclusions and outlook

This thesis focuses on the investigations of the small-scale activities in the solar atmosphere using high-resolution observations from the instruments aboard Solar Orbiter. The primary goal is to contribute to answering two of the most significant open questions in solar physics, the coronal heating problem and the origins of the solar wind. The persistent high temperatures of the corona and the continuous, long-term outflows of the solar wind require ubiquitous and sustained mechanisms, such as wave dissipation or small-scale magnetic reconnection. From an observational perspective, it is crucial to identify and analyze signatures of these mechanisms, which could be subtle, but omnipresent. Solar Orbiter, with its advanced instrumentation and unique vantage points, offers an unprecedented view of the Sun to explore these small-scale phenomena. This thesis primarily focuses on two regions of the Sun: the quiet sun and coronal holes. Despite their distinct magnetic field structures, both regions reveal an abundance of small-scale events in EUV observations from Solar Orbiter.

The EUV brightenings in the quiet sun have been statistically studied by Berghmans et al. (2021). They are reported to be small-scale, short-lived and happen frequently. Their correlation with chromospheric network and magnetic cancellation could support the nanoflare heating model. To explore their contribution to the coronal heating, another factor of these EUV brightenings, their

temperature, is studied here by combining spectroscopic data from SPICE and EUV imaging data from EUI for the first time.

Three EUI brightenings are captured by both HRI_{EUV} and SPICE in two data sets. Their scales almost reach the edge of the SPICE resolution, which makes the assistance of HRI_{EUV} images in identifying these brightenings necessary. SPICE, on the other hand, provides multi-thermal information once the locations of the brightenings are determined. The results show that, one of the EUI brightenings (E-1) is only detectable in an O VI line (0.3 MK) while the others (E-2 and E-3), which exist for a longer time (several minutes) leave signatures in transition region lines and a Ne VIII line (0.6 MK), which is believed to be formed from upper transition region to the low corona.

No hotter line is available in these data sets, resulting in a lack of direct evidence to determine whether these EUI brightenings have been heated to a higher temperature. However, the study of E-3 provides a proof of its thermal evolution. In transition region lines (C III and O VI), their light curves display two peaks, which could possibly correspond to the time when E-3 is heated up and cools back to these temperatures. Differently, Ne VIII has only one peak in its light curve, which could indicate that the highest temperature that E-3 reaches is not high enough, compared with the Ne VIII temperature to clearly show discrete heating and cooling peaks. All these findings lead to the conclusion that these EUI brightenings likely remain at the lower-coronal temperatures before cooling down.

Having examined small-scale events in the quiet sun, attention then turned to coronal holes, where plumes are commonly observed and are proposed to channel the MHD waves and the solar wind into the heliosphere. There are two phenomena usually reported in the coronal hole plumes, the high-speed propagating disturbances (PDs) and the base transients. The former ones have been well detected in previous studies but their physical nature is still under debate (waves vs mass flows). Although the latter ones have also been reported, many details about them were not recovered using instruments prior to the advent of EUI.

Within three coronal hole plumes, hundreds of base brightenings are identified, characterized by their small scale, short duration and slightly elongated

morphology. More intriguingly, most of the base brightenings show a small apparent speed in the POS of less than 10 km s^{-1} . These velocities are still much smaller than the PDs ($80\text{--}160 \text{ km s}^{-1}$) even after accounting for projection effects.

Potential explanations for base brightenings and their connection to PDs are explored. Assuming a constant plume temperature, the findings here favor PDs as mass flows over slow waves. However, mass conservation estimates do not support base brightenings as the initial outflows leading to high-speed PDs. While it is difficult to definitively rule out a direct link between base brightenings and PDs, here two hypotheses are proposed: base brightenings may be tied to wave-driven Type I spicules or interchange reconnection.

Although this thesis has provided some significant insights on small-scale events in both quiet sun and coronal holes, limitations remain and highlight opportunities for further explorations. As mentioned before, both the coronal heating and the solar wind origin problems require a persistent and steady energy input. It is then crucial to consider how to expand and generalize the results presented in this thesis.

Only three events were identified in the study of brightening structures in the quiet sun. This limitation primarily arises from the restricted availability of data, particularly from SPICE. To obtain more spectral data from SPICE for small-scale structures, longer duration SPICE observations that overlap with HRI_{EUV} would be beneficial. In the data set applied here, the simultaneous observations are only a few minutes to around ten minutes long. With Solar Orbiter now being in its nominal phase, it is possible to capture more events through longer observations. Additionally, given that the data alignment method in this study relies on time-slice plots, extending the overlapping duration would also help to minimize the alignment errors, further improving the reliability of the analysis.

It has also been found that some of these events exist only for less than 1 minute. Therefore, the observation mode of SPICE also needs to be carefully selected according to the requirements, as different observing modes result in different cadences. A context image can cover a large area and thus provide the opportunity of capturing more events. However, it sacrifices the temporal resolution and is not suitable for the studies of individual events. The sit-and-

stare mode, on the other hand, has higher time cadence by fixing the position of the slit. Also note that, some of the brightenings are not very bright in weak lines and to accumulate enough photons for a higher SNR, the exposure time should also be taken into consideration. There are other limitations of SPICE data in diagnosing the temperatures of the brightening structures. An important one is the lack of the bright hotter lines. Also, the spectral resolution of SPICE is not good enough to extract information from the analysis of the spectral profiles.

For the base brightenings in coronal hole plumes, although a statistical analysis is conducted here, all the brightenings come from the plumes within a single coronal hole. It is then necessary to consider whether the same results apply to plumes and even interplume regions in other coronal holes. Therefore, high-resolution data covering other coronal holes, including polar coronal holes, would be very helpful. Chitta et al. (2024)¹ investigated the same data set, recorded on 13 October 2022, analyzed in this thesis, together with a data set recorded on 17 April 2023, focusing on the intermittent jets in the interplume regions. Figure 5.1 shows that these picoflare jets are prevalent in the interplume region. Just like the PDs in the plume, they exhibit speeds on the order of $100\text{--}150\text{ km s}^{-1}$ in the POS.

What is also missing in this work is the precise 3-dimensional measurement of the velocities. To achieve this, stereoscopic observations, that is, observing the same structure from multiple perspectives, should be considered. However, given the small-scale nature of the brightenings and the optically thin environment, accurately identifying the same structures across different observations is not an easy task. Another approach is to use spectral data to get the Doppler velocity along the LOS ($V_{los}=c\Delta\lambda/\lambda_0$) by measuring the line center shift or enhancements in the line wings. Combining the LOS velocity with the POS velocities derived from imaging observations enables a more precise reconstruction of the 3-dimensional velocity.

Both studies presented in this thesis emphasize the importance of spectroscopic data. Table 5.1 summarizes some of the spectroscopic instruments apart from SPICE (for more details see Section 2.1.2), from the retired SUMER, to

¹I contributed to Chitta et al. (2024) by identifying and measuring the velocities of the picoflare jets, e.g., Figure 5.1.

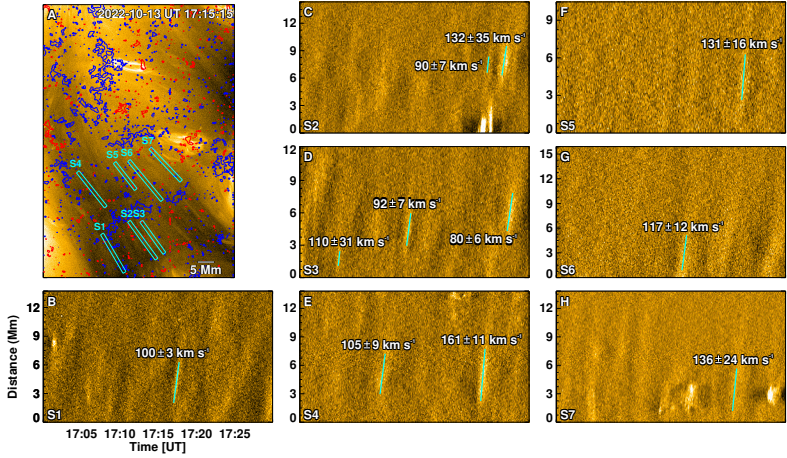


Figure 5.1: Picoflare jets in the interplume region, observed in HRI_{EUV} images. The same dataset is also used for studying the plumes in this coronal hole, as shown in Chapter 4. (A) HRI_{EUV} image of the coronal hole interplume region. Overplotted are contours showing magnetic field measured by SO/PHI-HRT. Slits S1-S7 marked in cyan boxes are selected to get time-slice plots shown in panels (B)–(H). Some jets are identified with cyan lines and their speeds are measured. Image credit: Chitta et al. (2024), reproduced under a CC BY 4.0 license.

the currently operating IRIS and EIS, and to the upcoming EUVST and MUSE. Spectroscopic instruments provide detailed spectra, which capture the intensity of light as a function of wavelength, offering insights into plasma properties like temperature, density, and velocity. This thesis also includes an error analysis of SPICE data. Considering the similarities shared by the designs of EUVST and SPICE, the same error estimation method could also be adjusted for the EUVST data in the future.

The small-scale nature of these brightenings demands high spatial resolution from both imagers and spectrometers. HRI_{EUV} has very high spatial resolution, especially near Solar Orbiter's perihelia. In contrast, SPICE's resolution is less suited for detecting EUV brightenings, highlighting the importance of combining its data with HRI_{EUV} observations. Among current spectroscopic instruments, the spatial resolution of IRIS can go down to $0.33''$ (~ 240 km), high enough to resolve the details of some EUV brightenings. The future missions EUVST and MUSE are also planned to provide high-resolution data ($0.4''$ for EUVST and less than $0.5''$ for MUSE). In addition, the multi-slit design of MUSE uses 37 simultaneous slits, enabling a spectroscopic raster with large FOV and unprecedented temporal resolution.

A broad temperature coverage is also crucial for understanding the plasma's thermal structure and provides valuable information for estimating the height distribution. Especially, observations in hotter (at coronal temperatures) lines are important for understanding the contribution of the target events to coronal heating. The SPICE lines are listed in Table 2.2. IRIS mainly focus on the chromosphere and transition region, while SUMER observes lines emitted from the upper chromosphere to the lower corona, as well as the forbidden lines from the flaring corona. Although SUMER had a wider wavelength range, for lines below 500\AA the sensitivity got very low. EIS covers hotter lines from upper transition region to the flaring corona. In the future, MUSE will focus on highly-ionized iron lines. Designed with a very wide wavelength range, EUVST is intended to simultaneously observe different temperatures throughout the solar atmosphere, from the chromosphere to the corona. It is possible that, MUSE and EUVST will provide simultaneous observations covering the same region of the Sun to achieve a large FOV, high spatial and temporal resolutions, along with a wide

Table 5.1: Overview of some key spectroscopic instruments

Instruments	mission	Status	Data products	Spatial resolution	Wavelength range (Å)
SUMER	SOHO	launched 1995 ended 2014	spectra raster images	2''	500–1600
EIS	Hinode	launched 2006 operating	spectra raster/slot images	2''	170–210 250–290
IRIS	IRIS	launched 2013 operating	spectra raster/slit-jaw images	0.33''	FUV 1332–1358 NUV 2783–2835
EUVST	Solar-C	plan to be launched 2027	spectra raster/slit-jaw images	0.4''	SW 170–215 LW 690–850 925–1085 (2 nd 463–542) 1115–1275 (2 nd 557–637)
Multi-slit EUV spectrograph	MUSE	plan to be launched 2027	multi-slit spectra high-cadence raster images	≤0.5''	171, 284, 108

coverage of temperatures.

In addition, activity in the solar atmosphere is often associated with magnetic field variations that also show up in magnetic field footpoints. This makes the photospheric magnetic field data from instruments such as PHI, HMI, and DKIST very important for investigating the physical mechanisms that give rise to these structures. In-situ instruments, including those onboard Solar Orbiter, PSP, and ACE, can provide the changes of the properties of the plasma that travel through them, helpful for studying the relationship between solar activity and space weather, including the origin of the solar wind.

These forthcoming instruments such as EUVST and MUSE will provide advanced capabilities to enhance our understanding of the small-scale brightenings and jets. For example, the thermal structures of the EUV brightenings can be analyzed in much greater detail using observations of higher spatial, temporal and spectral resolution from these new spectrographs, which also capture hotter, coronal spectral lines. This is crucial for determining whether these brightenings truly reach coronal temperatures and contribute to coronal heating. In addition, the faster scanning times of EUVST and, in particular, the multi-slit approach of MUSE will enable covering a much larger FOV at a cadence higher than the lifetime of most of these events. This will allow a significant increase in the number of studied events, which is essential to extrapolate general properties from the observation of individual events. More specifically, these observations allow for statistical analyses of the occurrence rates and energy release of EUV brightenings, helping to extend the energy distribution to smaller scales.

EUVST will provide spectroscopic data of coronal lines with higher spectral resolution than current instruments such as EIS and SPICE, allowing detailed studies of plasma flows along the LOS. On the other hand, imaging data, such as those from HRI_{EUV} are ideal to track motions in the POS. Thus, combining those spectroscopic observations with imaging data will allow determining the full plasma velocity vector at the base of the corona, leading to a better understanding of the mass transport throughout the corona and into the solar wind. In addition, comparing these velocities with the local acoustic and Alfvén speed could reveal the potential relation of jets to wave phenomena. Finally, high spectral resolution line profiles may allow to infer the underlying mechanisms driving

these jets. For instance, bi-directional flows observed in spectral lines can be regarded as signatures of magnetic reconnection.

To further investigate how these small jets propagate into the outer atmosphere, a connection could be established between remote-sensing observations and in-situ measurements, if the spacecraft crosses the region where jets are expected to propagate. Finally, magnetic field data help to understand the underlying magnetic mechanisms driving EUV brightenings and jets. For example, the small-scale magnetic footpoint evolution below the EUV brightenings can reveal localized magnetic activities, such as reconnection events associated with flux cancellations, that could trigger the brightenings. The magnetic structures can also be used to trace solar wind streams back to their source regions on the solar surface, with the assistance of magnetic extrapolations based on the photospheric magnetic field data.

In short, this thesis highlights the critical importance of high spatial, spectral and temporal resolution, multi-wavelength observations in uncovering the intricate processes governing the solar atmosphere. The advanced operating missions, such as Solar Orbiter, PSP, DKIST, along with future missions like EUVST and MUSE promise unprecedented opportunities to refine the understanding of small-scale events and how they are related to coronal heating and solar wind. These efforts will not only enhance the knowledge of solar physics but also improve the ability to predict space weather and its impacts on Earth.

Bibliography

- Abdelatif, T. E., Lites, B. W., & Thomas, J. H. The Interaction of Solar p-Modes with a Sunspot. I. Observations. *ApJ*, 311:1015, December 1986. doi: 10.1086/164838.
- Ahmad, I. A. & Webb, D. F. X-ray analysis of a polar plume. *Sol. Phys.*, 58(2): 323–336, July 1978. doi: 10.1007/BF00157278.
- Ahmad, I. A. & Withbroe, G. L. EUV analysis of polar plumes. *Sol. Phys.*, 53 (2):397–408, August 1977. doi: 10.1007/BF00160283.
- Amari, T., Aly, J. J., Luciani, J. F., Boulmezaoud, T. Z., & Mikic, Z. Reconstructing the Solar Coronal Magnetic Field as a Force-Free Magnetic Field. *Sol. Phys.*, 174(1-2):129–149, August 1997. doi: 10.1023/A:1004966830232.
- Amari, T., Luciani, J. F., Mikic, Z., & Linker, J. A Twisted Flux Rope Model for Coronal Mass Ejections and Two-Ribbon Flares. *ApJ*, 529(1):L49–L52, January 2000. doi: 10.1086/312444.
- Antiochos, S. K., Dahlburg, R. B., & Klimchuk, J. A. The Magnetic Field of Solar Prominences. *ApJ*, 420:L41, January 1994. doi: 10.1086/187158.
- Antonucci, E., Romoli, M., Andretta, V., et al. Metis: the Solar Orbiter visible light and ultraviolet coronal imager. *A&A*, 642:A10, October 2020. doi: 10.1051/0004-6361/201935338.
- Anusha, L. S., Solanki, S. K., Hirzberger, J., & Feller, A. Statistical evolution of quiet-Sun small-scale magnetic features using Sunrise observations. *A&A*, 598:A47, February 2017. doi: 10.1051/0004-6361/201527738.
- Aschwanden, M. J. An Evaluation of Coronal Heating Models for Active Regions Based on Yohkoh, SOHO, and TRACE Observations. *ApJ*, 560(2):1035–1044, October 2001. doi: 10.1086/323064.

BIBLIOGRAPHY

- Aschwanden, M. J. & Acton, L. W. Temperature Tomography of the Soft X-Ray Corona: Measurements of Electron Densities, Temperatures, and Differential Emission Measure Distributions above the Limb. *ApJ*, 550(1):475–492, March 2001. doi: 10.1086/319711.
- Aschwanden, M. J. & Parnell, C. E. Nanoflare Statistics from First Principles: Fractal Geometry and Temperature Synthesis. *ApJ*, 572(2):1048–1071, June 2002. doi: 10.1086/340385.
- Athay, G. R. & White, O. R. Chromospheric Oscillations Observed with OSO 8. II. Average Power Spectra for SI II. *ApJS*, 39:333–346, March 1979. doi: 10.1086/190574.
- Athay, R. G. & White, O. R. Chromospheric and coronal heating by sound waves. *ApJ*, 226:1135–1139, December 1978. doi: 10.1086/156690.
- Auffret, H. & Muller, R. Center-to-limb variation of the network bright points in the solar photosphere. *A&A*, 246(1):264–279, June 1991.
- Axford, W. I. & McKenzie, J. F. The origin of high speed solar wind streams. In Marsch, E. & Schwenn, R., editors, *Solar Wind Seven Colloquium*, pages 1–5, January 1992.
- Babcock, H. W. The Topology of the Sun's Magnetic Field and the 22-Year Cycle. *ApJ*, 133:572, March 1961. doi: 10.1086/147060.
- Babcock, H. W. & Babcock, H. D. The Sun's Magnetic Field, 1952-1954. *ApJ*, 121:349, March 1955. doi: 10.1086/145994.
- Bahng, J. & Schwarzschild, M. Lifetime of Solar Granules. *ApJ*, 134:312, September 1961. doi: 10.1086/147160.
- Balmforth, N. J. & Gough, D. O. Effluent Stellar Pulsation. *ApJ*, 362:256, October 1990. doi: 10.1086/169262.
- Banerjee, D. & Krishna Prasad, S. MHD Waves in Coronal Holes. *Geophysical Monograph Series*, 216:419–430, February 2016. doi: 10.1002/9781119055006.ch24.
- Banerjee, D., Teriaca, L., Doyle, J. G., & Wilhelm, K. Broadening of SI VIII lines observed in the solar polar coronal holes. *A&A*, 339:208–214, November 1998.
- Banerjee, D., Teriaca, L., Doyle, J. G., & Lemaire, P. Polar Plumes and Interplume regions as observed by SUMER on SOHO. *Sol. Phys.*, 194(1):43–58, May 2000. doi: 10.1023/A:1005253413687.

- Banerjee, D., Pérez-Suárez, D., & Doyle, J. G. Signatures of Alfvén waves in the polar coronal holes as seen by EIS/Hinode. *A&A*, 501(3):L15–L18, July 2009. doi: 10.1051/0004-6361/200912242.
- Banerjee, D., Krishna Prasad, S., Pant, V., et al. Magnetohydrodynamic Waves in Open Coronal Structures. *Space Sci. Rev.*, 217(7):76, October 2021. doi: 10.1007/s11214-021-00849-0.
- Barthol, P., Gandorfer, A., Solanki, S. K., et al. The Sunrise Mission. *Sol. Phys.*, 268(1):1–34, January 2011. doi: 10.1007/s11207-010-9662-9.
- Beckers, J. M. & Schröter, E. H. The Intensity, Velocity and Magnetic Structure of a Sunspot Region. I: Observational Technique; Properties of Magnetic Knots. *Sol. Phys.*, 4(2):142–164, June 1968. doi: 10.1007/BF00148076.
- Benz, A. O. Flare Observations. *Living Reviews in Solar Physics*, 5(1):1, December 2008. doi: 10.12942/lrsp-2008-1.
- Benz, A. O. Flare Observations. *Living Reviews in Solar Physics*, 14(1):2, December 2017. doi: 10.1007/s41116-016-0004-3.
- Berghmans, D., Clette, F., & Moses, D. Quiet Sun EUV transient brightenings and turbulence. A panoramic view by EIT on board SOHO. *A&A*, 336:1039–1055, August 1998.
- Berghmans, D., McKenzie, D., & Clette, F. Active region transient brightenings. A simultaneous view by SXT, EIT and TRACE. *A&A*, 369:291–304, April 2001. doi: 10.1051/0004-6361:20010142.
- Berghmans, D., Auchère, F., Long, D. M., et al. Extreme-UV quiet Sun brightenings observed by the Solar Orbiter/EUI. *A&A*, 656:L4, December 2021. doi: 10.1051/0004-6361/202140380.
- Bewsher, D., Parnell, C. E., Brown, D. S., & Hood, A. W. Magnetic structure of transition region blinkers. In Sawaya-Lacoste, H., editor, *SOLMAG 2002. Proceedings of the Magnetic Coupling of the Solar Atmosphere Euroconference*, volume 505 of *ESA Special Publication*, pages 239–242, October 2002.
- Biermann, L. Über die Ursache der chromosphärischen Turbulenz und des UV-Exzesses der Sonnenstrahlung. *ZAp*, 25:161, January 1948.
- Biermann, L. & Schlüter, A. Cosmic radiation and cosmic magnetic fields. ii. origin of cosmic magnetic fields. *Phys. Rev.*, 82:863–868, Jun 1951. doi: 10.1103/PhysRev.82.863. URL <https://link.aps.org/doi/10.1103/PhysRev.82.863>.

BIBLIOGRAPHY

- Boerner, P., Edwards, C., Lemen, J., et al. Initial Calibration of the Atmospheric Imaging Assembly (AIA) on the Solar Dynamics Observatory (SDO). *Sol. Phys.*, 275(1-2):41–66, January 2012. doi: 10.1007/s11207-011-9804-8.
- Bray, R. J., Cram, L. E., Durrant, C., & Loughhead, R. E. *Plasma Loops in the Solar Corona*. 1991.
- Canfield, R. C., Reardon, K. P., Leka, K. D., et al. H alpha Surges and X-Ray Jets in AR 7260. *ApJ*, 464:1016, June 1996. doi: 10.1086/177389.
- Carcedo, L., Brown, D. S., Hood, A. W., Neukirch, T., & Wiegmann, T. A Quantitative Method to Optimise Magnetic Field Line Fitting of Observed Coronal Loops. *Sol. Phys.*, 218(1):29–40, December 2003. doi: 10.1023/B:SOLA.0000013045.65499.da.
- Carmichael, H. A Process for Flares. In Hess, W. N., editor, *NASA Special Publication*, volume 50, page 451. 1964.
- Carrington, R. C. On the Distribution of the Solar Spots in Latitudes since the Beginning of the Year 1854, with a Map. *MNRAS*, 19:1–3, November 1858. doi: 10.1093/mnras/19.1.1.
- Chae, J., Qiu, J., Wang, H., & Goode, P. R. Extreme-Ultraviolet Jets and H α Surges in Solar Microflares. *ApJ*, 513(1):L75–L78, March 1999. doi: 10.1086/311910.
- Charbonneau, P. Solar Dynamo Theory. *ARA&A*, 52:251–290, August 2014. doi: 10.1146/annurev-astro-081913-040012.
- Chen, P. F. Coronal Mass Ejections: Models and Their Observational Basis. *Living Reviews in Solar Physics*, 8(1):1, December 2011. doi: 10.12942/lrsp-2011-1.
- Chen, Y., Przybylski, D., Peter, H., et al. Transient small-scale brightenings in the quiet solar corona: A model for campfires observed with Solar Orbiter. *A&A*, 656:L7, December 2021. doi: 10.1051/0004-6361/202140638.
- Cheung, M. C. M., Boerner, P., Schrijver, C. J., et al. Thermal Diagnostics with the Atmospheric Imaging Assembly on board the Solar Dynamics Observatory: A Validated Method for Differential Emission Measure Inversions. *ApJ*, 807(2):143, July 2015. doi: 10.1088/0004-637X/807/2/143.
- Cheung, M. C., De Pontieu, B., Martínez-Sykora, J., et al. Multi-component decomposition of astronomical spectra by compressed sensing. *The Astrophysical Journal*, 882(1):13, 2019.

- Chitta, L. P., Peter, H., Solanki, S. K., et al. Solar Coronal Loops Associated with Small-scale Mixed Polarity Surface Magnetic Fields. *ApJS*, 229(1):4, March 2017. doi: 10.3847/1538-4365/229/1/4.
- Chitta, L. P., Peter, H., & Young, P. R. Extreme-ultraviolet bursts and nanoflares in the quiet-Sun transition region and corona. *A&A*, 647:A159, March 2021a. doi: 10.1051/0004-6361/202039969.
- Chitta, L. P., Solanki, S. K., Peter, H., et al. Capturing transient plasma flows and jets in the solar corona. *A&A*, 656:L13, December 2021b. doi: 10.1051/0004-6361/202141683.
- Chitta, L. P., Solanki, S. K., del Toro Iniesta, J. C., et al. Fleeting Small-scale Surface Magnetic Fields Build the Quiet-Sun Corona. *ApJ*, 956(1):L1, October 2023a. doi: 10.3847/2041-8213/acf136.
- Chitta, L. P., Zhukov, A. N., Berghmans, D., et al. Picoflare jets power the solar wind emerging from a coronal hole on the Sun. *Science*, 381(6660):867–872, August 2023b. doi: 10.1126/science.ade5801.
- Chitta, L. P., Huang, Z., D’Amicis, R., et al. Coronal hole picoflare jets are the progenitors of both the fast and the Alfvénic slow solar wind. *arXiv e-prints*, art. arXiv:2411.16513, November 2024. doi: 10.48550/arXiv.2411.16513.
- Cho, K.-S., Kumar, P., Cho, I.-H., et al. High-resolution Observations of Plume Footpoints in a Solar Coronal Hole. *ApJ*, 953(1):69, August 2023. doi: 10.3847/1538-4357/acd456.
- Cirtain, J. W., Golub, L., Lundquist, L., et al. Evidence for Alfvén Waves in Solar X-ray Jets. *Science*, 318(5856):1580, December 2007. doi: 10.1126/science.1147050.
- Corti, G., Poletto, G., Romoli, M., et al. Physical Parameters in Plume and Interplume Regions from UVCS Observations. In Wilson, A., editor, *Fifth SOHO Workshop: The Corona and Solar Wind Near Minimum Activity*, volume 404 of *ESA Special Publication*, page 289, January 1997.
- Cranmer, S. R., van Ballegoijen, A. A., & Edgar, R. J. Self-consistent Coronal Heating and Solar Wind Acceleration from Anisotropic Magnetohydrodynamic Turbulence. *ApJS*, 171(2):520–551, August 2007. doi: 10.1086/518001.
- Curdt, W., Brekke, P., Feldman, U., et al. The SUMER spectral atlas of solar-disk features. *A&A*, 375:591–613, August 2001. doi: 10.1051/0004-6361:20010364.

BIBLIOGRAPHY

- Curdt, W., Landi, E., & Feldman, U. The SUMER spectral atlas of solar coronal features. *A&A*, 427:1045–1054, December 2004. doi: 10.1051/0004-6361:20041278.
- De Moortel, I., Ireland, J., & Walsh, R. W. Observation of oscillations in coronal loops. *A&A*, 355:L23–L26, March 2000.
- De Pontieu, B., Hansteen, V. H., Rouppe van der Voort, L., van Noort, M., & Carlsson, M. High-Resolution Observations and Modeling of Dynamic Fibrils. *ApJ*, 655(1):624–641, January 2007a. doi: 10.1086/509070.
- De Pontieu, B., McIntosh, S. W., Carlsson, M., et al. The Origins of Hot Plasma in the Solar Corona. *Science*, 331(6013):55, January 2011. doi: 10.1126/science.1197738.
- De Pontieu, B., Title, A. M., Lemen, J. R., et al. The Interface Region Imaging Spectrograph (IRIS). *Sol. Phys.*, 289(7):2733–2779, July 2014. doi: 10.1007/s11207-014-0485-y.
- De Pontieu, B., Erdélyi, R., & James, S. P. Solar chromospheric spicules from the leakage of photospheric oscillations and flows. *Nature*, 430(6999):536–539, July 2004. doi: 10.1038/nature02749.
- De Pontieu, B., McIntosh, S., Hansteen, V. H., et al. A Tale of Two Spicules: The Impact of Spicules on the Magnetic Chromosphere. *PASJ*, 59:S655, November 2007b. doi: 10.1093/pasj/59.sp3.S655.
- De Pontieu, B., McIntosh, S. W., Hansteen, V. H., & Schrijver, C. J. Observing the Roots of Solar Coronal Heating—in the Chromosphere. *ApJ*, 701(1):L1–L6, August 2009. doi: 10.1088/0004-637X/701/1/L1.
- De Pontieu, B., Martínez-Sykora, J., & Chintzoglou, G. What Causes the High Apparent Speeds in Chromospheric and Transition Region Spicules on the Sun? *ApJ*, 849(1):L7, November 2017. doi: 10.3847/2041-8213/aa9272.
- De Pontieu, B., Martínez-Sykora, J., Testa, P., et al. The Multi-slit Approach to Coronal Spectroscopy with the Multi-slit Solar Explorer (MUSE). *ApJ*, 888(1):3, January 2020. doi: 10.3847/1538-4357/ab5b03.
- DeForest, C. E. & Gurman, J. B. Observation of Quasi-periodic Compressive Waves in Solar Polar Plumes. *ApJ*, 501(2):L217–L220, July 1998. doi: 10.1086/311460.
- DeForest, C. E., Hoeksema, J. T., Gurman, J. B., et al. Polar Plume Anatomy: Results of a Coordinated Observation. *Sol. Phys.*, 175(2):393–410, October 1997. doi: 10.1023/A:1004955223306.

- DeForest, C. E., Lamy, P. L., & Llebaria, A. Solar Polar Plume Lifetime and Coronal Hole Expansion: Determination from Long-Term Observations. *ApJ*, 560(1):490–498, October 2001. doi: 10.1086/322497.
- Delaboudinière, J. P., Artzner, G. E., Brunaud, J., et al. EIT: Extreme-Ultraviolet Imaging Telescope for the SOHO Mission. *Sol. Phys.*, 162(1-2):291–312, December 1995. doi: 10.1007/BF00733432.
- Denvir, D. J. & Conroy, E. Electron-multiplying CCD: the new ICCD. In Johnson, C. B., Sinha, D., & Laplante, P. A., editors, *Low-Light-Level and Real-Time Imaging Systems, Components, and Applications*, volume 4796 of *Society of Photo-Optical Instrumentation Engineers (SPIE) Conference Series*, pages 164–174, February 2003. doi: 10.1117/12.457779.
- Dere, K. P., Bartoe, J. D. F., Brueckner, G. E., Ewing, J., & Lund, P. Explosive events and magnetic reconnection in the solar atmosphere. *J. Geophys. Res.*, 96(A6):9399–9407, June 1991. doi: 10.1029/90JA02572.
- Dere, K. P., Landi, E., Mason, H. E., Monsignori Fossi, B. C., & Young, P. R. CHIANTI - an atomic database for emission lines. *A&AS*, 125:149–173, October 1997. doi: 10.1051/aas:1997368.
- Deubner, F. L. & Fleck, B. Dynamics of the solar atmosphere. III - Cell-network distinctions of chromospheric oscillations. *A&A*, 228(2):506–512, February 1990.
- DeVore, C. R. & Antiochos, S. K. Dynamical Formation and Stability of Helical Prominence Magnetic Fields. *ApJ*, 539(2):954–963, August 2000. doi: 10.1086/309275.
- Dolliou, A., Parenti, S., Auchère, F., et al. Temperature of quiet Sun small scale brightenings observed by EU1 on board Solar Orbiter: Evidence for a cooler component. *A&A*, 671:A64, March 2023. doi: 10.1051/0004-6361/202244914.
- Domingo, V., Fleck, B., & Poland, A. I. The SOHO Mission: an Overview. *Sol. Phys.*, 162(1-2):1–37, December 1995. doi: 10.1007/BF00733425.
- Dowdy, Jr., J. F., Rabin, D., & Moore, R. L. On the Magnetic Structure of the Quiet Transition Region. *Sol. Phys.*, 105(1):35–45, May 1986. doi: 10.1007/BF00156374.
- Doyle, J. G., Teriaca, L., & Banerjee, D. Coronal hole diagnostics out to $8R_{sun}$. *A&A*, 349:956–960, September 1999.
- Edlén, B. The identification of the coronal lines (George Darwin Lecture). *MNRAS*, 105:323, January 1945. doi: 10.1093/mnras/105.6.323.

BIBLIOGRAPHY

- Edlén, B. Die Deutung der Emissionslinien im Spektrum der Sonnenkorona. Mit 6 Abbildungen. *ZAp*, 22:30, January 1943.
- Evans, J. W. & Michard, R. Observational Study of Macroscopic Inhomogeneities in the Solar Atmosphere. III. Vertical Oscillatory Motions in the Solar Photosphere. *ApJ*, 136:493, September 1962. doi: 10.1086/147403.
- Feng, L., Inhester, B., Solanki, S. K., et al. First Stereoscopic Coronal Loop Reconstructions from STEREO SECCHI Images. *ApJ*, 671(2):L205–L208, December 2007. doi: 10.1086/525525.
- Feng, L., Inhester, B., Solanki, S. K., et al. Stereoscopic Polar Plume Reconstructions from STEREO/SECCHI Images. *ApJ*, 700(1):292–301, July 2009. doi: 10.1088/0004-637X/700/1/292.
- Fludra, A., Del Zanna, G., Alexander, D., & Bromage, B. J. I. Electron density and temperature of the lower solar corona. *J. Geophys. Res.*, 104(A5):9709–9720, May 1999. doi: 10.1029/1998JA900033.
- Fludra, A., Griffin, D., Caldwell, M., et al. SPICE EUV spectrometer for the Solar Orbiter mission. In Fineschi, S. & Fennelly, J., editors, *Solar Physics and Space Weather Instrumentation V*, volume 8862 of *Society of Photo-Optical Instrumentation Engineers (SPIE) Conference Series*, page 88620F, September 2013. doi: 10.1117/12.2027581.
- Fu, H., Xia, L., Li, B., et al. Measurements of Outflow Velocities in on-disk Plumes from EIS/Hinode Observations. *ApJ*, 794(2):109, October 2014. doi: 10.1088/0004-637X/794/2/109.
- Gabriel, A., Bely-Dubau, F., Tison, E., & Wilhelm, K. The Structure and Origin of Solar Plumes: Network Plumes. *ApJ*, 700(1):551–558, July 2009. doi: 10.1088/0004-637X/700/1/551.
- Gabriel, A. H., Bely-Dubau, F., & Lemaire, P. The Contribution of Polar Plumes to the Fast Solar Wind. *ApJ*, 589(1):623–634, May 2003. doi: 10.1086/374416.
- Gabriel, A. H., Abbo, L., Bely-Dubau, F., Llebaria, A., & Antonucci, E. Solar Wind Outflow in Polar Plumes from 1.05 to 2.4 R_{solar} . *ApJ*, 635(2):L185–L188, December 2005. doi: 10.1086/499521.
- Gabriel, A. H. & Mason, H. E. 10 - solar physics. In MASSEY, H. & BATES, D., editors, *Applied Atomic Collision Physics*, pages 345–397. Academic Press, 1982. ISBN 978-0-12-478801-5. doi: <https://doi.org/10.1016/B978-0-12-478801-5.50016-5>. URL <https://www.sciencedirect.com/science/article/pii/B9780124788015500165>.

- Gary, G. A. Plasma Beta above a Solar Active Region: Rethinking the Paradigm. *Sol. Phys.*, 203(1):71–86, October 2001. doi: 10.1023/A:1012722021820.
- Gary, G. A. & Hagyard, M. J. Transformation of vector magnetograms and the problems associated with the effects of perspective and the azimuthal ambiguity. *Sol. Phys.*, 126:21–36, March 1990. doi: 10.1007/BF00158295.
- Gnevyshev, M. N. On the life-length of the sun-spots. *Pulkovo observatory circular*, (24):37, 1938.
- Golub, L., Krieger, A. S., Silk, J. K., Timothy, A. F., & Vaiana, G. S. Solar X-Ray Bright Points. *ApJ*, 189:L93, April 1974. doi: 10.1086/181472.
- Golub, L., Krieger, A. S., Harvey, J. W., & Vaiana, G. S. Magnetic properties of X-ray bright points. *Sol. Phys.*, 53(1):111–121, July 1977. doi: 10.1007/BF02260212.
- Grotian, W. Zur Frage der Deutung der Linien im Spektrum der Sonnenkorona. *Naturwissenschaften*, 27(13):214–214, March 1939. doi: 10.1007/BF01488890.
- Guennou, C., Auchère, F., Soubrié, E., et al. On the Accuracy of the Differential Emission Measure Diagnostics of Solar Plasmas. Application to SDO/AIA. II. Multithermal Plasmas. *ApJS*, 203(2):26, December 2012. doi: 10.1088/0067-0049/203/2/26.
- Habbal, S. R. & Withbroe, G. L. Spatial and Temporal Variations of EUV Coronal Bright Points. *Sol. Phys.*, 69(1):77–97, January 1981. doi: 10.1007/BF00151257.
- Habbal, S. R., Esser, R., Guhathakurta, M., & Fisher, R. R. Flow properties of the solar wind derived from a two-fluid model with constraints from white light and in situ interplanetary observations. *Geophys. Res. Lett.*, 22(12): 1465–1468, June 1995. doi: 10.1029/95GL01064.
- Halain, J. P., Mazzoli, A., Meining, S., et al. The extreme ultraviolet imager of solar orbiter: optical design and alignment scheme. In Fineschi, S. & Fennelly, J., editors, *Solar Physics and Space Weather Instrumentation VI*, volume 9604 of *Society of Photo-Optical Instrumentation Engineers (SPIE) Conference Series*, page 96040H, September 2015. doi: 10.1117/12.2185631.
- Hale, G. E. On the Probable Existence of a Magnetic Field in Sun-Spots. *ApJ*, 28:315, November 1908. doi: 10.1086/141602.
- Handy, B. N., Acton, L. W., Kankelborg, C. C., et al. The transition region and coronal explorer. *Sol. Phys.*, 187(2):229–260, July 1999. doi: 10.1023/A:1005166902804.

BIBLIOGRAPHY

- Hannah, I. G. & Kontar, E. P. Differential emission measures from the regularized inversion of Hinode and SDO data. *A&A*, 539:A146, March 2012. doi: 10.1051/0004-6361/201117576.
- Hansteen, V. H., De Pontieu, B., Rouppe van der Voort, L., van Noort, M., & Carlsson, M. Dynamic Fibrils Are Driven by Magnetoacoustic Shocks. *ApJ*, 647(1):L73–L76, August 2006. doi: 10.1086/507452.
- Harvey, K. L., Sheeley, Jr., N. R., & Harvey, J. W. Magnetic measurements of coronal holes during 1975–1980. *Sol. Phys.*, 79(1):149–160, July 1982. doi: 10.1007/BF00146979.
- Harvey, K. L., Strong, K. T., Nitta, N., & Tsuneta, S. Lifetimes and distribution of coronal bright points observed with Yohkoh. *Advances in Space Research*, 13(9):27–30, September 1993. doi: 10.1016/0273-1177(93)90453-I.
- Harvey, K. L. & Zwaan, C. Properties and Emergence Patterns of Bipolar Active Regions - Part One. *Sol. Phys.*, 148(1):85–118, November 1993. doi: 10.1007/BF00675537.
- Hassler, D. M. Spectroscopic Observations of Polar Plumes with SOHO/SUMMER. In Livingston, W. & Özgüç, A., editors, *Last Total Solar Eclipse of the Millennium*, volume 205 of *Astronomical Society of the Pacific Conference Series*, page 83, April 2000.
- Hassler, D. M., Wilhelm, K., Lemaire, P., & Schühle, U. Observations of Polar Plumes with the SUMER Instrument on SOHO. *Sol. Phys.*, 175(2):375–391, October 1997. doi: 10.1023/A:1004959324214.
- Hassler, D. M., Dammasch, I. E., Lemaire, P., et al. Solar Wind Outflow and the Chromospheric Magnetic Network. *Science*, 283:810, February 1999. doi: 10.1126/science.283.5403.810.
- Hathaway, D. H. The Solar Cycle. *Living Reviews in Solar Physics*, 12(1):4, December 2015. doi: 10.1007/lrsp-2015-4.
- Hayashi, C. Stellar evolution in early phases of gravitational contraction. *PASJ*, 13:450–452, December 1961.
- Hegglund, L., De Pontieu, B., & Hansteen, V. H. Numerical Simulations of Shock Wave-driven Chromospheric Jets. *ApJ*, 666(2):1277–1283, September 2007. doi: 10.1086/518828.
- Henriques, V. M. J., Kuridze, D., Mathioudakis, M., & Keenan, F. P. Quiet-Sun H α Transients and Corresponding Small-scale Transition Region and Coronal Heating. *ApJ*, 820(2):124, April 2016. doi: 10.3847/0004-637X/820/2/124.

- Heyvaerts, J., Priest, E. R., & Rust, D. M. An emerging flux model for the solar phenomenon. *ApJ*, 216:123–137, August 1977. doi: 10.1086/155453.
- Hick, P. & Jackson, B. V. Evidence of active region imprints on the solar wind structure. In *Solar Wind Eight*, page 48, June 1995.
- Hick, P., Jackson, B. V., Rappoport, S., et al. Synoptic IPS and Yohkoh soft X-ray observations. *Geophys. Res. Lett.*, 22(5):643–646, March 1995. doi: 10.1029/95GL00011.
- Hirayama, T. Theoretical Model of Flares and Prominences. I: Evaporating Flare Model. *Sol. Phys.*, 34(2):323–338, February 1974. doi: 10.1007/BF00153671.
- Hoeksema, J. T., Liu, Y., Hayashi, K., et al. The Helioseismic and Magnetic Imager (HMI) Vector Magnetic Field Pipeline: Overview and Performance. *Sol. Phys.*, 289(9):3483–3530, September 2014. doi: 10.1007/s11207-014-0516-8.
- Hollweg, J. V. Fast wave evanescence in the solar corona. *Geophys. Res. Lett.*, 5(8):731–734, August 1978. doi: 10.1029/GL005i008p00731.
- Horbury, T. S., O’Brien, H., Carrasco Blazquez, I., et al. The Solar Orbiter magnetometer. *A&A*, 642:A9, October 2020. doi: 10.1051/0004-6361/201937257.
- Innes, D. E., Inhester, B., Axford, W. I., & Wilhelm, K. Bi-directional plasma jets produced by magnetic reconnection on the Sun. *Nature*, 386(6627):811–813, April 1997. doi: 10.1038/386811a0.
- Janssens, T. J. Long Term Observations of the H α Chromospheric Network. *Sol. Phys.*, 11(2):222–242, February 1970. doi: 10.1007/BF00155222.
- Joulin, V., Buchlin, E., Solomon, J., & Guennou, C. Energetic characterisation and statistics of solar coronal brightenings. *A&A*, 591:A148, July 2016. doi: 10.1051/0004-6361/201526254.
- Kahil, F., Hirzberger, J., Solanki, S. K., et al. The magnetic drivers of campfires seen by the Polarimetric and Helioseismic Imager (PHI) on Solar Orbiter. *A&A*, 660:A143, April 2022. doi: 10.1051/0004-6361/202142873.
- Kashyap, V. & Drake, J. J. Markov-Chain Monte Carlo Reconstruction of Emission Measure Distributions: Application to Solar Extreme-Ultraviolet Spectra. *ApJ*, 503(1):450–466, August 1998. doi: 10.1086/305964.

BIBLIOGRAPHY

- Kayshap, P. & Dwivedi, B. N. Diagnostics of Coronal Bright Points using IRIS, AIA, and HMI Observations. *Sol. Phys.*, 292(8):108, August 2017. doi: 10.1007/s11207-017-1132-1.
- Keller, C. U., Schüssler, M., Vögler, A., & Zakharov, V. On the Origin of Solar Faculae. *ApJ*, 607(1):L59–L62, May 2004. doi: 10.1086/421553.
- Klimchuk, J. A. The role of type II spicules in the upper solar atmosphere. *Journal of Geophysical Research (Space Physics)*, 117(A12):A12102, December 2012. doi: 10.1029/2012JA018170.
- Kojima, M., Washimi, H., Misawa, H., & Hakamada, K. Solar wind observed within 0.3 AU with interplanetary scintillation. In Marsch, E. & Schwenn, R., editors, *Solar Wind Seven Colloquium*, pages 201–204, January 1992.
- Kopp, R. A. & Pneuman, G. W. Magnetic reconnection in the corona and the loop prominence phenomenon. *Sol. Phys.*, 50(1):85–98, September 1976. doi: 10.1007/BF00206193.
- Kosugi, T., Matsuzaki, K., Sakao, T., et al. The Hinode (Solar-B) Mission: An Overview. *Sol. Phys.*, 243(1):3–17, June 2007. doi: 10.1007/s11207-007-9014-6.
- Krieger, A. S., Timothy, A. F., & Roelof, E. C. A Coronal Hole and Its Identification as the Source of a High Velocity Solar Wind Stream. *Sol. Phys.*, 29(2):505–525, April 1973. doi: 10.1007/BF00150828.
- Krishna Prasad, S., Banerjee, D., Van Doorselaere, T., & Singh, J. Omnipresent long-period intensity oscillations in open coronal structures. *A&A*, 546:A50, October 2012. doi: 10.1051/0004-6361/201219885.
- Krucker, S. & Benz, A. O. Energy Distribution of Heating Processes in the Quiet Solar Corona. *ApJ*, 501(2):L213–L216, July 1998. doi: 10.1086/311474.
- Krucker, S., Hurford, G. J., Grimm, O., et al. The Spectrometer/Telescope for Imaging X-rays (STIX). *A&A*, 642:A15, October 2020. doi: 10.1051/0004-6361/201937362.
- Kumar, P., Karpen, J. T., Uritsky, V. M., et al. Quasi-periodic Energy Release and Jets at the Base of Solar Coronal Plumes. *ApJ*, 933(1):21, July 2022. doi: 10.3847/1538-4357/ac6c24.
- Lagg, A., Solanki, S. K., Riethmüller, T. L., et al. Fully Resolved Quiet-Sun Magnetic flux Tube Observed with the SUNRISE/IMAX Instrument. *ApJ*, 723(2):L164–L168, November 2010. doi: 10.1088/2041-8205/723/2/L164.

- Lamy, P., Liebaria, A., Koutchmy, S., et al. Characterisation of Polar Plumes from LASCO-C2 Images in Early 1996. In Wilson, A., editor, *Fifth SOHO Workshop: The Corona and Solar Wind Near Minimum Activity*, volume 404 of *ESA Special Publication*, page 487, January 1997.
- Landi, E., Young, P. R., Dere, K. P., Del Zanna, G., & Mason, H. E. CHIANTI—An Atomic Database for Emission Lines. XIII. Soft X-Ray Improvements and Other Changes. *ApJ*, 763(2):86, February 2013. doi: 10.1088/0004-637X/763/2/86.
- Langangen, Ø., De Pontieu, B., Carlsson, M., et al. Search for High Velocities in the Disk Counterpart of Type II Spicules. *ApJ*, 679(2):L167, June 2008. doi: 10.1086/589442.
- Leibacher, J. W. & Stein, R. F. A New Description of the Solar Five-Minute Oscillation. *Astrophys. Lett.*, 7:191–192, January 1971.
- Leighton, R. B., Noyes, R. W., & Simon, G. W. Velocity Fields in the Solar Atmosphere. I. Preliminary Report. *ApJ*, 135:474, March 1962. doi: 10.1086/147285.
- Lemen, J. R., Title, A. M., Akin, D. J., et al. The Atmospheric Imaging Assembly (AIA) on the Solar Dynamics Observatory (SDO). *Sol. Phys.*, 275(1-2):17–40, January 2012. doi: 10.1007/s11207-011-9776-8.
- Lindeberg, T. Scale-space theory: A basic tool for analysing structures at different scales. *Journal of Applied Statistics*, 21:224–270, 09 1994. doi: 10.1080/757582976.
- Lites, B. W. & Thomas, J. H. Sunspot umbral oscillations in the photosphere and low chromosphere. *ApJ*, 294:682–688, July 1985. doi: 10.1086/163338.
- Lites, B. W., Elmore, D. F., Seagraves, P., & Skumanich, A. P. Stokes Profile Analysis and Vector Magnetic Fields. VI. Fine Scale Structure of a Sunspot. *ApJ*, 418:928, December 1993. doi: 10.1086/173450.
- Livingston, W. Sunspots Observed to Physically Weaken in 2000-2001. *Sol. Phys.*, 207(1):41–45, May 2002. doi: 10.1023/A:1015555000456.
- Livingston, W. C. & Orrall, F. Q. Magnetic Pukas and the Lifetime of the Supergranulation. *Sol. Phys.*, 39(2):301–304, March 1974. doi: 10.1007/BF00162421.
- Lowe, D. G. Distinctive Image Features from Scale-Invariant Keypoints. *International Journal of Computer Vision*, 60(2):91–110, November 2004. ISSN 1573-1405. doi: 10.1023/B:VISI.0000029664.99615.94. URL <https://doi.org/10.1023/B:VISI.0000029664.99615.94>.

BIBLIOGRAPHY

- Madjarska, M. S. Coronal bright points. *Living Reviews in Solar Physics*, 16(1): 2, December 2019. doi: 10.1007/s41116-019-0018-8.
- Maksimovic, M., Bale, S. D., Chust, T., et al. The Solar Orbiter Radio and Plasma Waves (RPW) instrument. *A&A*, 642:A12, October 2020. doi: 10.1051/0004-6361/201936214.
- Mandal, S., Peter, H., Chitta, L. P., et al. Propagating brightenings in small loop-like structures in the quiet-Sun corona: Observations from Solar Orbiter/EUI. *A&A*, 656:L16, December 2021. doi: 10.1051/0004-6361/202142041.
- Mandal, S., Peter, H., Chitta, L. P., et al. Evolution of dynamic fibrils from the cooler chromosphere to the hotter corona. *A&A*, 678:L5, October 2023. doi: 10.1051/0004-6361/202347343.
- Mariska, J. T. The solar transition region. *Cambridge Astrophysics Series*, 23, January 1992.
- Martínez-Sykora, J., De Pontieu, B., De Moortel, I., Hansteen, V. H., & Carlsson, M. Impact of Type II Spicules in the Corona: Simulations and Synthetic Observables. *ApJ*, 860(2):116, June 2018. doi: 10.3847/1538-4357/aac2ca.
- Maunder, E. W. Note on the Distribution of Sun-spots in Heliographic Latitude, 1874-1902. *MNRAS*, 64:747–761, June 1904. doi: 10.1093/mnras/64.8.747.
- McComas, D. J., Angold, N., Elliott, H. A., et al. Weakest Solar Wind of the Space Age and the Current “Mini” Solar Maximum. *ApJ*, 779(1):2, December 2013. doi: 10.1088/0004-637X/779/1/2.
- McEwan, M. P. & de Moortel, I. Longitudinal intensity oscillations observed with TRACE: evidence of fine-scale structure. *A&A*, 448(2):763–770, March 2006. doi: 10.1051/0004-6361:20054041.
- McIntosh, S. W., Innes, D. E., de Pontieu, B., & Leamon, R. J. STEREO observations of quasi-periodically driven high velocity outflows in polar plumes. *A&A*, 510:L2, February 2010. doi: 10.1051/0004-6361/200913699.
- McIntosh, S. W., de Pontieu, B., Carlsson, M., et al. Alfvénic waves with sufficient energy to power the quiet solar corona and fast solar wind. *Nature*, 475(7357):477–480, July 2011. doi: 10.1038/nature10235.
- Metcalf, T. R. Resolving the 180-degree ambiguity in vector magnetic field measurements: The ‘minimum’ energy solution. *Sol. Phys.*, 155(2):235–242, December 1994. doi: 10.1007/BF00680593.

- Metcalf, T. R., Leka, K. D., Barnes, G., et al. An Overview of Existing Algorithms for Resolving the 180 Ambiguity in Vector Magnetic Fields: Quantitative Tests with Synthetic Data. *Sol. Phys.*, 237(2):267–296, September 2006. doi: 10.1007/s11207-006-0170-x.
- Mou, C., Madjarska, M. S., Galsgaard, K., & Xia, L. Eruptions from quiet Sun coronal bright points. I. Observations. *A&A*, 619:A55, November 2018. doi: 10.1051/0004-6361/201833243.
- Müller, D., Marsden, R. G., St. Cyr, O. C., Gilbert, H. R., & Solar Orbiter Team. Solar Orbiter. Exploring the Sun-Heliosphere Connection. *Sol. Phys.*, 285(1-2):25–70, July 2013. doi: 10.1007/s11207-012-0085-7.
- Müller, D., St. Cyr, O. C., Zouganelis, I., et al. The Solar Orbiter mission. Science overview. *A&A*, 642:A1, October 2020. doi: 10.1051/0004-6361/202038467.
- Narain, U. & Ulmschneider, P. Chromospheric and Coronal Heating Mechanisms II. *Space Sci. Rev.*, 75(3-4):453–509, February 1996. doi: 10.1007/BF00833341.
- Narang, N., Arbacher, R. T., Tian, H., et al. Statistical Study of Network Jets Observed in the Solar Transition Region: a Comparison Between Coronal Holes and Quiet-Sun Regions. *Sol. Phys.*, 291(4):1129–1142, April 2016. doi: 10.1007/s11207-016-0886-1.
- Nelson, C. J., Auchère, F., Aznar Cuadrado, R., et al. Extreme-ultraviolet brightenings in the quiet Sun: Signatures in spectral and imaging data from the Interface Region Imaging Spectrograph. *A&A*, 676:A64, August 2023. doi: 10.1051/0004-6361/202346144.
- Neugebauer, M., Forsyth, R. J., Galvin, A. B., et al. Spatial structure of the solar wind and comparisons with solar data and models. *J. Geophys. Res.*, 103(A7):14587–14600, July 1998. doi: 10.1029/98JA00798.
- Neugebauer, M. & Snyder, C. W. Mariner 2 Observations of the Solar Wind, 2, Relation of Plasma Properties to the Magnetic Field. *J. Geophys. Res.*, 72: 1823, April 1967. doi: 10.1029/JZ072i007p01823.
- Newkirk, Jr., G. Structure of the Solar Corona. *ARA&A*, 5:213, January 1967. doi: 10.1146/annurev.aa.05.090167.001241.
- Newkirk, Jr., G. & Harvey, J. Coronal Polar Plumes. *Sol. Phys.*, 3(2):321–343, February 1968. doi: 10.1007/BF00155166.
- Noci, G., Kohl, J. L., & Withbroe, G. L. Solar Wind Diagnostics from Doppler-enhanced Scattering. *ApJ*, 315:706, April 1987. doi: 10.1086/165172.

BIBLIOGRAPHY

- Nolte, J. T., Krieger, A. S., Timothy, A. F., et al. Coronal holes as sources of solar wind. *Sol. Phys.*, 46(2):303–322, February 1976. doi: 10.1007/BF00149859.
- Nordlund, Å., Stein, R. F., & Asplund, M. Solar Surface Convection. *Living Reviews in Solar Physics*, 6(1):2, December 2009. doi: 10.12942/lrsp-2009-2.
- Ofman, L., Nakariakov, V. M., & DeForest, C. E. Slow Magnetosonic Waves in Coronal Plumes. *ApJ*, 514(1):441–447, March 1999. doi: 10.1086/306944.
- Ogilvie, K. W. & Desch, M. D. The wind spacecraft and its early scientific results. *Advances in Space Research*, 20(4-5):559–568, January 1997. doi: 10.1016/S0273-1177(97)00439-0.
- Orozco Suárez, D., Bellot Rubio, L. R., del Toro Iniesta, J. C., et al. Quiet-Sun Internetwork Magnetic Fields from the Inversion of Hinode Measurements. *ApJ*, 670(1):L61–L64, November 2007. doi: 10.1086/524139.
- Owen, C. J., Bruno, R., Livi, S., et al. The Solar Orbiter Solar Wind Analyser (SWA) suite. *A&A*, 642:A16, October 2020. doi: 10.1051/0004-6361/201937259.
- Panesar, N. K., Sterling, A. C., Moore, R. L., et al. IRIS and SDO Observations of Solar Jetlets Resulting from Network-edge Flux Cancellation. *ApJ*, 868(2): L27, December 2018. doi: 10.3847/2041-8213/aaef37.
- Panesar, N. K., Tiwari, S. K., Berghmans, D., et al. The Magnetic Origin of Solar Campfires. *ApJ*, 921(1):L20, November 2021. doi: 10.3847/2041-8213/ac3007.
- Pant, V., Dolla, L., Mazumder, R., et al. Dynamics of On-disk Plumes as Observed with the Interface Region Imaging Spectrograph, the Atmospheric Imaging Assembly, and the Helioseismic and Magnetic Imager. *ApJ*, 807(1): 71, July 2015. doi: 10.1088/0004-637X/807/1/71.
- Paraschiv, A. R., Bemporad, A., & Sterling, A. C. Physical properties of solar polar jets. A statistical study with Hinode XRT data. *A&A*, 579:A96, July 2015. doi: 10.1051/0004-6361/201525671.
- Parenti, S. Solar Prominences: Observations. *Living Reviews in Solar Physics*, 11(1):1, December 2014. doi: 10.12942/lrsp-2014-1.
- Parker, E. N. Acceleration of Cosmic Rays in Solar Flares. *Physical Review*, 107 (3):830–836, August 1957. doi: 10.1103/PhysRev.107.830.
- Parker, E. N. Dynamics of the Interplanetary Gas and Magnetic Fields. *ApJ*, 128:664, November 1958. doi: 10.1086/146579.

- Parker, E. N. The passage of energetic charged particles through interplanetary space. *Planet. Space Sci.*, 13(1):9–49, January 1965. doi: 10.1016/0032-0633(65)90131-5.
- Parker, E. N. Topological Dissipation and the Small-Scale Fields in Turbulent Gases. *ApJ*, 174:499, June 1972. doi: 10.1086/151512.
- Parker, E. N. Magnetic Neutral Sheets in Evolving Fields - Part Two - Formation of the Solar Corona. *ApJ*, 264:642, January 1983. doi: 10.1086/160637.
- Parker, E. N. Nanoflares and the Solar X-Ray Corona. *ApJ*, 330:474, July 1988. doi: 10.1086/166485.
- Parker, E. N. Hydromagnetic Dynamo Models. *ApJ*, 122:293, September 1955. doi: 10.1086/146087.
- Parnell, C. E. & Priest, E. R. A converging flux model for the formation of an X-ray bright point above a supergranule cell. *Geophysical and Astrophysical Fluid Dynamics*, 80(3):255–276, January 1995. doi: 10.1080/03091929508228958.
- Parnell, C. E., Bewsher, D., & Harrison, R. A. Transition-Region Blinkers - II. Active-Region Properties. *Sol. Phys.*, 206(2):249–271, April 2002. doi: 10.1023/A:1015094119974.
- Patsourakos, S., Vial, J. C., Gabriel, A. H., & Bellamine, N. Transition-Region Network Boundaries in the Quiet Sun: Width Variation with Temperature as Observed with CDS on SOHO. *ApJ*, 522(1):540–546, September 1999. doi: 10.1086/307609.
- Pauluhn, A. & Solanki, S. K. A nanoflare model of quiet Sun EUV emission. *A&A*, 462(1):311–322, January 2007. doi: 10.1051/0004-6361:20065152.
- Pereira, T. M. D., De Pontieu, B., Carlsson, M., et al. An Interface Region Imaging Spectrograph First View on Solar Spicules. *ApJ*, 792(1):L15, September 2014. doi: 10.1088/2041-8205/792/1/L15.
- Pesnell, W. D., Thompson, B. J., & Chamberlin, P. C. The Solar Dynamics Observatory (SDO). *Sol. Phys.*, 275(1-2):3–15, January 2012. doi: 10.1007/s11207-011-9841-3.
- Petschek, H. E. Magnetic Field Annihilation. In Hess, W. N., editor, *NASA Special Publication*, volume 50, page 425. 1964.
- Phillips, K. J. H., Feldman, U., & Landi, E. *Ultraviolet and X-ray Spectroscopy of the Solar Atmosphere*. 2008. doi: 10.1017/CBO9780511585968.

BIBLIOGRAPHY

- Planck, M. *The Theory of Heat Radiation*. Dover Books on Physics Series. Dover Publications, 1991. ISBN 978-0-486-66811-6. URL <https://books.google.de/books?id=UnGPVwLybcEC>.
- Poletto, G. Solar Coronal Plumes. *Living Reviews in Solar Physics*, 12(1):7, December 2015. ISSN 1614-4961. doi: 10.1007/lrsp-2015-7. URL <https://doi.org/10.1007/lrsp-2015-7>.
- Preś, P. & Phillips, K. H. J. The Magnetic Association of Coronal Bright Points. *ApJ*, 510(1):L73–L76, January 1999. doi: 10.1086/311791.
- Priest, E. R., Parnell, C. E., & Martin, S. F. A Converging Flux Model of an X-Ray Bright Point and an Associated Canceling Magnetic Feature. *ApJ*, 427:459, May 1994. doi: 10.1086/174157.
- Priest, E. R., Hood, A. W., & Bewsher, D. The Nature of Blinkers and the Solar Transition Region. *Sol. Phys.*, 205(2):249–264, February 2002a. doi: 10.1023/A:1014249729772.
- Priest, E. R., Chitta, L. P., & Syntelis, P. A Cancellation Nanoflare Model for Solar Chromospheric and Coronal Heating. *ApJ*, 862(2):L24, August 2018. doi: 10.3847/2041-8213/aad4fc.
- Priest, E. R., Heyvaerts, J. F., & Title, A. M. A Flux-Tube Tectonics Model for Solar Coronal Heating Driven by the Magnetic Carpet. *ApJ*, 576(1):533–551, September 2002b. doi: 10.1086/341539.
- Pucci, S., Poletto, G., Sterling, A. C., & Romoli, M. Birth, Life, and Death of a Solar Coronal Plume. *ApJ*, 793(2):86, October 2014. doi: 10.1088/0004-637X/793/2/86.
- Raouafi, N. E. & Stenborg, G. Role of Transients in the Sustainability of Solar Coronal Plumes. *ApJ*, 787(2):118, June 2014. doi: 10.1088/0004-637X/787/2/118.
- Raouafi, N. E., Petrie, G. J. D., Norton, A. A., Henney, C. J., & Solanki, S. K. Evidence for Polar Jets as Precursors of Polar Plume Formation. *ApJ*, 682(2):L137, August 2008. doi: 10.1086/591125.
- Raouafi, N. E., Matteini, L., Squire, J., et al. Parker Solar Probe: Four Years of Discoveries at Solar Cycle Minimum. *Space Sci. Rev.*, 219(1):8, February 2023. doi: 10.1007/s11214-023-00952-4.
- Raymond, J. C. & Doyle, J. G. The energy balance in coronal holes and average quiet-sun regions. *ApJ*, 247:686–691, July 1981. doi: 10.1086/159080.

- Régnier, S. & Amari, T. 3D magnetic configuration of the H α filament and X-ray sigmoid in NOAA AR 8151. *A&A*, 425:345–352, October 2004. doi: 10.1051/0004-6361:20034383.
- Régnier, S., Amari, T., & Kersalé, E. 3D Coronal magnetic field from vector magnetograms: non-constant-alpha force-free configuration of the active region NOAA 8151. *A&A*, 392:1119–1127, September 2002. doi: 10.1051/0004-6361:20020993.
- Rieutord, M. & Rincon, F. The Sun's Supergranulation. *Living Reviews in Solar Physics*, 7(1):2, December 2010. doi: 10.12942/lrsp-2010-2.
- Riley, P., Linker, J. A., Mikić, Z., et al. A Comparison between Global Solar Magnetohydrodynamic and Potential Field Source Surface Model Results. *ApJ*, 653(2):1510–1516, December 2006. doi: 10.1086/508565.
- Rimmele, T. R., Warner, M., Keil, S. L., et al. The Daniel K. Inouye Solar Telescope - Observatory Overview. *Sol. Phys.*, 295(12):172, December 2020. doi: 10.1007/s11207-020-01736-7.
- Rochus, P., Auchère, F., Berghmans, D., et al. The Solar Orbiter EUV instrument: The Extreme Ultraviolet Imager. *A&A*, 642:A8, October 2020. doi: 10.1051/0004-6361/201936663.
- Rodríguez-Pacheco, J., Wimmer-Schweingruber, R. F., Mason, G. M., et al. The Energetic Particle Detector. Energetic particle instrument suite for the Solar Orbiter mission. *A&A*, 642:A7, October 2020. doi: 10.1051/0004-6361/201935287.
- Rosner, R., Tucker, W. H., & Vaiana, G. S. Dynamics of the quiescent solar corona. *ApJ*, 220:643–645, March 1978. doi: 10.1086/155949.
- Roudier, T. & Muller, R. Structure of the solar granulation. *Sol. Phys.*, 107(1): 11–26, March 1986. doi: 10.1007/BF00155337.
- Roupe van der Voort, L., Leenaarts, J., de Pontieu, B., Carlsson, M., & Vissers, G. On-disk Counterparts of Type II Spicules in the Ca II 854.2 nm and H α Lines. *ApJ*, 705(1):272–284, November 2009. doi: 10.1088/0004-637X/705/1/272.
- Roupe van der Voort, L. H. M., De Pontieu, B., Hansteen, V. H., Carlsson, M., & van Noort, M. Magnetoacoustic Shocks as a Driver of Quiet-Sun Mottles. *ApJ*, 660(2):L169–L172, May 2007. doi: 10.1086/518246.
- Roy, J. R. The Dynamics of Solar Surges. *Sol. Phys.*, 32(1):139–151, September 1973. doi: 10.1007/BF00152734.

BIBLIOGRAPHY

- Sackmann, I. J., Boothroyd, A. I., & Kraemer, K. E. Our Sun. III. Present and Future. *ApJ*, 418:457, November 1993. doi: 10.1086/173407.
- Saito, K. Photometry of the Solar Corona at the Eclipse on June 20, 1955. *PASJ*, 8:126, January 1956.
- Sakurai, T. Computational Modeling of Magnetic Fields in Solar Active Regions. *Space Sci. Rev.*, 51(1-2):11–48, October 1989. doi: 10.1007/BF00226267.
- Sánchez Cuberes, M., Vázquez, M., Bonet, J. A., & Sobotka, M. Infrared Photometry of Solar Photospheric Structures. II. Center-to-Limb Variation of Active Regions. *ApJ*, 570(2):886–899, May 2002. doi: 10.1086/339737.
- Sanchez-Ibarra, A. & Barraza-Paredes, M. World data center A for solar-terrestrial physics. Catalog of coronal holes, 1970-1991, October 1992.
- Sandman, A. W., Aschwanden, M. J., DeRosa, M. L., Wülser, J. P., & Alexander, D. Comparison of STEREO/EUVI Loops with Potential Magnetic Field Models. *Sol. Phys.*, 259(1-2):1, October 2009. doi: 10.1007/s11207-009-9383-0.
- Scharmer, G. B., Bjelksjo, K., Korhonen, T. K., Lindberg, B., & Petterson, B. The 1-meter Swedish solar telescope. In Keil, S. L. & Avakyan, S. V., editors, *Innovative Telescopes and Instrumentation for Solar Astrophysics*, volume 4853 of *Society of Photo-Optical Instrumentation Engineers (SPIE) Conference Series*, pages 341–350, February 2003. doi: 10.1117/12.460377.
- Schatten, K. H., Wilcox, J. M., & Ness, N. F. A model of interplanetary and coronal magnetic fields. *Sol. Phys.*, 6(3):442–455, March 1969. doi: 10.1007/BF00146478.
- Scherrer, P. H., Schou, J., Bush, R. I., et al. The Helioseismic and Magnetic Imager (HMI) Investigation for the Solar Dynamics Observatory (SDO). *Sol. Phys.*, 275(1-2):207–227, January 2012. doi: 10.1007/s11207-011-9834-2.
- Schmahl, E. J. The Physical Relationship Between Flares and Surges Observed in the Extreme Ultraviolet. *Sol. Phys.*, 69(1):135–146, January 1981. doi: 10.1007/BF00151261.
- Schmidt, W., von der Lühse, O., Volkmer, R., et al. The 1.5 meter solar telescope GREGOR. *Astronomische Nachrichten*, 333(9):796–809, November 2012. doi: 10.1002/asna.201211725.
- Schmieder, B., Mein, P., Simnett, G. M., & Tandberg-Hanssen, E. An example of the association of X-ray and UV emission with H-alpha surges. *A&A*, 201(2):327–338, August 1988.

- Schou, J., Antia, H. M., Basu, S., et al. Helioseismic Studies of Differential Rotation in the Solar Envelope by the Solar Oscillations Investigation Using the Michelson Doppler Imager. *ApJ*, 505(1):390–417, September 1998. doi: 10.1086/306146.
- Schrijver, C. J., DeRosa, M. L., Metcalf, T., et al. Nonlinear Force-free Field Modeling of a Solar Active Region around the Time of a Major Flare and Coronal Mass Ejection. *ApJ*, 675(2):1637–1644, March 2008. doi: 10.1086/527413.
- Schrijver, C. J. & Title, A. M. The Magnetic Connection between the Solar Photosphere and the Corona. *ApJ*, 597(2):L165–L168, November 2003. doi: 10.1086/379870.
- Schrijver, C. J. & van Ballegooijen, A. A. Is the Quiet-Sun Corona a Quasi-steady, Force-free Environment? *ApJ*, 630(1):552–560, September 2005. doi: 10.1086/431754.
- Schrijver, C. J., Title, A. M., van Ballegooijen, A. A., Hagenaar, H. J., & Shine, R. A. Sustaining the Quiet Photospheric Network: The Balance of Flux Emergence, Fragmentation, Merging, and Cancellation. *ApJ*, 487(1):424–436, September 1997. doi: 10.1086/304581.
- Schrijver, C. J., De Rosa, M. L., Title, A. M., & Metcalf, T. R. The Non-potentiality of Active-Region Coronae and the Dynamics of the Photospheric Magnetic Field. *ApJ*, 628(1):501–513, July 2005. doi: 10.1086/430733.
- Schühle, U., Halain, J.-P., Meining, S., & Teriaca, L. The Lyman-alpha telescope of the extreme ultraviolet imager on Solar Orbiter. In Fineschi, S. & Fennelly, J., editors, *Solar Physics and Space Weather Instrumentation IV*, volume 8148 of *Society of Photo-Optical Instrumentation Engineers (SPIE) Conference Series*, page 81480K, October 2011. doi: 10.1117/12.893573.
- Schwarzschild, M. On Noise Arising from the Solar Granulation. *ApJ*, 107:1, January 1948. doi: 10.1086/144983.
- Shibata, K., Ishido, Y., Acton, L. W., et al. Observations of X-Ray Jets with the YOHKOH Soft X-Ray Telescope. *PASJ*, 44:L173–L179, October 1992.
- Shimizu, T., Imada, S., Kawate, T., et al. The Solar-C (EUVST) mission: the latest status. In den Herder, J.-W. A., Nikzad, S., & Nakazawa, K., editors, *Space Telescopes and Instrumentation 2020: Ultraviolet to Gamma Ray*, volume 11444 of *Society of Photo-Optical Instrumentation Engineers (SPIE) Conference Series*, page 114440N, December 2020. doi: 10.1117/12.2560887.

BIBLIOGRAPHY

- Shimojo, M., Narukage, N., Kano, R., et al. Fine Structures of Solar X-Ray Jets Observed with the X-Ray Telescope aboard Hinode. *PASJ*, 59:S745, November 2007. doi: 10.1093/pasj/59.sp3.S745.
- Shimooda, H. Solar and Interplanetary Magnetic Field, II. Polar Rays and the General Magnetic Field. *PASJ*, 10:107, January 1958.
- Simon, G. W. & Leighton, R. B. Velocity Fields in the Solar Atmosphere. III. Large-Scale Motions, the Chromospheric Network, and Magnetic Fields. *ApJ*, 140:1120, October 1964. doi: 10.1086/148010.
- Solanki, S. K. & Steiner, O. How magnetic is the solar chromosphere? *A&A*, 234(1-2):519–529, August 1990.
- Solanki, S. K., del Toro Iniesta, J. C., Woch, J., et al. The Polarimetric and Helioseismic Imager on Solar Orbiter. *A&A*, 642:A11, October 2020. doi: 10.1051/0004-6361/201935325.
- Solanki, S. K. Sunspots: An overview. *A&A Rev.*, 11(2-3):153–286, January 2003. doi: 10.1007/s00159-003-0018-4.
- SPICE Consortium, Anderson, M., Appourchaux, T., et al. The Solar Orbiter SPICE instrument. An extreme UV imaging spectrometer. *A&A*, 642:A14, October 2020. doi: 10.1051/0004-6361/201935574.
- Stein, R. F. & Nordlund, Å. Simulations of Solar Granulation. I. General Properties. *ApJ*, 499(2):914–933, May 1998. doi: 10.1086/305678.
- Stix, M. *The sun: an introduction*. 2002.
- Stone, E. C., Frandsen, A. M., Mewaldt, R. A., et al. The Advanced Composition Explorer. *Space Sci. Rev.*, 86:1–22, July 1998. doi: 10.1023/A:1005082526237.
- Strong, K. T., Harvey, K., Hirayama, T., et al. Observations of the Variability of Coronal Bright Points by the Soft X-Ray Telescope on YOHKOH. *PASJ*, 44:L161–L166, October 1992.
- Sturrock, P. A. Model of the High-Energy Phase of Solar Flares. *Nature*, 211 (5050):695–697, August 1966. doi: 10.1038/211695a0.
- Sweet, P. A. The Neutral Point Theory of Solar Flares. In Lehnert, B., editor, *Electromagnetic Phenomena in Cosmical Physics*, volume 6 of *IAU Symposium*, page 123, January 1958.
- Tarbell, T. D. & Title, A. M. Measurements of magnetic fluxes and field strengths in the photospheric network. *Sol. Phys.*, 52(1):13–25, April 1977. doi: 10.1007/BF00935784.

- Teriaca, L., Banerjee, D., Falchi, A., Doyle, J. G., & Madjarska, M. S. Transition region small-scale dynamics as seen by SUMER on SOHO. *A&A*, 427:1065–1074, December 2004. doi: 10.1051/0004-6361:20040503.
- Teriaca, L., Poletto, G., Romoli, M., & Biesecker, D. A. The Nascent Solar Wind: Origin and Acceleration. *ApJ*, 588(1):566–577, May 2003. doi: 10.1086/368409.
- Tian, H., DeLuca, E. E., Cranmer, S. R., et al. Prevalence of small-scale jets from the networks of the solar transition region and chromosphere. *Science*, 346(6207):1255711, October 2014. doi: 10.1126/science.1255711.
- Tian, H., Curdt, W., Marsch, E., & He, J. Cool and Hot Components of a Coronal Bright Point. *ApJ*, 681(2):L121, July 2008. doi: 10.1086/590410.
- Tian, H., McIntosh, S. W., Habbal, S. R., & He, J. Observation of High-speed Outflow on Plume-like Structures of the Quiet Sun and Coronal Holes with Solar Dynamics Observatory/Atmospheric Imaging Assembly. *ApJ*, 736(2): 130, August 2011. doi: 10.1088/0004-637X/736/2/130.
- Title, A. M., Tarbell, T. D., Topka, K. P., et al. Statistical Properties of Solar Granulation Derived from the SOUP Instrument on Spacelab 2. *ApJ*, 336: 475, January 1989. doi: 10.1086/167026.
- Title, A. M., Frank, Z. A., Shine, R. A., et al. High Resolution Observations of the Magnetic and Velocity Field of Simple Sunspots. In Thomas, J. H. & Weiss, N. O., editors, *Sunspots. Theory and Observations*, volume 375 of *NATO Advanced Study Institute (ASI) Series C*, page 195, January 1992. doi: 10.1007/978-94-011-2769-1_9.
- Tomczyk, S., McIntosh, S. W., Keil, S. L., et al. Alfvén Waves in the Solar Corona. *Science*, 317(5842):1192–1196, August 2007. doi: 10.1126/science.1143304.
- Tomczyk, S., Card, G. L., Darnell, T., et al. An Instrument to Measure Coronal Emission Line Polarization. *Sol. Phys.*, 247(2):411–428, February 2008. doi: 10.1007/s11207-007-9103-6.
- Tomczyk, S. & McIntosh, S. W. Time-Distance Seismology of the Solar Corona with CoMP. *ApJ*, 697(2):1384–1391, June 2009. doi: 10.1088/0004-637X/697/2/1384.
- Trujillo Bueno, J., Shchukina, N., & Asensio Ramos, A. A substantial amount of hidden magnetic energy in the quiet Sun. *Nature*, 430(6997):326–329, July 2004. doi: 10.1038/nature02669.

BIBLIOGRAPHY

- Tsuneta, S., Acton, L., Bruner, M., et al. The Soft X-ray Telescope for the SOLAR-A mission. *Sol. Phys.*, 136(1):37–67, November 1991. doi: 10.1007/BF00151694.
- Tu, C.-Y., Zhou, C., Marsch, E., et al. Solar Wind Origin in Coronal Funnel. *Science*, 308(5721):519–523, April 2005. doi: 10.1126/science.1109447. URL <https://www.science.org/doi/10.1126/science.1109447>. Publisher: American Association for the Advancement of Science.
- Ulrich, R. K. The Five-Minute Oscillations on the Solar Surface. *ApJ*, 162:993, December 1970. doi: 10.1086/150731.
- Uritsky, V. M., DeForest, C. E., Karpen, J. T., et al. Plumelets: Dynamic Filamentary Structures in Solar Coronal Plumes. *ApJ*, 907(1):1, January 2021. doi: 10.3847/1538-4357/abd186.
- Vaiana, G. S., Davis, J. M., Giacconi, R., et al. X-Ray Observations of Characteristic Structures and Time Variations from the Solar Corona: Preliminary Results from SKYLAB. *ApJ*, 185:L47, October 1973a. doi: 10.1086/181318.
- Vaiana, G. S., Krieger, A. S., & Timothy, A. F. Identification and Analysis of Structures in the Corona from X-Ray Photography. *Sol. Phys.*, 32(1):81–116, September 1973b. doi: 10.1007/BF00152731.
- Verwichte, E., Marsh, M., Foullon, C., et al. Periodic Spectral Line Asymmetries in Solar Coronal Structures from Slow Magnetoacoustic Waves. *ApJ*, 724(2): L194–L198, December 2010. doi: 10.1088/2041-8205/724/2/L194.
- Waldmeier, M. *Ergebnisse und Probleme der Sonnenforschung*. 1955.
- Walker, Jr., A. B. C., DeForest, C. E., Hoover, R. B., & Barbee, Jr., T. W. Thermal and Density Structure of Polar Plumes. *Sol. Phys.*, 148(2):239–252, December 1993. doi: 10.1007/BF00645089.
- Wang, Y. M. Network Activity and the Evaporative Formation of Polar Plumes. *ApJ*, 501(1):L145–L150, July 1998. doi: 10.1086/311445.
- Wang, Y. M. Small Coronal Holes Near Active Regions as Sources of Slow Solar Wind. *ApJ*, 841(2):94, June 2017. doi: 10.3847/1538-4357/aa706e.
- Wang, Y. M. & Muglach, K. Observations of Low-Latitude Coronal Plumes. *Sol. Phys.*, 249(1):17–35, May 2008. doi: 10.1007/s11207-008-9171-2.
- Wang, Y. M. & Sheeley, Jr., N. R. On Potential Field Models of the Solar Corona. *ApJ*, 392:310, June 1992. doi: 10.1086/171430.

- Wang, Y. M. & Sheeley, Jr., N. R. Coronal Plumes and Their Relationship to Network Activity. *ApJ*, 452:457, October 1995a. doi: 10.1086/176317.
- Wang, Y. M. & Sheeley, Jr., N. R. Identification of Low-Latitude Coronal Plumes in Extreme-Ultraviolet Spectroheliograms. *ApJ*, 446:L51, June 1995b. doi: 10.1086/187928.
- Wang, Y. M. & Sheeley, Jr., N. R. Sources of the Solar Wind at Ulysses during 1990-2006. *ApJ*, 653(1):708–718, December 2006. doi: 10.1086/508929.
- Wang, Y. M., Sheeley, Jr., N. R., Socker, D. G., et al. Observations of Correlated White-Light and Extreme-Ultraviolet Jets from Polar Coronal Holes. *ApJ*, 508(2):899–907, December 1998a. doi: 10.1086/306450.
- Wang, Y. M., Sheeley, Jr., N. R., Walters, J. H., et al. Origin of Streamer Material in the Outer Corona. *ApJ*, 498(2):L165–L168, May 1998b. doi: 10.1086/311321.
- Warren, H. P. & Brooks, D. H. The Temperature and Density Structure of the Solar Corona. I. Observations of the Quiet Sun with the EUV Imaging Spectrometer on Hinode. *ApJ*, 700(1):762–773, July 2009. doi: 10.1088/0004-637X/700/1/762.
- Webb, D. F. & Howard, T. A. Coronal Mass Ejections: Observations. *Living Reviews in Solar Physics*, 9(1):3, December 2012. doi: 10.12942/lrsp-2012-3.
- Wedemeyer-Böhm, S. & Wöger, F. Small-scale structure and dynamics of the lower solar atmosphere. In Erdélyi, R. & Mendoza-Briceno, C. A., editors, *Waves & Oscillations in the Solar Atmosphere: Heating and Magneto-Seismology*, volume 247 of *IAU Symposium*, pages 66–73, May 2008. doi: 10.1017/S1743921308014671.
- Wiegelmann, T. & Sakurai, T. Solar force-free magnetic fields. *Living Reviews in Solar Physics*, 18(1):1, December 2021. doi: 10.1007/s41116-020-00027-4.
- Wiegelmann, T., Thalmann, J. K., & Solanki, S. K. The magnetic field in the solar atmosphere. *A&A Rev.*, 22:78, November 2014. doi: 10.1007/s00159-014-0078-7.
- Wilhelm, K. Solar coronal-hole plasma densities and temperatures. *A&A*, 455(2):697–708, August 2006. doi: 10.1051/0004-6361:20054693.
- Wilhelm, K. & Bodmer, R. Solar EUV and UV Emission Line Observations Above a Polar Coronal Hole. *Space Sci. Rev.*, 85:371–378, May 1998. doi: 10.1023/A:1005187509676.

BIBLIOGRAPHY

- Wilhelm, K., Curdt, W., Marsch, E., et al. SUMER - Solar Ultraviolet Measurements of Emitted Radiation. *Sol. Phys.*, 162(1-2):189–231, December 1995. doi: 10.1007/BF00733430.
- Wilhelm, K., Dammasch, I. E., Marsch, E., & Hassler, D. M. On the source regions of the fast solar wind in polar coronal holes. *A&A*, 353:749–756, January 2000.
- Wilhelm, K., Abbo, L., Auchère, F., et al. Morphology, dynamics and plasma parameters of plumes and inter-plume regions in solar coronal holes. *A&A Rev.*, 19(1):35, June 2011. doi: 10.1007/s00159-011-0035-7.
- Wilhelm, K., Marsch, E., Dwivedi, B. N., et al. The Solar Corona Above Polar Coronal Holes as Seen by SUMER on SOHO. *ApJ*, 500(2):1023–1038, June 1998. doi: 10.1086/305756.
- Wilken, V., de Boer, C. R., Denker, C., & Kneer, F. Speckle measurements of the centre-to-limb variation of the solar granulation. *A&A*, 325:819–824, September 1997.
- Withbroe, G. L. & Noyes, R. W. Mass and energy flow in the solar chromosphere and corona. *ARA&A*, 15:363–387, January 1977. doi: 10.1146/annurev.aa.15.090177.002051.
- Woo, R. & Habbal, S. R. Extension of coronal structure into interplanetary space. *Geophys. Res. Lett.*, 24(10):1159–1162, May 1997. doi: 10.1029/97GL01156.
- Yokoyama, T. & Shibata, K. Magnetic reconnection as the origin of X-ray jets and H α surges on the Sun. *Nature*, 375(6526):42–44, May 1995. doi: 10.1038/375042a0.
- Yokoyama, T. & Shibata, K. Numerical Simulation of Solar Coronal X-Ray Jets Based on the Magnetic Reconnection Model. *PASJ*, 48:353–376, April 1996. doi: 10.1093/pasj/48.2.353.
- Young, P. R. The element abundance FIP effect in the quiet Sun. *A&A*, 439(1):361–366, August 2005a. doi: 10.1051/0004-6361:20052963.
- Young, P. R. The Ne/O abundance ratio in the quiet Sun. *A&A*, 444(2): L45–L48, December 2005b. doi: 10.1051/0004-6361:200500206.
- Young, P. R. Element Abundance Ratios in the Quiet Sun Transition Region. *ApJ*, 855(1):15, March 2018. doi: 10.3847/1538-4357/aaab48.

-
- Young, P. R., Klimchuk, J. A., & Mason, H. E. Temperature and density in a polar plume - measurements from CDS/SOHO. *A&A*, 350:286–301, October 1999.
- Zhang, J., Kundu, M. R., & White, S. M. Spatial Distribution and Temporal Evolution of Coronal Bright Points. *Sol. Phys.*, 198(2):347–365, February 2001. doi: 10.1023/A:1005222616375.
- Zirin, H. *The Photosphere*, pages 175–190. Springer Netherlands, Dordrecht, 1992. ISBN 978-94-011-2765-3. doi: 10.1007/978-94-011-2765-3_8. URL https://doi.org/10.1007/978-94-011-2765-3_8.
- Zirker, J. B. Coronal holes and high-speed wind streams. *Reviews of Geophysics and Space Physics*, 15:257–269, August 1977. doi: 10.1029/RG015i003p00257.
- Zwaan, C., Brants, J. J., & Cram, L. E. High Resolution Spectroscopy of Active Regions - Part One - Observing Procedures. *Sol. Phys.*, 95(1):3–14, January 1985. doi: 10.1007/BF00162632.
- Zwaan, C. Elements and patterns in the solar magnetic field. *ARA&A*, 25: 83–111, January 1987. doi: 10.1146/annurev.aa.25.090187.000503.



Acknowledgement

This thesis work is carried out in the framework of the International Max Planck Research School for Solar System Science at the University of Göttingen and at TU Braunschweig and is funded by the Federal Ministry for Economic Affairs and Climate Action (BMWK) through the German Space Agency at DLR based on a decision of the German Bundestag (Funding code: 50OU2101).

I would like to express my gratitude to all the incredible human beings, who have made this thesis possible and my PhD journey memorable.

My deepest thanks go to my TAC members, Sami, Luca and Ferdinand, who have been always supportive during these years and during the thesis writing. Their invaluable feedback have transformed this thesis from some unpolished mess into what it is now.

I would like to sincerely thank my daily supervisor Luca, who, despite an impossibly busy schedule, has always been approachable and has never once kicked me out of his office. His insights in science, and in life, have been encouraging me to learn, to strive, and to enjoy the process. I also want to thank the people that I have been working with, Regina, Pradeep, Sami, Hardi, Thomas, and many more, for the insightful discussions and guidance in my work.

To all my friends here, thank you for being so amazing. The random chats, coffee breaks, endless cat pictures, and shared moments have brightened my days. This PhD journey would not have been the same without you. I am also grateful to my partner for all the support and company along the way.

I always owe thanks to my parents, who have no idea what I actually do, but stand behind me unconditionally, worrying about me and being proud of me. To my families and friends back home, thank you for simply being there and always caring. All the courage has brought me this far, and may carry me even further comes from the the belief that no matter what happens, there will always be a place saved for me.

Finally, my appreciation goes to the unbelievable weather and lunchbox food. I now feel ready to survive anything.



Publications

Refereed Publications

- Chitta, L.P.; **Huang, Z.**; D'Amicis, R.; Calchetti, D.; Zhukov, A.N.; Kraaikamp, E.; Verbeeck, C.; Aznar Cuadrado, R.; Hirzberger, J.; Berghmans, D. et al.: Coronal hole picoflare jets are progenitors of both fast and Alfvénic slow solar wind. *Astronomy and Astrophysics* 694, p. A71 (2025)
- **Huang, Z.**; Teriaca, L.; Aznar Cuadrado, R.; Chitta, L.P.; Mandal, S.; Peter, H.; Schühle, U.; Solanki, SK; Auchère, F.; Berghmans, D. et al.: Imaging and spectroscopic observations of extreme-ultraviolet brightenings using EUI and SPICE on board Solar Orbiter. *Astronomy and Astrophysics* 673, p. A82 (2023)
- Antolin, P.; Dolliou, A.; Auchère, F.; Chitta, L.P.; Parenti, S.; Berghmans, D.; Aznar Cuadrado, R.; Barczynski, K.; Gissot, S.; Harra, L. et al.: EUV fine structure and variability associated with coronal rain revealed by Solar Orbiter/EUI HRIEUV and SPICE. *Astronomy and Astrophysics* 676, p. A112 (2023)
- Berghmans, D.; Antolin, P.; Auchère, F.; Aznar Cuadrado, R.; Barczynski, K.; Chitta, L.P.; Gissot, S.; Harra, L.; **Huang, Z.**; Janvier, M. et al.: First perihelion of EUI on the Solar Orbiter mission. *Astronomy and Astrophysics* 675, A110 (2023)

Conference Contributions

- **17th European Solar Physics Meeting ESPM-17**
9/2024; Torino, Italy
Poster: High-resolution observations of small-scale activity in coronal hole plumes
- **Hinode-16/IRIS-13 Meeting**
9/2023; Niigata, Japan
Poster: High-resolution observations of small-scale activity in coronal hole plumes
- **SOLARNET Conference**
5/2023; Postdam, Germany
Poster: Imaging and spectroscopic observations of EUV brightenings using EUI and SPICE aboard Solar Orbiter
- **8th Solar Orbiter Conference**
9/2022; Belfast, The UK
Oral talk: Imaging and spectroscopic observations of EUV brightenings using EUI and SPICE aboard Solar Orbiter
- **SPICE Consortium Meeting**
6/2022; Online
Oral talk: Imaging and spectroscopic observations of EUV brightenings using EUI and SPICE aboard Solar Orbiter
- **EUI Consortium Meeting**
5/2022; Brussels, Belgium
Oral talk: Imaging and spectroscopic observations of EUV brightenings using EUI and SPICE aboard Solar Orbiter

Curriculum Vitae

Name: Huang, Ziwen

Year of birth: 1996

Nationality: Chinese

Education

Ph.D. in Physics 2021-2025

Max Planck Institute for Solar System Research Göttingen, Germany

IMPRS for Solar System Science

Technical University Braunschweig

Thesis: Investigating small-scale dynamics: Analysis and Interpretation of Solar Orbiter observations

M.Sc. in Astrophysics 2018-2021

Nanjing University Nanjing, China

School of Astronomy and Space Science

Thesis: A Kinematic and Thermodynamic Study of Confined Solar Eruptions

B.Sc. in Space Science 2014-2018

Nanjing University Nanjing, China

School of Astronomy and Space Science

Tutoring

The Sun and Heliosphere 2024

Technical University Braunschweig Braunschweig, Germany